

A TAILORED APPROACH TO ENGINEERING SOLID STATE SINGLE PHOTON
SOURCES

by

RACHAEL KLAISS

A DISSERTATION

Presented to the Department of Physics
and the Division of Graduate Studies of the University of Oregon
in partial fulfillment of the requirements
for the degree of
Doctor of Philosophy

June 2023

DISSERTATION APPROVAL PAGE

Student: Rachael Klaiss

Title: A Tailored Approach to Engineering Solid State Single Photon Sources

This dissertation has been accepted and approved in partial fulfillment of the requirements for the Doctor of Philosophy degree in the Department of Physics by:

Hailin Wang	Chairperson
Benjamín Alemán	Advisor
Benjamin McMorran	Core Member
Christopher Hendon	Institutional Representative

and

Krista Chronister	Vice Provost for Graduate Studies
-------------------	-----------------------------------

Original approval signatures are on file with the University of Oregon Division of Graduate Studies.

Degree awarded June 2023

© 2023 Rachael Klaiss

DISSERTATION ABSTRACT

Rachael Klaiss

Doctor of Philosophy

Department of Physics

June 2023

Title: A Tailored Approach to Engineering Solid State Single Photon Sources

Integrated quantum information technologies such as photonic circuits, quantum transducers, and magnetic sensors require robust single-photon sources in precise locations. Solid-state single photon emitters (SPEs) hosted by mid-bandgap defects in 2D material hexagonal boron nitride (hBN) are bright and stable at room temperature and demonstrate strong coupling to external fields, making them desirable candidates for quantum device applications. However, the specific atomic structure of hBN SPEs remains unidentified, making deterministic engineering a challenge. While recent studies have narrowed the range of possible defect candidates by demonstrating the role of carbon in hBN SPEs, the methods to engineer carbon-based defects in hBN either produce randomly located emitters or require bottom-up crystal growth on structured substrates.

We achieved patterned arrays of SPEs via focused ion beam (FIB) milling followed by chemical vapor deposition (CVD) of nanocrystalline graphite source for carbon diffusion, and found that both techniques are necessary for significant and repeatable creation of SPEs. This technique creates localized emitters with ten times the yield of carbon annealing alone. Furthermore, by adjusting the parameters of FIB exposure time and carbon annealing time, we found multiple different parameter combinations that successfully created SPEs, demonstrating the adjustability of this technique based on device application requirements.

Additionally, we performed atomic force microscopy to characterize the surface morphology of hBN regions patterned by Ga⁺ FIB to create SPEs at a range of ion doses and found that material swelling is strongly correlated to successful SPE creation. Furthermore, we simulated vacancy and impurity profiles to elucidate how Ga⁺ FIB patterning induces lattice damage in the form of vacancies, structural voids, and amorphous layers, creating a diffusion barrier to control the introduction of carbon impurities to engineer isolated SPEs with high resolution of process control. Our results provide novel insight into the formation of hBN SPEs created by high-energy, heavy-ion FIB that can be leveraged for monolithic hBN photonic devices and a wide range of low-dimensional solid-state SPE hosts.

This dissertation includes previously published and unpublished coauthored material.

CURRICULUM VITAE

NAME OF AUTHOR: Rachael Klaiss

GRADUATE AND UNDERGRADUATE SCHOOLS ATTENDED:

University of Oregon, Eugene, OR
University of California Berkeley, Berkeley, CA

DEGREES AWARDED:

Doctor of Philosophy, Physics, 2023, University of Oregon
Bachelor of Arts, Physics, 2017, University of California Berkeley

AREAS OF SPECIAL INTEREST:

Color centers in wide bandgap semiconductors
Defect engineering
2D materials
Materials characterization

PROFESSIONAL EXPERIENCE:

Graduate Research Assistant, Alemán Lab, University of Oregon, Eugene,
Oregon, 2017-2023

Graduate Teaching Assistant, Department of Physics, University of Oregon,
Eugene, Oregon, 2017-2022

Graduate Teaching Assistant, Graduate Internship Program Photovoltaic and
Semiconductor Device Processing Track, Knight Campus for Accelerating Scientific
Impact, Eugene, Oregon 2020-2022

Diversity Equity and Inclusion Graduate Employee, Department of Physics, University of
Oregon, Eugene, Oregon, 2021

GRANTS, AWARDS, AND HONORS:

Future Leaders Society, Finalist for K. Patricia Cross Future Leaders Award, American
Association of Colleges & Universities, 2023

Weiser Leadership Award, Department of Physics, University of Oregon, 2022

Karfilis Leadership Award, University of Oregon Women in Graduate Sciences, 2021

Best Student Poster, “Hexagonal Boron Nitride Defect Investigation via Super Resolution Imaging of Quantum Emission”, Oregon Center for Optical, Molecular, and Quantum Science, 2019

Summer Research Institute Fellowship, CalTeach, University of California Berkeley, 2015

PUBLICATIONS:

R. Klaiss, J. Ziegler, D. Miller, K. Zappitelli, K. Watanabe, T. Taniguchi, and B.J. Alemán. Uncovering the morphological effects of high energy Ga⁺ focused ion beam milling on hBN single-photon emitter fabrication. *J. Chem. Phys.* **157**, 074703 (2022).

J. Ziegler, R. Klaiss, A. Blaikie, D. Miller, V.R. Horowitz, and B.J. Alemán. Deterministic quantum emitter formation in hexagonal boron nitride via controlled edge creation. *Nano Lett.* **19**, 2121-2127 (2019).

ACKNOWLEDGMENTS

--
*I am a blank canvas
and the Mona Lisa
if we were all born with a paintbrush in hand*
--

I owe the deepest gratitude to my advisor, Benjamín Alemán, for a phone call back in the Fall of 2016 that kickstarted this whole thing, and for all of the moments along the way when you were my biggest cheerleader and advocate. Thank you for making this work possible, for trusting me as I took this project down the path that spoke to me, and for validating my skills as a scientist, educator, and communicator. I move on to the next stage of my career with full confidence in my abilities because of your mentorship.

To my lab mates and collaborators who taught me that science is a group effort both inside and outside the lab: Brittany Carter, for chem room cleaning sessions, office chats, and soup nights; Uriel Hernandez, for shared experiences and putting on so many hats; Rudy Resch, David Miller, Andrew Blaike, Kara Zappitelli, and Josh Ziegler, for laying foundations and teaching me how to conquer mountains and graduate school; Davis Austin, Skippy Clairmont, Paulina Nelson, Josh D’Mello, Halle Foster, Silkie Melloul, and Alena McVicker, for learning along with me; Sai Krishna Narayanan and Pratibha Dev, for calculations and reaching out; Viva Horowitz, for showing me what’s possible; Hailin Wang, Ben McMorran, and Chris Hendon, for serving on my committee and providing valuable insight beyond what the role requires.

To the educators and scientists who shaped my passions for physics, unfurling its wonders for others, and ending the active exclusion of and harm done to many in the field: Mrs. Revelle, for “Best Girl Scientist”; Mr. Emmanuel and Professor Haefner, for seeing my interest and intuition for physics before I could see it myself; Frank Ferrone, for answering a cold email from a college

freshman and making my research career possible; Geoff Wehmeyer and the Dames Lab, for including me in part of a broader research community; Matt Gilbert and the Zettl Lab, for teaching me that I can always figure it out and try again; Robbie McGehee and Eli Mizrahi, for still being my models for a great mentorship group; Nima Dinyari, Fuding Lin, Stacey York, and Lynde Ritzow, for showing me that I can bring my whole self to work every day; Joel Corbo, Gina Quan, and the Access Network, for helping me find my niche and doing what you do; Tien-Tien Yu and Steven van Enk, for giving me agency, encouragement, and structure in the classroom; Stephanie Majewski, Laura Jeanty, and Tim Cohen, for listening; My mentees Francis Duey, Jasper Marcum, and Cristian Garcia, for sticking with me; The student leaders and organizers involved with UOWiP/PAGES, DuckREFS, North Star, and GTFF, for showing up and getting it done.

To my friends that span states and stages of my life, I'm so glad I found you all when I did: Erin Coffman, Megan Bottino, and Sofia McCline, for being there through all evolutions; Lauren Capelluto, for being my Berkeley first and longest; Mike Lu and Jack Twilling, for Math 1B, Napa wineries, and everything in between; Siena Ramirez and Andy Meislin, for helping us get it together; Lexi Goldwyn, Maddy Spiering, Megan Perley, Rayna Kim, and so many other Zeta sisters, for showing me the true meaning of #ZLAM and #4Years4Life; Nicole O'Shea, for keeping it classy and catty; Christine Abelyan, Melissa Hazelwood, Ramsey Karim, Joe Costello, Danny Tuthill, Rob Bentley, Mac Robertson, and Chris Agostino, for the reading room, study snacks, and support; The many iterations of Big Pink: Justin Kittell, Ethan Turner, Marija Glisic, Claire Pokorny, Andrew Lesak, and Cassidy Wagner, for always tuning in for Rachael's Opinion Time and turning our little old house into a little old home; Michael Hurst, for sharing the longest and hardest leg of this journey with me; Grace Waddell and Steph VanBeuge, for showing me that physicists, chemists, and biologists aren't so different after all; Daniel Moore

and Dylan Heim, for your campaign shenanigans and unique perspectives; Amy Soudachanh and Sean Brudney, for the chats; UO Phys Grads, especially the Fall 2017 cohort, for reading all my emails and showing me that grad school can be fun; Grace Lindquist, Kendra Lady, Chelsea Godon, and the many dancers I've had the privilege of working with over the last 18 months, for introducing me to your community and reminding me about balance.

To my whole extended family that I know I'm making proud, and in particular: Aunt GG, for remembering more than I ever expected; Aunt Carole, for being a safe and comfortable place; Shannon, for popping in with a cat video and smile every so often; Aunt Kathy, for making a place at the table for me.

To my parents, AnnaMarie and Harry: I have always believed I could do anything I set my mind to because of you, and I knew that you would support me every step of the way. This wouldn't have been possible without either of you. I know you are proud of me, and I'm proud of me—so please give yourselves a space to be proud of yourselves. This is your accomplishment too.

To my late baby brother, Harrison: I never doubted for a second that you'd want me to finish this thing, and honestly, I never even considered *not* finishing it. I couldn't suddenly change what you thought was going to happen, so I kept going. I wish we could've had those thesis writing parties like we talked about, but I'm grateful for all you taught me about writing. Thank you for taking notes every time I tried to teach you about my work, because you said you wanted to understand my defense when it came around. Thank you for your unending curiosity, admiration, and love. I will carry them with me the rest of my life, in everything I do.

If you are feeling alone and having thoughts of suicide—whether or not you are in crisis—or know someone who is, don't remain silent. Call or text the [988 Suicide & Crisis Lifeline](#) at **988**. The Lifeline provides free and confidential emotional support to people in suicidal crisis or emotional distress 24 hours a day, 7 days a week, across the United States.

For Harrison. Thanks for stopping by.

“Go confidently in the direction of your dreams. Live the life you have imagined”
-Henry David Thoreau

TABLE OF CONTENTS

Chapter	Page
I. INTRODUCTION	20
1.1. Solid State Single Photon Sources for Integrated Photonics	20
1.2. Two-Dimensional Wide-Bandgap Insulator Hexagonal Boron Nitride SPEs.....	21
1.3. Current Challenges in Engineering hBN SPEs	23
II. ENGINEERING CARBON-BASED QUANTUM EMITTERS IN HEXAGONAL BORON NITRIDE.....	25
2.1. Introduction.....	25
2.2. Results and discussion	26
2.3. Conclusions.....	35
2.4. Methods.....	35
2.5. Supplementary information	38
2.6. Bridge.....	56
III. UNCOVERING THE MORPHOLOGICAL EFFECTS OF HIGH ENERGY GA+ FOCUSED ION BEAM MILLING ON HBN SINGLE-PHOTON EMITTER FABRICATION.....	58
3.1. Introduction.....	58
3.2. Results and discussion	60

Chapter	Page
3.3. Conclusions.....	76
3.4. Methods.....	77
3.5. Supplementary information	88
3.6. Bridge.....	90
IV. MODELING EXTRINSIC IMPURITY DIFFUSION FOR COLOR CENTER FORMATION.....	91
4.1. Introduction.....	91
4.2. Results and discussion	92
4.3. Conclusions.....	100
4.4. Methods.....	101
4.5. Supplementary information	103
V. CONCLUDING REMARKS.....	114
APPENDICIES	116
A. CORRELATIVE SCANNING NEAR-FIELD OPTICAL FLUORESCENCE AND TOPOGRAPHY OF HBN COLOR CENTERS	116
B. SAMPLE IMAGES.....	121
C. HOME-BUILT CONFOCAL MICROSCOPE USE INSTRUCTIONS	125

Chapter

Page

REFERENCES CITED..... 130

LIST OF FIGURES

Figure	Page
Figure 2.1. SPE fabrication process flow diagram	27
Figure 2.2. Characterizing SPEs patterned in pristine hBN.....	28
Figure 2.3. Four factor two level screening SPE yield response	30
Figure 2.4. Parameters and interactions that influence SPE yield	31
Figure 2.5. Optimizing SPE yield via FIB exposure and carbon annealing interaction	33
Figure 2.6. Tailoring antibunching at $g^2(0)$ and emission energy.....	34
Figure 2.7. Process flow diagrams for control experiments	39
Figure 2.8. Raman characterization of diffusion source deposition	41
Figure 2.9. SEM and PL centroid analysis to localize patterned SPEs.....	41
Figure 2.10. Fabrication parameter factor screening details.....	42
Figure 2.11. Plots for single factor effects on SPE yield.....	47
Figure 2.12. Plots for two-factor interaction effects on SPE yield.....	48
Figure 2.13. Plots for three-factor interaction effects on SPE yield	49
Figure 2.14. FIB exposure and carbon annealing interaction optimization parameters	50
Figure 2.15. Second order photon correlation fit parameter distributions.....	55
Figure 2.16. Example zero phonon line spectra shapes for $g^2(0) > 0.5$	56
Figure 3.1. Testing FIB exposure on a single hBN flake.....	60
Figure 3.2. AFM characterization of FIB exposure levels.....	61
Figure 3.3. Morphological characteristics calculated from AFM height data	62
Figure 3.4. Average morphological characteristics for each FIB exposure level	63
Figure 3.5. Summary of photophysical characterization by FIB exposure.....	66

Figure	Page
Figure 3.6. Correlating material damage to SPE yield and photoluminescence.....	67
Figure 3.7. Simulated FIB exposure dose profile	68
Figure 3.8. SRIM vacancy concentration profile.....	69
Figure 3.9. Estimating damage thresholds from simulated vacancies	70
Figure 3.10. Simulated swelling and milling via vacancy concentration thresholds.....	72
Figure 3.11. Illustration of vacancy distribution, void nucleation and growth, and milling	73
Figure 3.12. Analyzing AFM height data to calculate morphological characteristics.....	80
Figure 3.13. Stopping Range of Ions in Matter vacancy concentration.....	83
Figure 3.14. Simulating FIB patterning beam path.....	84
Figure 3.15. AFM height scan data of pre-exposure hBN flake.	88
Figure 3.16. Mean calculated values for average heights and exposed edge surface area	89
Figure 3.17. Measured values for ZPL and $g^2(0)$	89
Figure 4.1. Extended atomic force microscopy and photoluminescence characterization.	93
Figure 4.2. Illustrations demonstrating multilayer diffusion model formulation	95
Figure 4.3. Evaluated model at tested anneal times.....	96
Figure 4.4. Model parameter dependence of SPE supersaturation characteristics	97
Figure 4.5. Full AFM characterization at 4 different anneal times.....	104
Figure 4.6. Multi-layer diffusion carbon concentration profiles.....	105
Figure 4.7. Illustration of Boltzmann distribution model for defect formation	106
Figure 4.8. Density functional theory (DFT) calculations	113
Figure A.1. Schematic of WITec SNOM adapted for fluorescence.....	118

Figure	Page
Figure A.2. Improving confocal resolution with SNOM.....	118
Figure A.3. Simultaneous correlation of hBN color center SNOM to AFM.....	119
Figure A.4. Correlative imaging of an hBN quantum emitter.....	120
Figure B.1. Optical and SEM of factor screening samples.....	121
Figure B.2. Confocal PL scans of factor screening samples.....	122
Figure B.3. Optical and SEM of optimization samples.....	123
Figure B.4. Confocal PL of optimization samples.....	124

LIST OF TABLES

Table	Page
Table 2.1. Control Experiments Results	39
Table 2.2. Control Experiments – SPE Yield Mean Comparison Tests	40
Table 2.3. Factor Screening Experiments Results	45
Table 2.4. Thin, 500 nm, 3.8 ms, 5 hr – Mean SPE Yield Comparison Tests	45
Table 2.5. Factor Screening Full Model Effects Test for Number of SPEs.....	46
Table 2.6. Ion Fluences for Optimization FIB Exposure Levels	50
Table 2.7. Optimization Experiments Results	51
Table 2.8. Optimization Experiments – Mean SPE Yield Comparison Tests	52
Table 2.9. Optimization Experiments – Mean Region PL Comparison Tests.....	53
Table 2.10. Top 5 Optimization Experiments – Mean $g^2(0)$ Comparison Tests.....	54
Table 2.11. ZPL by FIB Exposure – Mean Comparison Tests.....	55
Table 2.12. ZPL by Carbon anneal time – Mean Comparison Tests	55
Table 3.1. Morphological Characteristics Calculated from AFM	63
Table 4.1. Average Mill Depth by FIB Exposure time– Mean Comparison Tests.....	103
Table 4.2. Average Swell Height by FIB Exposure time– Mean Comparison Tests	103
Table 4.3. Model Parameters Used for Figure 4.3	105
Table 4.4. Model Parameter 2^4 Results –Time of Max SPE Probability	109
Table 4.5. Model Parameter 2^4 Results –SPE Onset Time.....	109
Table 4.6. Model Parameter 2^4 Results –Color Center Saturation Time	110
Table 4.7. Factor Screening Full Model Effects Test for Time of Max SPE Probability.....	110

Table	Page
Table 4.8. Factor Screening Full Model Effects Test for SPE Onset Time.....	111
Table 4.9. Factor Screening Full Model Effects Test for Color Center Saturation Time.....	111

CHAPTER I

INTRODUCTION

1.1. Solid State Single Photon Sources for Integrated Photonics

Advances in quantum technology that promise more complex computation, secure communication, and accessible sensing rely on scaling the unique capabilities of quantum emitters (QEs)—atom-like systems such as quantum dots and solid-state defects—to practical devices, while connecting sources that operate at multiple wavelength ranges in a quantum network.¹ Promising qubit candidates for communicating between quantum technologies over long distances are single photon emitter (SPE) polarization qubits with tunable wavelength and stable fluorescence², while spin qubits with SPE readout via optically detectable magnetic resonance (ODMR) are desirable for quantum sensing and transduction applications. Currently, classical light mediates communication between various systems, for example in the transmission of information in fiber optic cables for television or internet. SPEs can be coupled to optical fibers for transmission, demonstrating an avenue for sending information in a quantum network.³

However, a requirement for telecommunication is microwave photon conversion, which is yet to be demonstrated in a tunable and stable quantum light system.⁴ For example, silicon-based QEs (e.g. *G*, *W*, and *T*-centers) are desirable for photonics applications due to the mature understanding of silicon-based electronics fabrication and emission in the telecom band, but these systems require cryogenic temperatures for operation and photon conversion platforms require increasingly complex fabrication, making practical applications elusive.⁵⁻⁷

A way to convert QEs outside the telecom band to telecommunication frequencies is through coupling to mechanical modes, which operate at high frequencies. Solid-state QEs that operate at room temperature in the visible band are an attractive way to couple optical readout signals to spin, electronic, or phononic degrees of freedom when applied to hybrid and heterogenous integrated photonics, allowing for communication and translation between different components in a range of applications.^{8,9} These quantum applications require stable, indistinguishable SPEs and scalable placement, the limitations of which depend highly on the solid-state source and fabrication technique.

Optomechanical devices have demonstrated coupling between mechanical modes and light in quantum dots and NV centers in diamond via strain mediation and electron spin centers in diamond via surface acoustic waves.¹⁰⁻¹² Two-dimensional (2D) materials such as graphene, hexagonal boron nitride (hBN), and transition metal dichalcogenides (TMDCs) (e.g. MoS₂, WSe₂, etc.) have a wide parameter space in the mechanical regime due to their low mass and high capacity for strain, with mechanical resonances in the telecommunication frequency regime.¹³ SPEs from 2D material hosts therefore promise strong single photon optomechanical coupling, with an ideal source operating at room temperature to decrease the reliance on cryogenics.⁴

1.2. Two-Dimensional Wide-Bandgap Insulator Hexagonal Boron Nitride SPEs

hBN SPEs are a desirable platform for integrated photonics and quantum technologies applications due to the utility of hBN in many existing technologies as an insulating layer, as well as unique SPE properties when compared to both bulk and other 2D hosts. hBN is a wide bandgap semiconductor and emitters are hosted in mid-bandgap states caused by atomic vacancy defects.¹⁴ States that are within the band gap can be excited without also mediating exciton

recombination optical emission. Therefore, hBN single photon sources do not require cooling to cryogenic temperatures to exhibit bright, stable, and narrow spectral lines of single photon emission in contrast to SPEs from TMDCs.^{15,16}

The characteristic spectral line shape of a SPE is called the zero-phonon line (ZPL) due to emission not requiring phonon assistance to reach the energy between excited and ground states. The ZPL of different hBN SPEs can range over hundreds of nanometers.^{17,18} The range in ZPL has been attributed to various vacancy-antisite and vacancy-interstitial defect complexes such as $N_B V_N$ and $C_N V_B$ as well as to a range of vacancy defect complexes with anywhere from one to sixteen vacancies per defect.^{19,20} Substrate interactions are also expected to induce ZPL variation even for the same defect due to local strain and charge gradients.²¹

hBN SPEs can be heavily influenced by the host environment. Blinking emitters have been observed and characterized in numerous systems.²²⁻²⁴ Consistent with other quantum systems such as quantum dots and single molecules, the dynamics of blinking follow a power law fit, which attributes the blinking to a population trap or accessing a triplet dark state by spontaneous fluctuations.²⁵⁻²⁷ Spectral diffusion has also been attributed to random changes to the charge surrounding the single photon source, inducing a strong local Stark shift.²⁸ These random fluctuations are hypothesized as due to charge diffusing from the sample substrate or the environment.¹⁷⁻²³

Similar to the NV-center in diamond, V_B^- in hBN exhibits optically detectable magnetic resonance (ODMR) that has been demonstrated as a spin sensor for ferromagnetic materials.^{29,30} Additionally, hBN defects not specifically identified as V_B^- are sensitive to strain³¹ and external electric fields, exhibiting strong stark shifts³², while carbon-based defects of various complex types and sizes are expected to be spin sensitive^{33,34}. Furthermore, recent work has shown that

twisted bilayers of hBN can host emitters, which are also magnetically sensitive and tunable when exposed to electron beams^{35,36}.

1.3. Current Challenges in Engineering hBN SPEs

To be useful for applications, e.g. into arrays for photonic circuits, or into structures like nanoelectromechanical systems or optical cavities, it is essential that the SPEs be patterned at well-defined positions^{8,9}. There is some success in large-scale activation of hBN SPEs with bulk focused ion beam (FIB)^{37,38} and plasma irradiation³⁹, but these methods generate randomly positioned emitters in a large area and tend to produce ensembles that cannot be isolated into single photons. Moreover, carbon implantation (and deposition) of hBN revealed the likely role of carbon in emitting defects—carbon-vacancy centers—but was also only successful at producing randomly located emitters⁴⁰. Similar results have been attained by bottom-up growth⁴⁰ or annealing of hBN crystals in the presence of atomic carbon⁴¹.

Patterning of SPEs in hBN has been realized via low electron beam (e-beam) irradiation⁴² and nanoindentation with an atomic force microscopy (AFM) tip⁴³, and was achieved by the authors in earlier work²³ by milling nanoscale holes and edges into hBN followed by annealing, but the replication success and efficiency highly depended on material properties and even local variations of a given sample; for example, SPE nanofabrication was not possible in high-quality exfoliated hBN. Ultimately, challenges in engineering and localizing hBN SPEs persist because the specific atomic structure of defects varies greatly and the physical mechanism for defect formation enabled by patterning and doping has not been thoroughly investigated.

In order to address these challenges, we developed an adjustable technique using FIB patterning to create edges and vacancies that allow for diffusive impurity doping to create visible-range, room temperature SPEs in hBN, likely in the form of carbon-vacancy defect

complexes. By characterizing both photophysical properties of the SPEs and morphological features of the patterned hBN regions for multiple FIB and impurity diffusion parameter combinations, we propose a model for the physical mechanism of defect formation with this technique. Understanding the physical mechanism of defect formation provides a framework to optimize fabrication of not just hBN SPEs, but other impurity defect-based solid state SPEs that can be used in a wider range of photonics applications. Furthermore, this adjustable engineering technique can be leveraged to minimize negative effects of substrate interactions and local charge fluctuations on spectral diffusion and photon indistinguishability, thereby improving the viability of solid-state SPEs for scalable integrated photonics.

The work described in this dissertation is based largely on co-authored material. Chapters II and IV contain unpublished co-authored material with contributions from Josh Ziegler, David Miller, Kara Zappitelli, Kenji Watanabe, Takashi Tanaguchi, Sai Krishna Narayanan, Pratibha Dev, and Benjamín Alemán. Chapter III contains published co-authored material with contributions from Josh Ziegler, David Miller, Kara Zappitelli, Kenji Watanabe, Takashi Tanaguchi, and Benjamín Alemán.

CHAPTER II

ENGINEERING CARBON-BASED QUANTUM EMITTERS IN HEXAGONAL BORON NITRIDE

This chapter contains in-preparation co-authored material; it has been reproduced with permission from: R. Klaiss, J. Ziegler, D. Miller, K. Zappitelli, K. Watanabe, T. Tanaguchi, S.K. Narayanan, P. Dev, B. J. Alemán, “An adjustable focused ion beam – impurity diffusion approach to pattern hexagonal boron nitride quantum emitters.” In this work, I contributed to designing the research, performing the research, analyzing the data, and writing the paper.

2.1. Introduction

Solid-state single photon sources are essential platforms for all-optical quantum computing, quantum communication, and as sources for quantum optics experiments, and are desirable due to ease of on-chip integration and coupling to the material host as a means of control and tunability^{1,8,9,44,45}. Single photon emitters (SPEs) have been discovered in various 2D materials, which offer particularly straightforward integration, strong surface-sensitivity, and a wider range of strain-tunability than their bulk counterparts^{3,44,46}. Hexagonal boron nitride (hBN) SPEs are particularly effective due to 2D material host and defect states hosted within the wide bandgap, leading to robustness at room temperature^{47,48}.

Practical application of SPEs for photonics applications requires straightforward, deterministic placement of defects, but many techniques currently require structured substrates⁴⁹ or niche ion implantation systems⁵⁰. In our previous work utilizing focused ion beam (FIB)

patterning to address this challenge, milling into poorer quality chemical vapor deposition (CVD) grown hBN worked the best²³. This CVD grown hBN likely had high levels of amorphous carbon from the multi-step polymer transfer process, further indicating that the presence of carbon was essential to creating the emitters. Guided by these observations, we conjecture that nanofabrication was enabled by diffusive driving of carbon into vacancies located near edges of holes.

To test this idea, we combine FIB nanopatterning with CVD of nanocrystalline-graphite (NC-Gr) as a carbon diffusion source to nanofabricate quantum emitters in hBN. We find SPEs in positions localized to our FIB patterning process and use factor screening to determine which process parameters are important for SPE creation. We postulate that this process works when elemental carbon diffuses into vacancies created by FIB, entering at the edges from the surface of the hBN and perform process optimization experiments to test this model.

2.2. Results and discussion

The steps to fabricate samples used in this work are outlined in **Figure 2.1**, with more details in **2.4 Methods**. To create edge defects at deterministic locations, we patterned arrays of 500 nm circles separated by a 1 μm pitch with beam parameters determined in our previous work as optimal for SPE creation.^{23,51} We then performed CVD of NC-Gr via non-catalytic ethylene decomposition (confirmed via Raman spectroscopy [**Supplementary information Figure 2.8**]) at 1000°C, the annealing temperature used by Lyu et al. to activate hBN SPEs in a carbon rich environment⁴¹. To remove residual surface NC-Gr prior to characterization, we annealed the samples under flowing oxygen.

We identified spots of photoluminescence (PL) and measured the degree of second-order coherence ($g^2(t)$) of emitted photons via Hanbury-Brown and Twiss experiment in a home-built

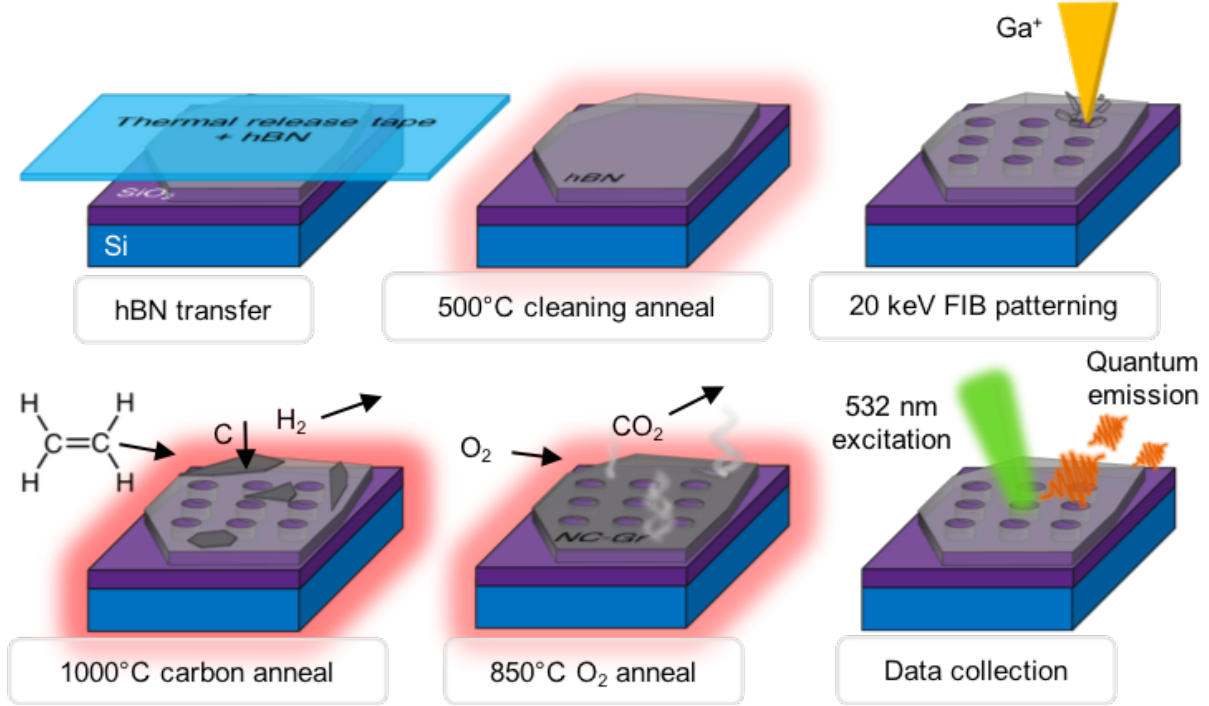


Figure 2.1. SPE fabrication process flow diagram starting with hBN transfer, followed by cleaning anneal, Ga⁺ FIB patterning, carbon annealing shown via ethylene decomposition, cleaning of carbon diffusion source shown via oxidation, and ending with characterization of single photon emission via 532 nm excitation in home-built confocal microscope

confocal microscope with 532 nm excitation [Figure 2.2(a), Supplementary information

Figure 2.9, 2.4 Methods]. These measurements were used to determine if PL sources exhibited antibunching, and also yielded their average photon number, nonradiative and radiative lifetimes, and bunching amplitude. These parameters were extracted from antibunching measurements by fitting our data to the following second order correlation function model for a three-level system:

$$g^2(t) = 1 - \rho^2 + \rho^2 \left(1 - (1 - a)e^{-|t|/\tau_1} + ae^{-|t|/\tau_2} \right) \quad (2.1)$$

where a is the bunching amplitude, τ_1 is the nonradiative lifetime, τ_2 is the radiative lifetime, and $\rho^2 = 1 - g^2(0)$ where $g^2(0)$ is the degree of antibunching. Photon number in a given milled hole was determined by binning $g^2(0)$ values according to:

$$g^2(0) = 1 - \frac{1}{n} \quad (2.2)$$

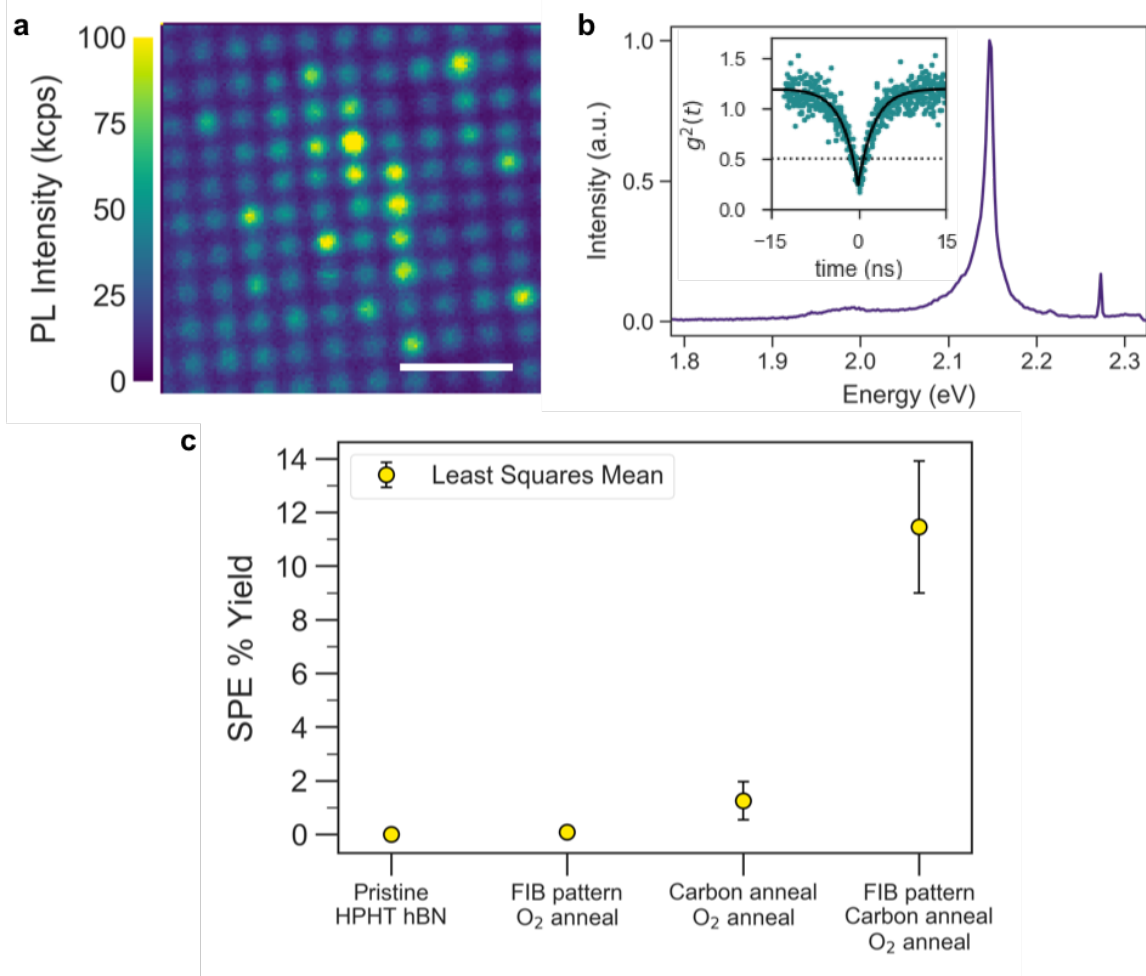


Figure 2.2. Characterizing SPEs patterned in pristine hBN (a) Representative confocal PL map of a color center array on an hBN flake patterned with the described process. Dashed lines indicate hBN flake edges. Scale bar: 4 μm (b) Zero-phonon line (ZPL) at ~ 2.15 eV and corresponding phonon sideband (PSB) emission of 160 meV for a representative single photon emitter created with this process. Inset: $g^2(t)$ for the emitter with $g^2(0) = 0.24$, well below the $g^2(0) < 0.5$ threshold for single photon emission. (c) Yield of patterned sites that hosted single photon emitters on samples subjected to 4 different treatment combinations. Error bars show standard error on mean.

We use the accepted antibunching threshold for SPE ($g^2(0) < 0.5$) to categorize emitting sites as SPE [Figure 2.2(b) Inset]. We denote any emitting sites that exhibit antibunching (with $0.5 < g^2(0) < 1$) as quantum emitters (QE). We categorize any bright emitting sites that do not exhibit antibunching ($g^2(0) = 1$) and do not photobleach as color centers. We further characterized the quantum emitting nature of the spots by acquiring spectra, where we observe

the expected zero-phonon line (ZPL) and corresponding phonon sideband (PSB) for quantum emitters [Figure 2.2(b)].

FIB patterning followed by carbon annealing produced SPEs with higher yield than only FIB patterning or only carbon annealing [Figure 2.2(c)]. The combined process (optimized parameters) yielded 0.1146 ± 0.0094 SPEs/patterned site (0.1146 ± 0.0094 SPEs/ μm^2), approximately 9.2 times more SPEs than carbon annealing alone (0.0125 ± 0.0071 SPEs/ μm^2) [Supplementary information Table 2.2 Student's t test: $p < 0.0001$]. This observed difference in yield is in qualitative agreement with our density functional theory (DFT)-based calculations of the defect formation energies for a representative set of carbon-based defect complexes, which consist of substitutional carbons adjacent to different vacancies. The formation energy of these defect complexes in pristine hBN are much larger than the energies required to incorporate carbon once defects have already been created in hBN [see Chapter IV Supplementary information Figure 4.8(a)]. The latter scenario emulates experimental process of FIB followed by CVD.

To determine which fabrication parameters of the combined FIB-CVD technique contributed to the improved SPE yield, we performed a two-level factor screening on four targeted factors: hBN thickness (14.59 ± 4.81 nm, 28.47 ± 5.42 nm), FIB pattern size (250 nm, 500 nm), FIB exposure time (2.5 ms, 3.8 ms), and carbon annealing time (20 min, 300 min) [Supplementary information Figure 2.10]. The parameter combination from this factor screening that produced the highest SPE yield was: 500 nm pattern diameter holes exposed for 3.8 ms on a 16 nm flake with 5 hours of carbon annealing time [Figure 2.3]. Samples fabricated with this combination of parameters yielded 0.0673 ± 0.0058 SPEs/patterned site, which was 3.4 times higher than the

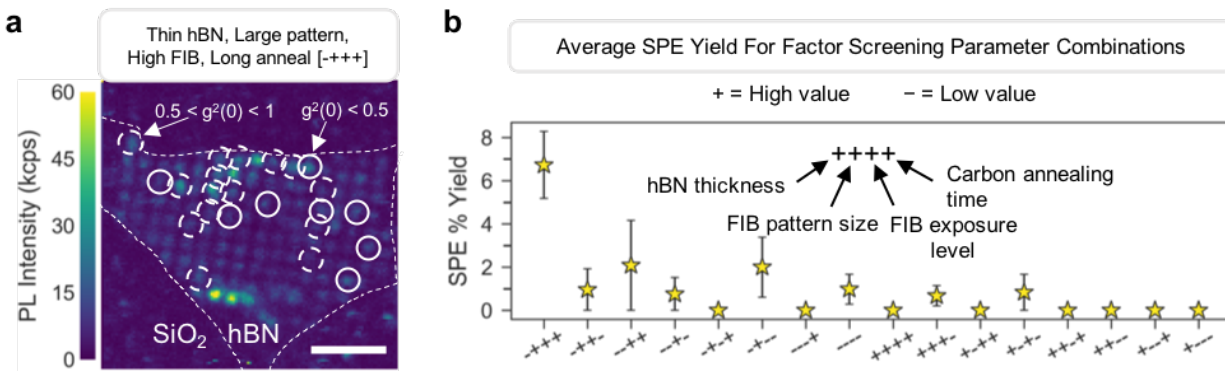


Figure 2.3. Four factor two level screening SPE yield response (a) Confocal PL scan for a sample processed under the best conditions for SPE creation during factor screening. SPEs are circled in solid white line, QEs are circled in dashed white line. Scale Bar: 4 μm (b) All factor combinations tested, showing that the low thickness, high FIB pattern size, high FIB exposure time, high carbon annealing time combination lead to the highest SPE yield (Tukey-Kramer HSD)

second-best parameter combination [**Supplementary information Table 2.4** Student's t test: $p = 0.0022$].

We found that hBN thickness had the strongest single-factor effect on SPE yield. Thinner flakes hosted 9.1 times higher SPE yields than thicker flakes, regardless of the chosen FIB exposure time, pattern size, and carbon annealing time [**Supplementary information Table 2.5** F-test: $p = 0.004$] [**Figure 2.4(a)**]. The FIB exposure time was the only other single factor that influenced the SPE yield, with “high” exposure producing 4 times higher SPE yields than “low” exposure [**Supplementary information Table 2.5** F-Test: $p = 0.028$] [**Figure 2.4(b)**].

Somewhat surprisingly, annealing samples for 5 hours did not, on average, produce a higher or lower SPE yield than annealing samples for 20 minutes [**Supplementary information Table 2.5** F-test: $p = 0.544$].

When we accounted for parameter interactions, we found that increasing the anneal time increased the SPE yield only in the high exposure case, whereas it decreased the SPE yield in the low exposure case, indicating a strong FIB exposure time and carbon anneal time interaction effect [**Supplementary information Table 2.5** F-test, $p = 0.042$] [**Figure 2.4(c)**]. Furthermore,

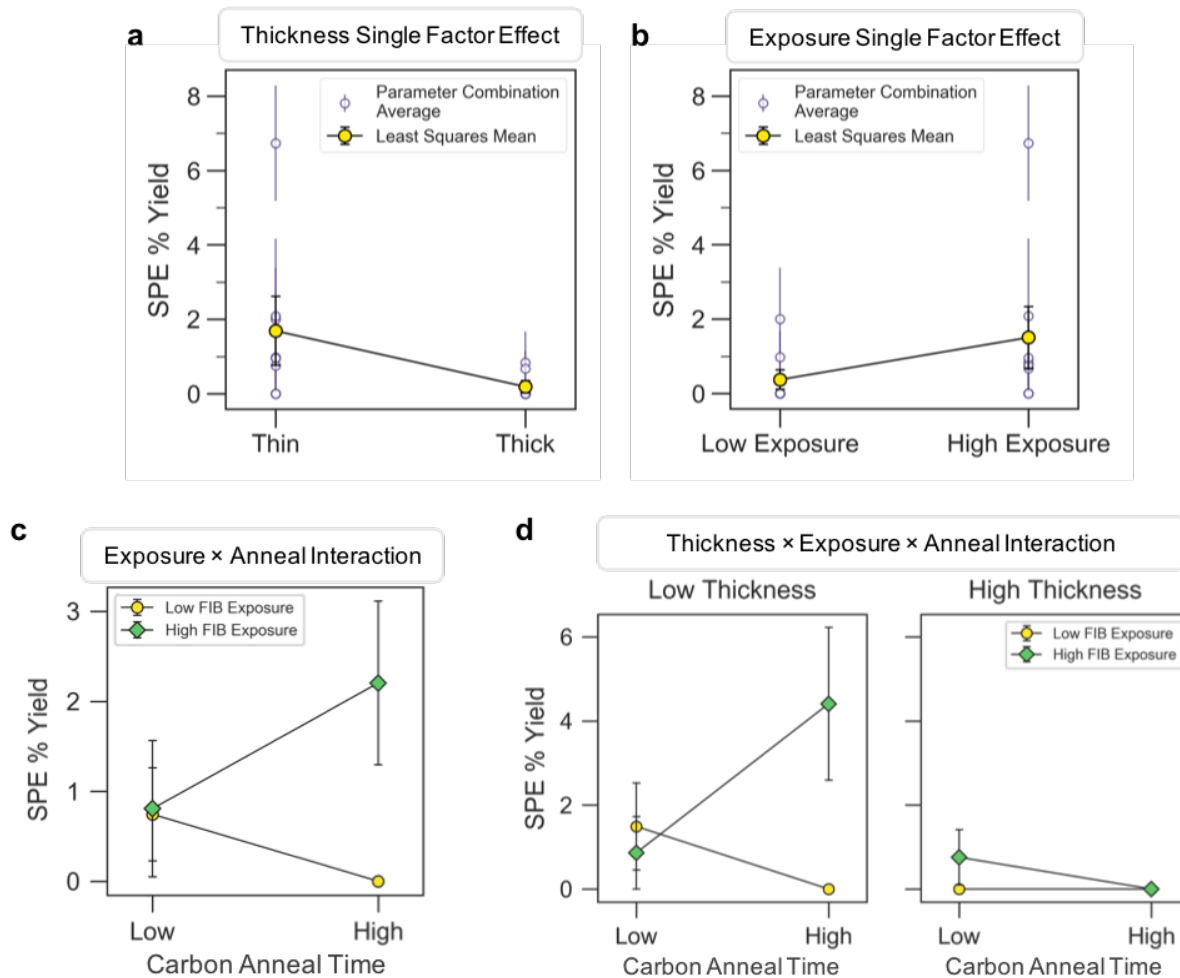


Figure 2.4. Parameters and interactions that influence SPE yield (c) Effect of hBN thickness on SPE yield. Closed yellow circles show least squares mean SPE yield for thin hBN and thick hBN. (d) Effect of FIB exposure time on SPE yield. Closed yellow circles show least squares mean SPE yield for low exposure and high exposure. Error bars show standard error on the mean. (e) Effect of FIB exposure-Carbon annealing interaction on SPE yield. Closed yellow circles show least squares mean SPE yield for low FIB exposure interactions and closed green circles show least squares mean SPE yield for high FIB exposure interactions. (f) Effect of hBN thickness-FIB exposure-Carbon annealing interaction on SPE yield. Left panel shows thin hBN interactions and right panel shows thick hBN interactions. Closed yellow circles show least squares mean SPE yield for low FIB exposure interactions and closed green circles show least squares mean SPE yield for high FIB exposure interactions. Error bars show standard error on the mean.

on thinner flakes, this effect was enhanced, while on thicker flakes, this effect was reversed, indicating a strong hBN thickness, FIB exposure time, and carbon annealing time interaction effect [Supplementary information Table 2.5 F-test, $p = 0.005$] [Figure 2.4(d)].

Based on the results of this factor screening, we established that the optimal hBN thickness to fabricate SPEs with this process is 10-19 nm. Furthermore, since SPE yield depends strongly on the interaction of FIB exposure and carbon annealing times, we can more finely tune this technique by sweeping those parameters. We postulate that balancing the concentration of vacancy defects and carbon impurity atoms is essential to engineering carbon-based quantum emitters in pristine hBN and increasing SPE yield.

To optimize emitter yield with this technique, we explored the interaction of FIB exposure and carbon annealing for four FIB exposure times (1.3 ms, 2.5 ms, 3.8 ms, 5 ms) and five carbon annealing times (20 min, 75 min, 150 min, 300 min, 720 min) in order to cover the range within the two extreme values chosen for the factor screening. For more details about the experimental design, refer to **Supplementary information Figure 2.14**.

Our technique successfully created color centers for 13 of the 18 FIB exposure-carbon annealing time combinations. We observed that longer carbon annealing decreased SPE yield for shorter FIB exposure times and increased SPE yield for longer exposure [**Figure 2.5(a)**]. This behavior agrees with the factor screening results. We found the highest SPE yields on regions exposed for 5.0 ms and annealed for 5 hr, with average SPE yield of 0.1146 ± 0.0094 SPEs/patterned site—approximately twice the yield produced by the best factor screening parameters [**Supplementary information Table 2.8** Student's t test: $p < 0.0001$]. Four additional FIB exposure-carbon annealing time combinations yielded quantum emitters at patterned sites [**Supplementary information Table 2.7** Dunett test with no FIB no CVD control: $p < 0.0001$], **(B)** 3.8 ms:2.5 hr, **(C)** 3.8 ms:5 hr, **(D)** 2.5 ms:20 min, **(E)** 5.0 ms:12 hr [**Figure 2.5(b)**].

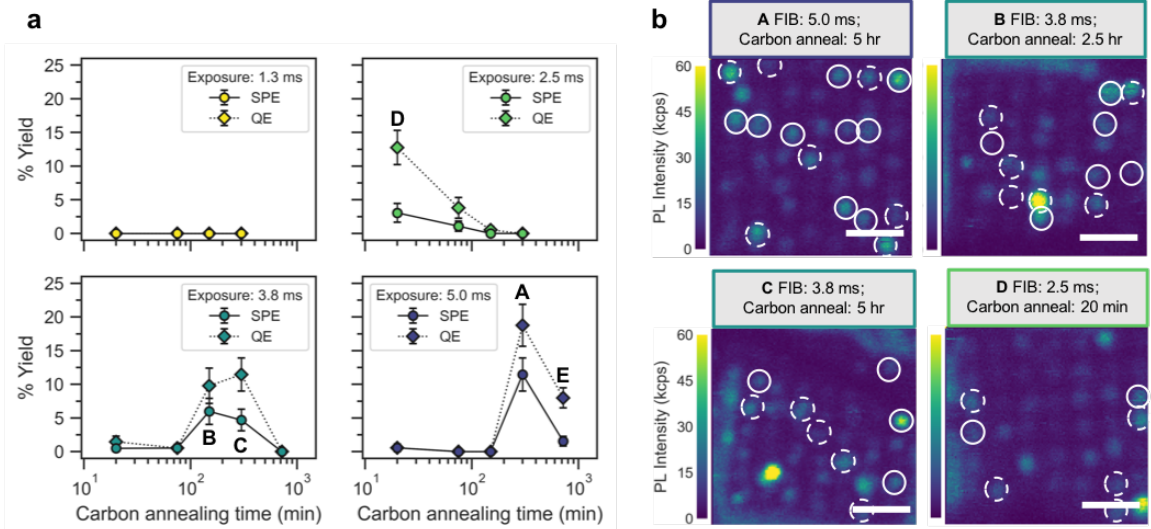


Figure 2.5. Optimizing SPE yield via FIB exposure and carbon annealing interaction (a) Interaction plots showing mean SPE and mean QE yield for samples processed under the same optimization conditions. The conditions that on average produce the highest number of SPEs and QEs are labeled with A being the conditions that produces the highest number of emitters on average, B the second highest, and so on. (b) Representative PL maps for the conditions that produce the 4 highest number of emitters on average. Scale Bar: 2 μm

While the current, most persistent need for integrating quantum emitters into photonic technologies is to optimize the yield of SPEs at deterministic locations, it is also essential to characterize the influence of the fabrication technique on optical characteristics such as single-photon purity and ZPL energy that determine the utility of the emitters in these technologies. To determine if the particular combination of FIB exposure and carbon annealing times impact the single-photon purity, we characterized 157 emitters with $g^2(0) < 1$ on regions subjected to 12 of the 18 possible exposure and annealing combinations, with 65.6% of those emitters on regions subjected to the top five combinations listed above as producing the highest QE yields. We found that emitters fabricated with conditions (A) and (B) had average $g^2(0) < 0.5$, while regions subjected to conditions (C), (D), and (E) had average $g^2(0) > 0.5$ [Figure 2.6(a)]. Furthermore, we observed that for constant FIB exposure level, longer carbon annealing time increased the average $g^2(0)$ [Supplementary information Table 2.10 B-C Student's t test $0.436 \pm 0.038 - 0.631 \pm 0.033$: $p = 0.0002$, A-E Student's t test $0.477 \pm 0.028 - 0.698 \pm 0.028$: $p < 0.0001$].

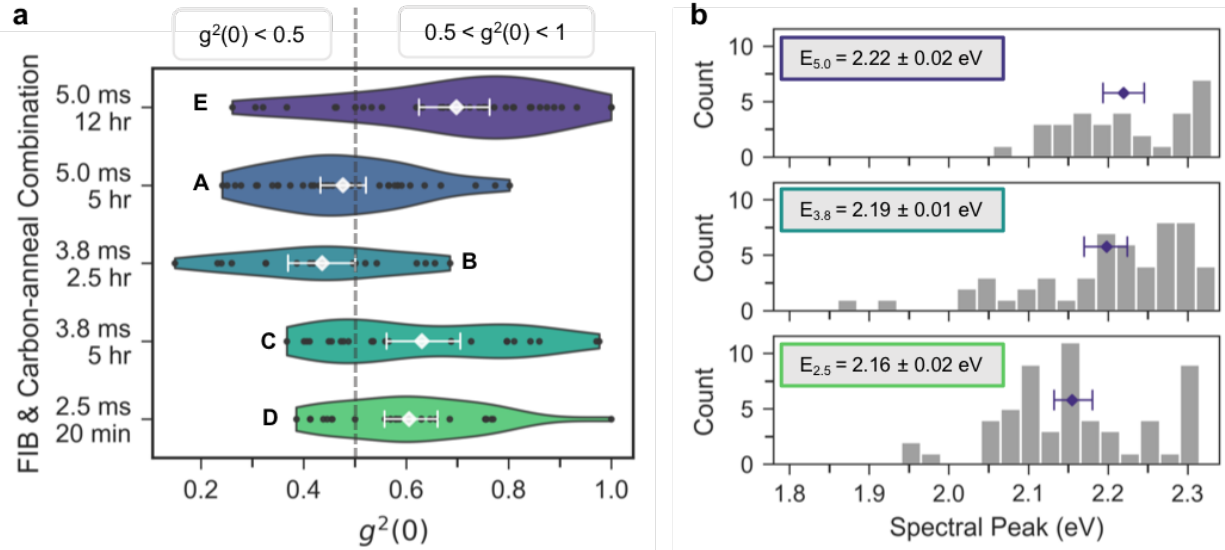


Figure 2.6. Tailoring antibunching at $g^2(0)$ and emission energy (a) $g^2(0)$ value distribution for parameter combinations that yielded the most QEs, where A, B, C, D, E labels correspond to the same labels in Figure 2.3. Diamond with error bars for each experiment represent the mean $g^2(0)$ and standard error on mean. Dashed lines mark single-photon emitter threshold $g^2(0) = 0.5$ (b) ZPL distribution by FIB exposure level. Purple diamond with error bars for each level represent mean ZPL and standard error on the mean.

These results demonstrate that we can tailor the quantum purity of emitters fabricated with this technique by adjusting the exposure time and carbon annealing time.

To determine if we can similarly tailor the ZPL, we collected spectra from 143 color centers and observed ZPL within the expected visible range for hBN QEs. We found that ZPL and ZPL distributions varied due to FIB exposure time [Figure 2.6(b)]. Although the average ZPL of emitters patterned with the 2 highest FIB exposure times were similar [Supplementary information Table 2.11 5.0 ms-3.8 ms Student's t test $2.22 \pm 0.02 - 2.19 \pm 0.01$: $p = 0.312$], the average ZPL for emitters patterned with the second FIB level shifted to 2.16 ± 0.02 eV [Supplementary information Table 2.11 3.8 ms-2.5 ms Student's t test: $p = 0.0164$, 5.0 ms-2.5 ms Student's t test: $p = 0.0022$]. This difference could indicate variations in the types of defects and defect complexes, local strain gradients, or substrate effects that are dependent on the specific exposure and annealing combinations.

2.3. Conclusions

In this work, we engineered single photon sources in pristine hBN by combining FIB patterning and carbon diffusion via CVD of nanocrystalline graphite as a carbon source. By exploring a portion of the rich parameter space of this technique, we found multiple combinations of FIB exposure dose and diffusion time that successfully created SPEs and determined that crystals < 20 nm, FIB exposure for 5.0 ms, and carbon annealing for 5 hours lead to the highest yield of SPEs, with other combinations providing a means to produce SPEs with different average purity and ZPL range. Further work to characterize the influence of these parameters on material properties such as sputtering damage and vacancy distributions could help identify the classes of defects created with this technique, thereby leading to greater control over SPE creation and photophysical properties. This adjustable fabrication technique provides an avenue to tunable SPE properties that can be applied to a wider range of integrated quantum photonics applications.

2.4. Methods

Sample Fabrication

All experiments: The samples studied were prepared on Si wafers with 300 nm of thermal wet oxide from University Wafer. Wafers were diced into 7 mm by 7 mm chips and patterned with a number array via laser writing and reactive ion etching for labeling purposes only. After the labeling process, chips were cleaned in acetone sonication bath for 5 min and IPA sonication bath for 5 min. Cleaned chips were exposed to 300 mTorr O_2 plasma at 300 W RF power in a March plasma cleaner for 1 min to create a hydrophilic surface for material transfer adhesion. HPHT hBN crystals were prepared for exfoliation transfer on thermal release tape. The thermal release tape with hBN crystals was placed on the chip surface immediately after oxygen plasma

exposure. The chip-hBN-tape stack was placed on a 120°C hot plate for 5 minutes to release the tape from the chip-hBN stack. The sample was cleaned of any tape residue in a tube furnace open to air at 500°C for 3 hours with no gas flow.

FIB only, FIB+CVD experiments: FIB exposure to create vacancy and edge defects occurred in a FEI Helios Dual Beam with gallium ion source. Prior to sample loading, the chamber was plasma cleaned with air for 5 min. The FIB was set to acceleration voltage of 20 keV and beam current of 59 pA. The circular pattern exposure mask was drawn directly in the FIB window of the execution software interface with desired circle diameter of either 250 nm or 500 nm depending on the experiment. Once the pattern was drawn in the software, an array of the circle patterns with 1 μm pitch was made. The exposure time was set in the pattern settings of the execution software to 1.3 ms, 2.5 ms, 3.8 ms, or 5.0 ms depending on the experiment. When the desired hBN flake was located via SEM, the FIB pattern was executed, exposing only the regions of the material as determined in the circular array pattern exposure mask.

CVD only, FIB+CVD experiments: Samples immediately underwent the CVD process to introduce carbon into the crystal environment. Samples were loaded into the tube furnace connected to vacuum system and the system was evacuated to a base pressure of ~ 30 mTorr. When the base pressure was reached, the C_2H_4 , Ar, and H_2 gas lines were purged. Once the base pressure was reached again, the furnace temperature setpoint was ramped to 1000°C over 30 minutes under 50 sccm Ar. After 40 minutes, the temperature was held at 1000°C for 20 minutes, 75 minutes, 150 minutes, or 300 minutes depending on the experiment. During this time, the gas flow was 35 sccm ethylene, 2 sccm H_2 , and 5 sccm Ar at 1 Torr. At the end of the designated time, the furnace temperature setpoint was set to 0°C and the sample was allowed to gradually cool under 50 sccm Ar. When the temperature readout reached 400°C, the furnace lid was

opened to speed up the rest of the cooling process. The CVD process was ended when the temperature readout reaches 200°C. The vacuum system was vented, and samples were removed.

FIB only, CVD only, and FIB+CVD experiments: To remove residual carbon on the surface, the samples underwent a cleaning anneal at 850°C for 30 min under 5 sccm O₂.

Characterization

Atomic Force Microscopy: After material transfer and 500°C cleaning anneal, the hBN flake thickness was characterized by taking a line cut measurement of a few micron square area AFM image taken via Bruker Dimension FastScan AFM in Tapping Mode.

Optical Characterization: Confocal PL images were taken to identify spots of photoluminescence in a home-built confocal microscope with 532 nm solid state laser (OptoEngine) excitation, 100× 0.7 NA objective, dichroic beam splitter, and 550 nm long pass filter. Emission was coupled to a ThorLabs fiber optic 50:50 beam splitter and photon counts for each path were detected by avalanche photodiodes (Micro Photon Devices). PL images show the signal from one APD. Time correlated photon counting was performed in a Hanbury-Brown and Twiss experiment using the signal from both APDs sent to a PicoQuant TimeHarp 260. PL spectra of emitting sites and Raman of material were collected in a commercial WITec alpha300 spectrometer equipped with a Peltier-cooled Andor iDus CCD.

Statistical Analysis: Characterized regions were divided into 4 μm^2 segments, which corresponds to 4 FIB patterned locations for patterned samples because we patterned exactly one circle per 1 μm^2 . To calculate mean SPE (QE) density or yield, we recorded the number of emission sites with $g^2(0) < 0.5$ ($g^2(0) < 1$) in each 4 μm^2 region and averaged all regions processed with a given combination of experimental input factors. To calculate the mean PL map intensity, we converted all confocal image points from kcps to cts by the detection bin size of 0.1

s and plotted in grayscale where 0 corresponded to the minimum counts value and 255 corresponded to the maximum counts value for the given PL map. We recorded the mean pixel height in ImageJ for each region, converted it to the mean PL intensity in counts, and averaged all regions processed with a given combination of experimental input factors. To elucidate which input factors influence successful SPE creation alone or combined with other input factors and obtain significance values, we performed a Full Model Effects Test on the number of SPEs counted, number of QEs counted, and average PL in each $4 \mu\text{m}^2$ region.

All statistical tests were performed in SAS JMP 15.1 statistical analysis software. Factor Screening (4-factor 2-level) Full Model Effects Test and all ANOVA tests (test specified in main text i.e. Student's t-test, Tukey-Kramer HSD, or Dunnett test) were performed with significance level $\alpha = 0.05$. Prior to all statistical tests for SPE Yield, QE Yield, and Region PL Counts, we performed a variance stabilizing transform for Poissonian data:

$$\tilde{x} = \sqrt{x} \quad (2.3)$$

2.5. Supplementary information

Control experiments

To test if both FIB milling and carbon annealing are necessary to create localized quantum emitters, we compared the combined process to the following 2 treatments: (1) FIB milled only without carbon anneal and (2) carbon anneal only with no FIB milling, as well as to a pristine hBN control [Figure 2.7]. We used a 5-hour carbon deposition and anneal time for both the CVD only process and the combined process. Our CVD process was performed at 1000°C due to the temperature dependent diffusion constant of carbon in semiconductor and insulating materials⁵². Recent works have also shown that this temperature is optimal for carbon-based CVD for emitter creation in hBN⁴¹. hBN flakes characterized for CVD only experiments were on

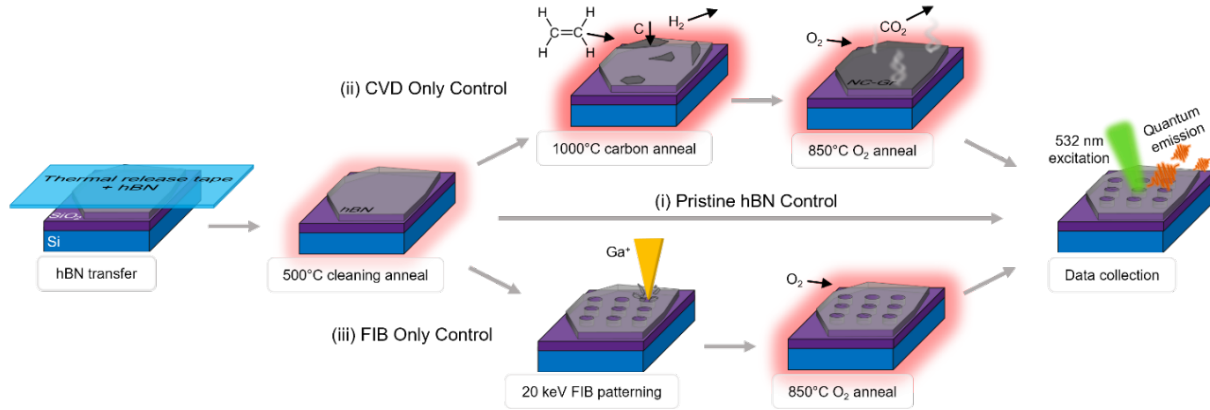


Figure 2.7. Process flow diagrams for control experiments (i) pristine hBN control, (ii) carbon annealing (CVD) only control, (iii) FIB only control. All samples underwent the same transfer and cleaning process.

the same chips as those characterized for FIB+CVD experiments so may have been exposed to residual charging effects, but were not directly patterned via FIB exposure nor imaged via SEM. Samples processed with FIB milling that skip the carbon anneal still undergo the 30 min O₂ anneal at 850°C even though there is no need to remove carbon from the surface because we found this to be required to activate emitters in our previous work.

Table 2.1 shows the average SPE yield per μm^2 for each control experiment, including a pristine hBN control. Carbon annealing alone produced yields comparable to those found by Lyu et. al. using methane feedstock gas in a similar carbon annealing process⁴¹. In **Table 2.2**, we report p-values for Student's t and Tukey-Kramer HSD Means Comparison Tests for the optimized combined process parameters with each and all control experiments.

Table 2.1. Control Experiments Results for average SPE yield. 1 SPE per μm^2 on pristine and CVD only controls is analogous to 100% yield on FIB only control and combined process samples because we patterned 1 site per μm^2 .

Experiment	Studied region	SPE Yield (Mean \pm Std Err)
Pristine hBN Control	192 μm^2	0
CVD Only Control	240 μm^2	0.0125 \pm 0.0071 / μm^2
FIB Only Control	1200 sites	0.0008 \pm 0.0024 / μm^2 (0.08 %)

Table 2.2. Control Experiments – SPE Yield Mean Comparison Tests $\alpha = 0.05$ significance level, unbalanced, unequal variance

Experiment 1 – Experiment 2	Difference	Standard Error Difference	p-value (Student's t Each Pair)	p-value (Tukey-Kramer HSD All Pairs)
Combined Process – Pristine hBN Control	0.3973	0.0410	< 0.0001	< 0.0001
Combined Process – FIB Only Control	0.3940	0.0313	< 0.0001	< 0.0001
Combined Process – CVD Only Control	0.3473	0.0389	< 0.0001	< 0.0001
CVD Only Control – Pristine hBN Control	0.0500	0.0389	0.1997	0.5734
CVD Only Control – FIB Only Control	0.0467	0.0284	0.1014	0.3565
FIB Only Control – Pristine hBN Control	0.0033	0.0313	0.9151	0.9996

Raman characterization of graphite diffusion source deposition

We confirmed the introduction of carbon via Raman spectroscopy with 532 nm excitation [Figure 2.8]. The observed nanocrystalline graphite D and G Raman peaks demonstrates that during the carbon annealing process, ethylene successfully decomposed, depositing carbon on the surface⁵³. Therefore, we assert that elemental carbon was present during the anneal process. The visibility of the hBN Raman peak⁵⁴ following the full fabrication process demonstrates that the oxygen anneal removed the deposited graphite and confirms that the process did not change the overall hBN crystal composition or structure.

Pattern localization

On samples patterned using the combined process, we observed spots separated by an average pitch of $0.934 \pm 0.013 \mu\text{m}$, found via average centroid calculation of a background subtracted PL scan [Figure 2.9]. This value is slightly out of range of the $1 \mu\text{m}$ input FIB patterning pitch. This discrepancy could be due to FIB stage calibration, sample tilt during milling, confocal fast scanning mirror calibration, or sample tilt during confocal data collection. However, these scans show qualitative agreement to the periodicity of the pattern, showing

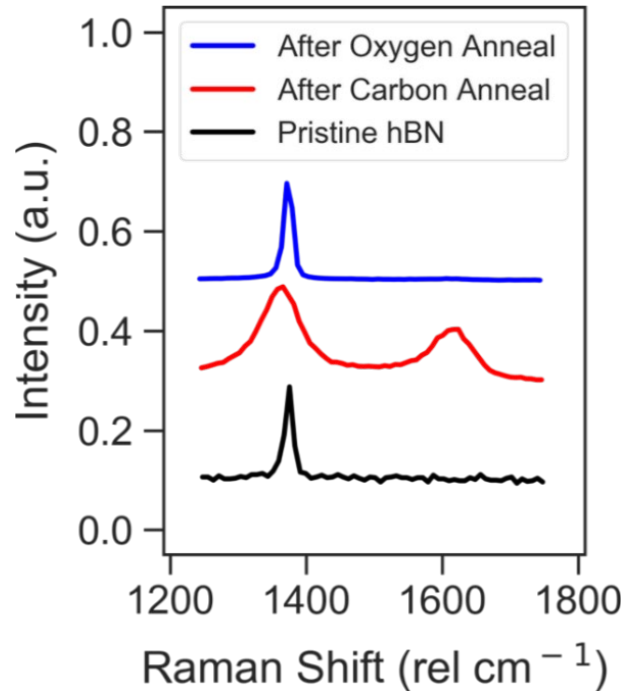


Figure 2.8. Raman characterization of diffusion source deposition Peaks showing hBN peak (1370 rel. cm^{-1}) for the cleaned pristine flake (black line), nanocrystalline-graphite D (1360 rel. cm^{-1}) and G (1610 rel. cm^{-1}) peaks after carbon annealing (red line), and hBN peak again after removing NC-Gr in the oxygen anneal

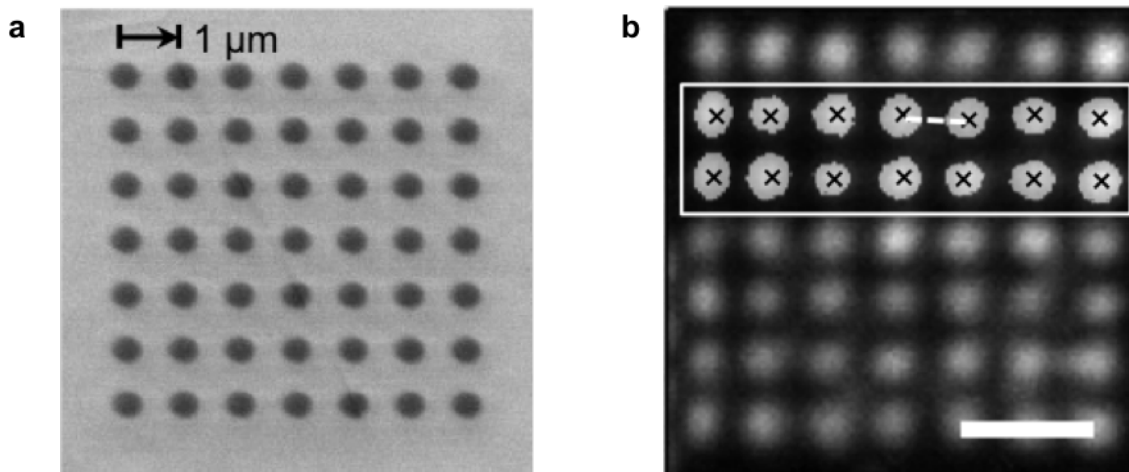


Figure 2.9. SEM and PL centroid analysis to localize patterned SPEs (a) SEM image of FIB patterned 500 nm diameter holes in hBN flakes, separated by 1 μm pitch. (b) Grayscale confocal PL scan image showing fluorescent emission at FIB patterned locations after the combined FIB and carbon annealing process. Inset: PL image was background subtracted and ImageJ software found all “particles”, outlined the closed circles, and recorded the centroid position of each spot. The “x” of each spot marks the centroid position and the dashed line shows an example displacement measurement to give emission location pitch. Scale bar: 2 μm

$n \times n$ emission sites when we mill an $n \times n$ pattern. Therefore, we assert this technique as a method to produce localized, patterned emission sites.

Factor screening experiments

Parameters: We chose four experimental factors that are straightforward to control and chose qualitative “high” and “low” regimes justified by past work or observations prior to SPE characterization. Demonstrations of these parameter values are shown in **Figure 2.10**.

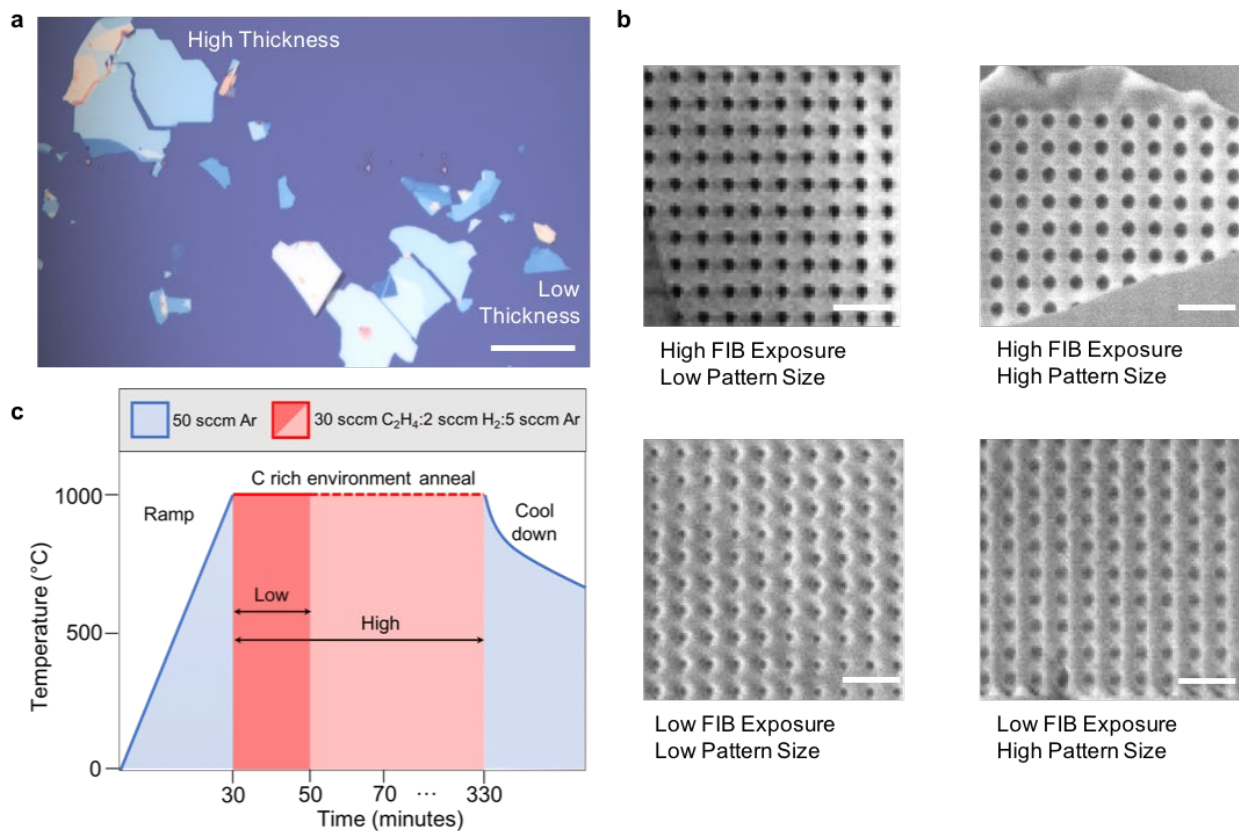


Figure 2.10. Fabrication parameter factor screening details (a) Optical microscope image showing hBN flakes with different optical contrasts due to thickness dependence of thin film interference (High: labeled “thick” during optical inspection with mean \pm s.d. = 28.47 ± 5.42 nm, Low: labeled “thin” with mean \pm s.d. = 14.59 ± 4.81 nm). Scale bar: $30 \mu\text{m}$), (b) SEM images showing differences in FIB pattern size (high: 500 nm, low: 250 nm), and FIB exposure time (high: 3.8 ms, low: 2.5 ms). Scale bars: $2 \mu\text{m}$, (c) CVD process parameters as a function of time for carbon annealing step to facilitate the deposition and diffusion of carbon impurities (high: 300 min, low: 20 min).

The hBN thickness is a natural parameter to vary because our straightforward transfer method produces a wide range of hBN flake thicknesses. Furthermore, previous studies cite material thickness as an influential factor in QE stability⁵⁵. We placed hBN flakes into “high” or “low” regime for our factor screening experiment based on qualitative optical contrast. Then, we measured the thickness of individual hBN flakes via Atomic Force Microscopy (AFM), finding that flakes placed in the “high” regime were > 20 nm and those placed in the “low” regime were < 20 nm.

We chose to vary the FIB pattern size to test the lower limit of our QE localizing abilities with this method. We set this parameter in the FIB pattern software by varying the pattern diameter. A 500 nm pattern size was chosen as our “high” based on [NL paper] and 250 nm pattern size was chosen as our “low” based on the expected resolution limits of the FIB patterning and confocal microscope characterization systems.

To control the amount of damage done to the material in the form of vacancies, Ga⁺ implantation, and sputtering to create milled edges, we chose to vary the FIB exposure time, thereby controlling the ion fluence for a constant energy and current. We defaulted to the FIB energy and current determined as optimal from our previous work²³, detailed in Methods. Furthermore, recent work utilizing ion implantation to create SPEs in hBN showed that ion fluence has a larger influence on the SPE density than ion energy⁵⁶. We chose “high” and “low” values of 3.8 ms and 2.5 ms respectively, because these exposure times produced distinct levels of material damage during our preliminary experiments.

CVD involves many parameters that could influence the creation of SPEs, we chose to vary the carbon annealing time in order to determine if a steady supply of carbon introduced for a long time is necessary for the creation of QEs in hBN or if a steady supply of carbon introduced

for a short time is sufficient. Furthermore, the carbon annealing time controls both the concentration of elemental carbon and the diffusion time for all defects and therefore contains valuable information within one parameter. We expected the carbon annealing time to independently and strongly influence SPE yield because the probability of forming carbon-based defects depends explicitly on the concentration of impurity atoms and therefore implicitly on the annealing time t by:

$$C(x, t) = C_s \operatorname{erfc}\left(\frac{x}{2\sqrt{Dt}}\right) \quad (2.3)$$

where x is the depth, C_s is the surface concentration of carbon impurity atoms, which is dependent on the deposition of NC graphite we observed via Raman, and D is the diffusion constant. We kept all other CVD parameters constant for experimental simplicity, but we expect that further study will elucidate the role of these parameters such as chosen carbon feedstock, gas ratios, and process pressure. We chose a “high” value of 5 hr and a “low” value of 20 min.

Data: The mean SPE Yield for all 16 factor screening combinations are shown in **Table 2.3**. The table also lists the number of sites across multiple samples patterned with each combination. Additionally, we performed Dunnett Means Comparison Test with pristine hBN control and report the p-value for each combination to determine if that particular combination successfully creates SPEs with higher yield than what would be found in unprocessed material. Furthermore, we report the results of Student’s t and Tukey-Kramer HSD Mean SPE Yield Comparison Tests for pairs that include the thin, 500 nm, 3.8 ms, 5 hr parameter combination in **Table 2.4**.

Table 2.3. Factor Screening Experiments Results for average SPE yield.

Experiment (thickness, pattern size, exposure, anneal time)	Studied region	SPE Yield (Mean±Std Err)	p-value (Dunnett with Pristine hBN Control)
Thin, 500 nm, 3.8 ms, 5 hr	208 sites	0.0673±0.0058	< 0.0001
Thin, 250 nm, 3.8 ms, 5 hr	48 sites	0.0208±0.0120	0.8784
Thin, 500 nm, 2.5 ms, 20 min	100 sites	0.0200±0.0083	0.6300
Thin, 250 nm, 2.5 ms, 20 min	204 sites	0.0098±0.0058	0.9856
Thin, 500 nm, 3.8 ms, 20 min	104 sites	0.0096±0.0082	0.9983
Thick, 250 nm, 3.8 ms, 20 min	120 sites	0.0083±0.0076	0.9994
Thin, 250 nm, 3.8 ms, 20 min	132 sites	0.0076±0.0073	0.9997
Thick, 500 nm, 3.8 ms, 20 min	296 sites	0.0068±0.0068	0.9993
Thin, 500 nm, 2.5 ms, 5 hr	196 sites	0	1
Thin, 250 nm, 2.5 ms, 5 hr	32 sites	0	1
Thick, 500 nm, 2.5 ms, 5 hr	84 sites	0	1
Thick, 250 nm, 2.5 ms, 5 hr	92 sites	0	1
Thick, 500 nm, 2.5 ms, 20 min	124 sites	0	1
Thick, 250 nm, 2.5 ms, 20 min	60 sites	0	1
Thick, 500 nm, 3.8 ms, 5 hr	144 sites	0	1
Thick, 250 nm, 3.8 ms, 5 hr	148 sites	0	1

Table 2.4. Thin, 500 nm, 3.8 ms, 5 hr – Mean SPE Yield Comparison Tests $\alpha = 0.05$ significance level, unbalanced, unequal variance. Experiment labels given according to key in **Figure 2.3(b)**

Experiment 1 – Experiment 2 (thickness, pattern size, exposure, anneal time)	Difference	Standard Error Difference	p-value (Student's t Each Pair)	p-value (Tukey-Kramer HSD All Pairs)
-+++ – ---+	0.2692	0.0717	0.0002	0.0197
-+++ – -+-+	0.2692	0.0375	< 0.0001	< 0.0001
-+++ – +---	0.2692	0.0553	< 0.0001	0.0002
-+++ – +--+	0.2692	0.0472	< 0.0001	< 0.0001
-+++ – +-++	0.2692	0.0406	< 0.0001	< 0.0001
-+++ – ++--	0.2692	0.0428	< 0.0001	< 0.0001
-+++ – ++++	0.2692	0.0488	< 0.0001	< 0.0001
-+++ – +++-	0.2692	0.0409	< 0.0001	< 0.0001
-+++ – +++-	0.2422	0.0341	< 0.0001	< 0.0001
-+++ – --+-	0.2389	0.0420	< 0.0001	< 0.0001
-+++ – +-+-	0.2358	0.0432	< 0.0001	< 0.0001
-+++ – -+--	0.2307	0.0453	< 0.0001	< 0.0001
-+++ – ----	0.2300	0.0372	< 0.0001	< 0.0001
-+++ – -+--	0.1892	0.0459	< 0.0001	0.0050
-+++ – ---+	0.1858	0.0604	0.0022	0.1565

Full Model Effects Test: We report results from the SPE Yield Full Model Effects test in **Table 2.5**, including both the effect size and p-value, listed in order by p-value. Interaction plots for all single factor, 2-factor, and 3-factor effects for SPE Yield are displayed in **Figures 2.11-2.13**.

Table 2.5. Factor Screening Full Model Effects Test for Variance Transformed Number of SPEs per 4 patterned sites $\alpha = 0.05$ significance level, unbalanced, unequal variance.

Input Factor or Interaction	Effect Size (F)	p-value
hBN thickness	8.24	0.004
hBN thickness × FIB exposure time × Carbon annealing time	7.89	0.005
FIB exposure	4.85	0.028
FIB exposure × Carbon annealing time	4.17	0.042
hBN thickness × FIB exposure time	2.06	0.152
hBN thickness × FIB pattern size	2.05	0.153
FIB pattern size	1.95	0.164
hBN thickness × Carbon annealing time	1.89	0.170
FIB exposure time × FIB pattern size × Carbon annealing time	1.78	0.183
hBN thickness × FIB exposure time × FIB pattern size × Carbon annealing time	1.69	0.195
hBN thickness × FIB exposure time × FIB pattern size	0.89	0.347
FIB exposure × FIB pattern size	0.82	0.366
FIB pattern size × Carbon annealing time	0.71	0.400
hBN thickness × FIB pattern size × Carbon annealing time	0.65	0.421
Carbon annealing time	0.37	0.544

Single Factor Effects

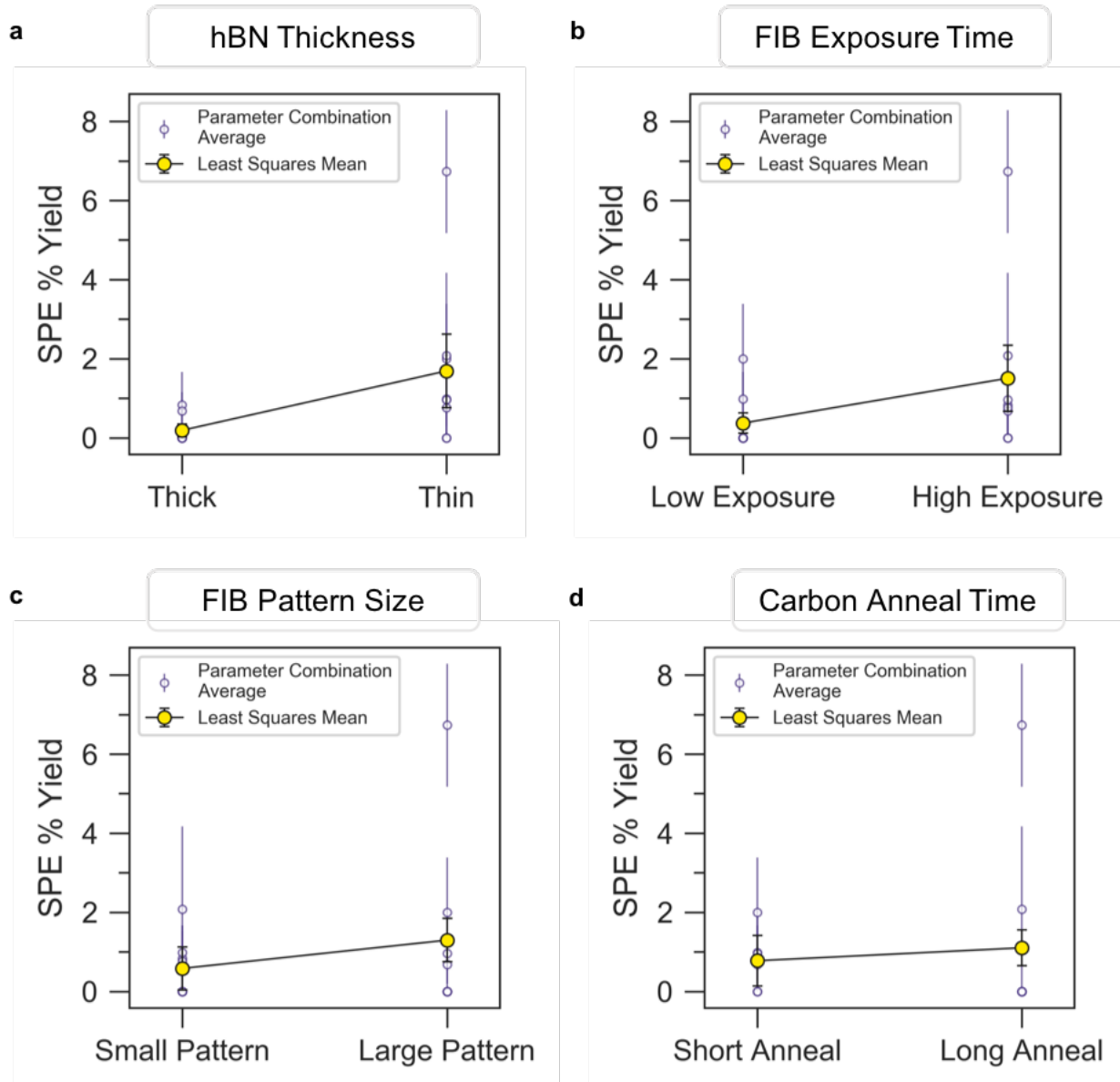


Figure 2.11. Plots for single factor effects on SPE yield for 2 level factor screening showing least squares means by level and parameter combination averages for each factor (a) hBN thickness (b) FIB exposure time, (c) FIB pattern size, (d) carbon anneal time. Error bars are standard error on mean.

2-Factor Interaction Effects

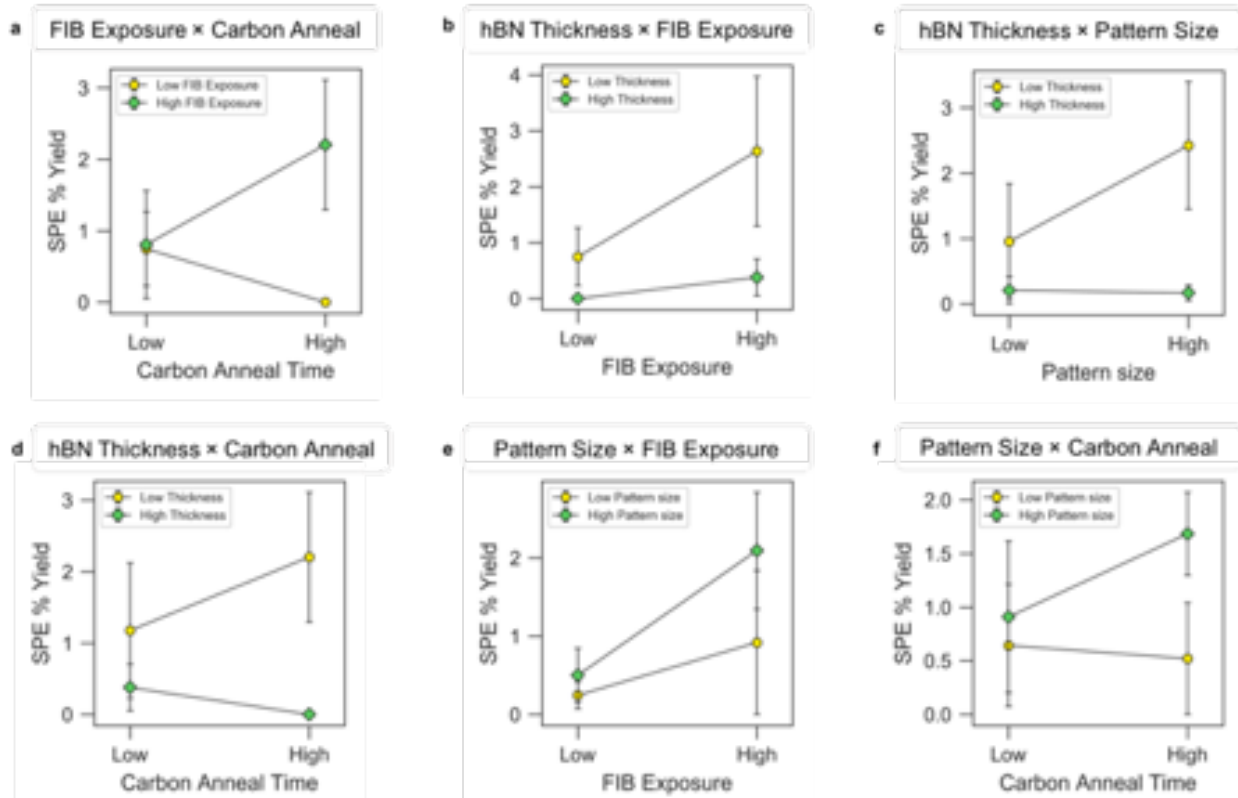


Figure 2.12. Plots for two-factor interaction effects on SPE yield for 2 level factor screening showing least squares means by level combination for each interaction (a) FIB exposure and carbon anneal time (b) hBN thickness and FIB exposure (c) hBN thickness and pattern size (d) hBN thickness and carbon anneal (e) pattern size and FIB exposure (f) pattern size and carbon anneal time. Points are least squares mean of parameter combinations that include the labeled interaction. Error bars are standard error on mean.

3-Factor Interaction Effects

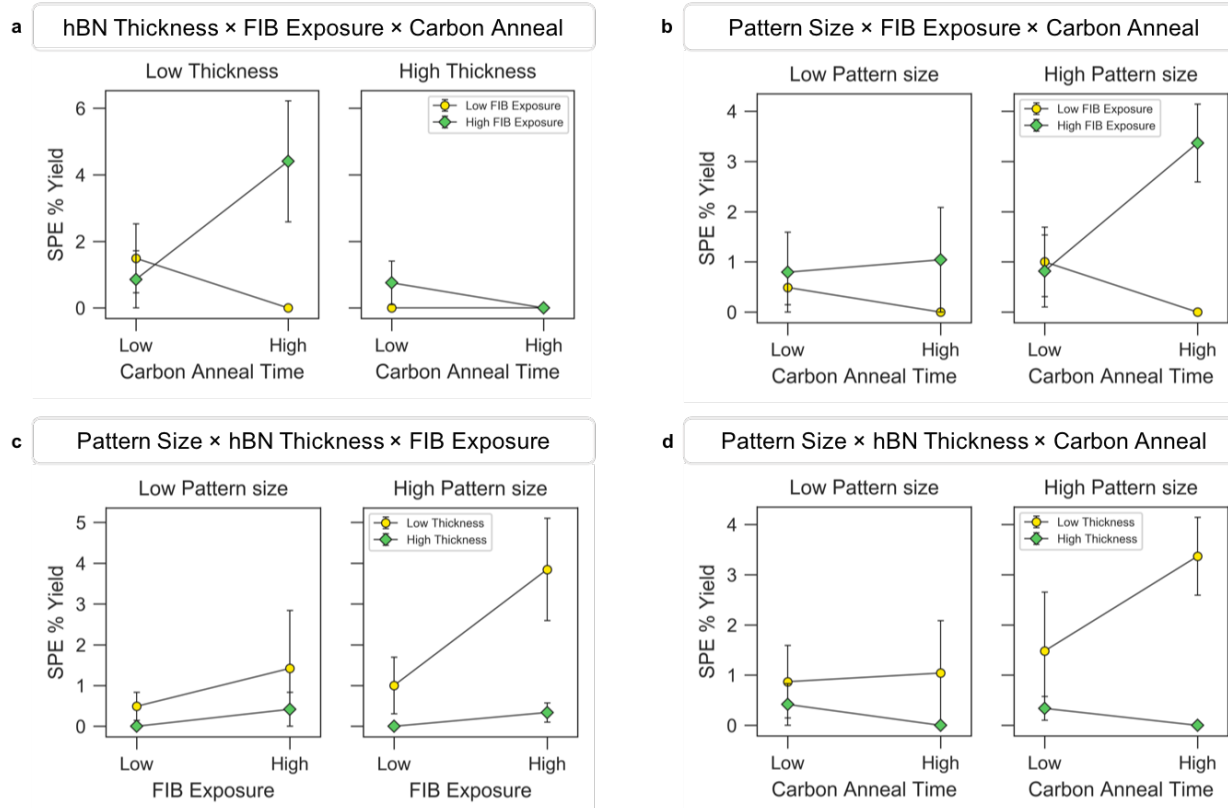


Figure 2.13. Plots for three-factor interaction effects on SPE yield for 2 level factor screening showing least squares means by level combination for each interaction (a) hBN thickness, FIB exposure, and carbon anneal time (b) pattern size, FIB exposure, and carbon anneal time (c) pattern size, hBN thickness, and FIB exposure (d) pattern size, hBN thickness, and carbon anneal time. Points are least squares mean of parameter combinations that include the labeled interaction. Error bars are standard error on mean.

Optimization

Parameters: Carbon annealing and FIB exposure levels and processes are shown in **Figure 2.14**. Based on the factor screening results, we only exposed flakes with thickness in the range of 11-18 nm and only patterned circles of 500 nm diameter. For each substrate, we found four flakes of suitable area in the prescribed thickness range determined as optimal during Factor Screening. On each flake, we patterned one 7×7 array of circles at each dose. We randomized the order of the four doses patterned on each flake to minimize any pattern order-dependent

variance in measured response variables. The lowest value of 1.3 ms was the lowest time possible given the fixed pattern size, current, and dwell time specified for the Helios Dual Beam FIB system used for this work. Exposure times longer than 5 ms in past experiments milled through hBN within this thickness range completely and began milling SiO₂. Given the constant pattern area for this set of fabrication, we can also refer to the FIB exposure time parameter by the ion fluence [Table 2.6] calculated by:

$$Fluence = \frac{I_{beam} \times t_{exposed}}{e^+ \times A_{pattern}} \quad (2.4)$$

Where $I_{beam} = 59 \text{ pA}$, $e^+ = 1.6E - 7 \text{ pC}$, and $A_{pattern} = \pi \left(\frac{500 \text{ nm}}{2} \right)^2$

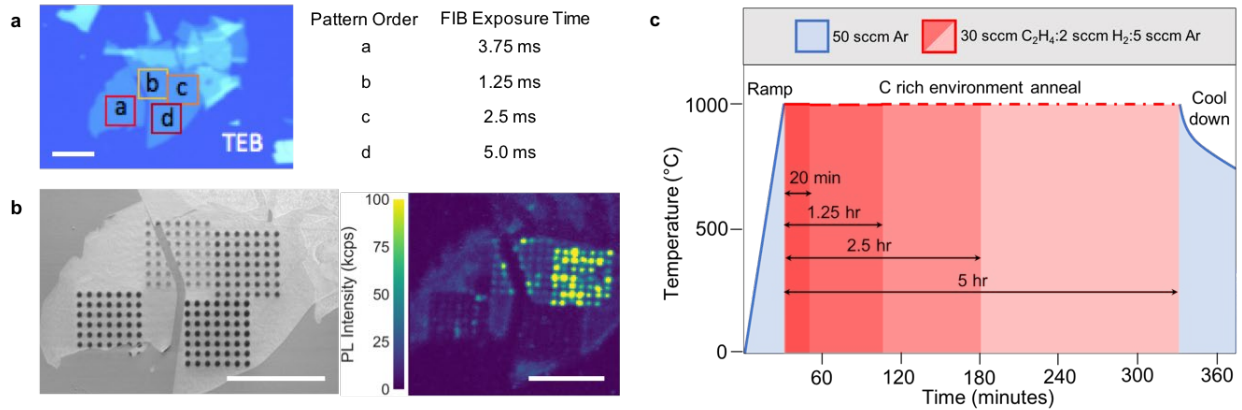


Figure 2.14. FIB exposure and carbon annealing interaction optimization parameters, (a) Optical microscope image of hBN flake marked with array locations for each FIB level. Pattern order was random to randomize the changes to the FIB exposure time (b) SEM image and corresponding confocal PL scan of patterned flake shown in (a). Scale bars for (a) and (b): 10 μm. (c) CVD process showing the 4 carbon anneal time levels

Table 2.6. Ion Fluences for Optimization FIB Exposure Levels calculated according to Equation 2.4

FIB Exposure Level	Exposure Time (ms)	Ion Fluence (cm ⁻²)
1	1.25	2.35×10 ¹⁴
2	2.5	4.70×10 ¹⁴
3	3.75	7.04×10 ¹⁴
4	5.0	9.39×10 ¹⁴

Data: The mean SPE Yield, QE Yield, and Region PL for all 18 optimization combinations are shown in **Table 2.7**. The table also lists the number of sites across multiple samples patterned with each combination. Additionally, we performed Dunnett Means Comparison Test with pristine hBN control and report the p-value for each combination to determine if that particular combination successfully creates SPEs and QEs (PL) with higher yield (intensity) than what would be found in unprocessed material. Furthermore, we report the results of Student's t and Tukey-Kramer HSD Mean SPE Yield Comparison Tests for pairs that include parameter combinations where the SPE yield was greater than zero in **Table 2.8**. We also report the results of Student's t and Tukey-Kramer HSD Mean Region PL Grouped by Anneal Time Comparison Tests for pairs that include parameter combinations in **Table 2.9**.

Table 2.7. Optimization Experiments Results for average SPE yield, average QE yield, and Region PL intensity. $\alpha = 0.05$ significance level

Experiment (FIB exposure, carbon anneal time)	Number of patterned sites	SPE Yield (Mean \pm Std Err)	p-value (Dunnett with Pristine hBN Control)	QE Yield (Mean \pm Std Err)	p-value (Dunnett with Pristine hBN Control)	Region PL [cts] (Mean \pm Std Err)	p-value (Dunnett with Pristine hBN Control)
5.0 ms, 5 hr	192	0.1146\pm0.0094	< 0.0001	0.1875\pm0.0144	< 0.0001	46.03 \pm 2.56	0.9716
3.8 ms, 2.5 hr	184	0.0598 \pm 0.0096	< 0.0001	0.0978\pm0.0147	< 0.0001	86.15 \pm 10.30	0.2305
3.8 ms, 5 hr	192	0.0469 \pm 0.0094	0.0014	0.1094\pm0.0144	< 0.0001	186.37 \pm 25.08	0.0004
2.5 ms, 20 min	196	0.0305 \pm 0.0093	0.1318	0.1453\pm0.0142	< 0.0001	239.80 \pm 48.36	0.0001
5.0 ms, 12 hr	388	0.0155 \pm 0.0054	0.7758	0.0799\pm0.0083	< 0.0001	108.63 \pm 20.79	0.0525
2.5 ms, 1.25 hr	184	0.0109 \pm 0.0096	0.9877	0.0380 \pm 0.0147	0.2691	393.22 \pm 46.33	< 0.0001
5.0 ms, 20 min	176	0.0057 \pm 0.0098	1.0000	0.0057 \pm 0.0150	1.0000	28.62 \pm 0.77	1.0000
3.8 ms, 1.25 hr	184	0.0053 \pm 0.0095	1.0000	0.0053 \pm 0.0145	1.0000	36.16 \pm 0.67	1.0000
3.8 ms, 20 min	132	0.0050 \pm 0.0091	1.0000	0.0147 \pm 0.0140	0.911	39.06 \pm 1.67	0.9998
2.5 ms, 2.5 hr	192	0	1.0000	0.0052 \pm 0.0144	1.0000	769.81 \pm 57.56	< 0.0001
1.3 ms, 20 min	192	0	1.0000	0	1.0000	468.32 \pm 21.62	< 0.0001

Table 2.7. (continued)

Experiment (FIB exposure, carbon anneal time)	Number of patterned sites	SPE Yield (Mean±Std Err)	p-value (Dunnett with Pristine hBN Control)	QE Yield (Mean±Std Err)	p-value (Dunnett with Pristine hBN Control)	Region PL [cts] (Mean±Std Err)	p-value (Dunnett with Pristine hBN Control)
1.3 ms, 1.25 hr	192	0	1.0000	0	1.0000	298.54±26.19	< 0.0001
1.3 ms, 2.5 hr	184	0	1.0000	0	1.0000	385.09±42.60	< 0.0001
1.3 ms, 5 hr	192	0	1.0000	0	1.0000	573.44±26.55	< 0.0001
2.5 ms, 5 hr	192	0	1.0000	0	1.0000	1097.49±55.80	< 0.0001
3.8 ms, 12 hr	376	0	1.0000	0	1.0000	233.19±21.12	< 0.0001
5.0 ms, 1.25 hr	204	0	1.0000	0	1.0000	29.35±0.47	1.0000
5.0 ms, 2.5 hr	192	0	1.0000	0	1.0000	31.46±0.57	1.0000

Table 2.8. Optimization Experiments – Mean SPE Yield Comparison Tests for pairs where SPE yield > 0. $\alpha = 0.05$ significance level, unbalanced, unequal variance

Experiment 1 – Experiment 2	SPE Difference	SPE Standard Error Difference	p-value (Student's t Each Pair)	p-value (Tukey-Kramer HSD All Pairs)
4:4 – 3:1	0.3777	0.0438	< 0.0001	< 0.0001
4:4 – 3:2	0.3760	0.0447	< 0.0001	< 0.0001
4:4 – 4:1	0.3745	0.0455	< 0.0001	< 0.0001
4:4 – 2:2	0.3538	0.0449	< 0.0001	< 0.0001
4:4 – 4:5	0.3414	0.0384	< 0.0001	< 0.0001
4:4 – 2:1	0.2868	0.0442	< 0.0001	< 0.0001
4:4 – 3:4	0.2220	0.0445	< 0.0001	0.0001
3:3 – 3:1	0.1940	0.0443	< 0.0001	0.002
3:3 – 3:2	0.1923	0.0452	< 0.0001	0.0034
3:3 – 4:1	0.1909	0.0459	< 0.0001	0.0051
4:4 – 3:3	0.1836	0.0449	< 0.0001	0.0068
3:3 – 2:2	0.1701	0.0454	0.0002	0.0242
3:3 – 4:5	0.1578	0.0390	< 0.0001	0.0079
3:4 – 3:1	0.1556	0.0438	0.0004	0.0464
3:4 – 3:2	0.1540	0.0447	0.0006	0.0653
3:4 – 4:1	0.1525	0.0455	0.0008	0.0856
3:4 – 2:2	0.1318	0.0449	0.0035	0.2559
3:4 – 4:5	0.1194	0.0384	0.002	0.1687
3:3 – 2:1	0.1031	0.0447	0.0214	0.7067
2:1 – 3:1	0.0908	0.0436	0.0375	0.8464
2:1 – 3:2	0.0892	0.0445	0.0454	0.8851
2:1 – 4:1	0.0877	0.0453	0.0529	0.9121
2:1 – 2:2	0.0670	0.0447	0.1347	0.9933
3:4 – 2:1	0.0648	0.0442	0.1437	0.9948

Table 2.8 (continued)

Experiment 1 – Experiment 2	SPE Difference	SPE Standard Error Difference	p-value (Student’s t Each Pair)	p-value (Tukey-Kramer HSD All Pairs)
2:1 – 4:5	0.0546	0.0382	0.1529	0.9961
3:3 – 3:4	0.0383	0.0449	0.3941	1.0000
4:5 – 3:1	0.0362	0.0377	0.3373	1.0000
4:5 – 3:2	0.0345	0.0387	0.3731	1.0000
4:5 – 4:1	0.0330	0.0396	0.404	1.0000
2:2 – 3:1	0.0238	0.0443	0.5905	1.0000
2:2 – 3:2	0.0222	0.0452	0.6236	1.0000
2:2 – 4:1	0.0207	0.0459	0.6519	1.0000
4:5 – 2:2	0.0123	0.0390	0.752	1.0000
4:1 – 3:1	0.0031	0.0448	0.9446	1.0000
3:2 – 3:1	0.0016	0.0440	0.9698	1.0000
4:1 – 3:2	0.0014	0.0457	0.9747	1.0000

**Table 2.9. Optimization Experiments – Mean Region PL Grouped by Anneal Time
Comparison Tests $\alpha = 0.05$ significance level, unbalanced, unequal variance**

Experiment 1 – Experiment 2	PL Difference	PL Standard Error Difference	p-value (Student’s t Each Pair)	p-value (Tukey-Kramer HSD All Pairs)
2:1 – 1:1	8.66	1.04	< 0.0001	< 0.0001
2:1 – 3:1	6.37	1.02	< 0.0001	< 0.0001
2:1 – 4:1	7.24	1.06	< 0.0001	< 0.0001
1:1 – 3:1	15.03	1.03	< 0.0001	< 0.0001
1:1 – 4:1	15.90	1.06	< 0.0001	< 0.0001
3:1 – 4:1	0.87	1.05	0.4085	0.8409
2:2 – 1:2	1.32	0.999	0.1877	0.5500
2:2 – 3:2	11.93	1.00	< 0.0001	< 0.0001
2:2 – 4:2	12.52	0.98	< 0.0001	< 0.0001
1:2 – 3:2	10.61	0.99	< 0.0001	< 0.0001
1:2 – 4:2	11.20	0.97	< 0.0001	< 0.0001
3:2 – 4:2	0.59	0.98	0.5455	0.9302
2:3 – 1:3	8.40	1.08	< 0.0001	< 0.0001
2:3 – 3:3	18.21	1.08	< 0.0001	< 0.0001
2:3 – 4:3	21.23	1.07	< 0.0001	< 0.0001
1:3 – 3:3	9.81	1.09	< 0.0001	< 0.0001
1:3 – 4:3	12.82	1.08	< 0.0001	< 0.0001
3:3 – 4:3	3.02	1.08	0.0059	0.0297
2:4 – 1:4	8.93	0.98	< 0.0001	< 0.0001
2:4 – 3:4	20.34	0.98	< 0.0001	< 0.0001
2:4 – 4:4	25.90	0.98	< 0.0001	< 0.0001
1:4 – 3:4	11.41	0.98	< 0.0001	< 0.0001
1:4 – 4:4	16.97	0.98	< 0.0001	< 0.0001
3:4 – 4:4	5.56	0.98	< 0.0001	< 0.0001

$g^2(0)$ Analysis

We report the results of Student's t and Tukey-Kramer HSD Mean $g^2(0)$ Comparison Tests for the optimization parameter combinations with the 5 highest SPE/QE yields in **Table 2.10**.

Table 2.10. Top 5 Optimization Experiments – Mean $g^2(0)$ Comparison Tests $\alpha = 0.05$ significance level, unbalanced, unequal variance

Experiment 1 – Experiment 2	$g^2(0)$ Difference	$g^2(0)$ Standard Error Difference	p-value (Student's t Each Pair)	p-value (Tukey-Kramer HSD All Pairs)
4:5 – 3:3	0.262	0.047	< 0.0001	< 0.0001
4:5 – 4:4	0.221	0.040	< 0.0001	< 0.0001
3:4 – 3:3	0.194	0.050	0.0002	0.0015
2:1 – 3:3	0.170	0.050	0.0009	0.0076
3:4 – 4:4	0.154	0.043	0.0005	0.0048
2:1 – 4:4	0.129	0.043	0.0032	0.0261
4:5 – 2:1	0.092	0.043	0.0325	0.2014
4:5 – 3:4	0.067	0.043	0.1215	0.5270
4:4 – 3:3	0.041	0.047	0.3894	0.9097
3:4 – 2:1	0.025	0.046	0.5913	0.9832

Figure 2.15 shows the distribution of fit parameters for the antibunching data collected from the QEs characterized for this work. While $g^2(0)$ values were process dependent, we did not find any significant variations in average bunching amplitude, lifetime τ_1 , and decoherence time τ_2 across the parameter combinations that produced the highest emitter yields.

ZPL characterization

We report the results of Student's t and Tukey-Kramer HSD Mean average ZPL Comparison Tests for each FIB exposure time averaged over all anneal times in **Table 2.11** and for each carbon annealing time averaged over all FIB exposure times in **Table 2.12**.

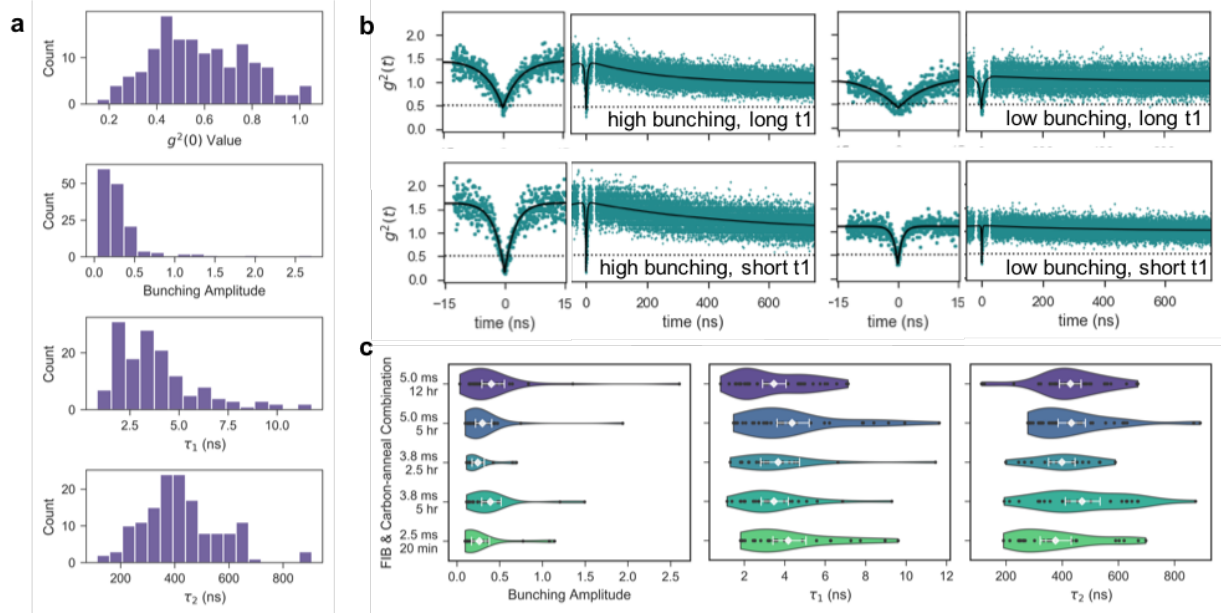


Figure 2.15. Second order photon correlation fit parameter distributions (a) Histograms for the fit parameter values extracted from fitting Equation 2.1 to photon correlation data for each color center characterized for this work where $g^2(0) < 1.0$ (b) Example antibunching curves from $g^2(t)$ with green points showing rebinned data and black lines showing fit (c) Violin plots showing distributions of bunching amplitude, τ_1 , and τ_2 for the five best QE fabrication parameter combinations.

Table 2.11. ZPL by FIB Exposure – Mean Comparison Tests $\alpha = 0.05$ significance level, unbalanced, unequal variance

Exposure 1 – Exposure 2	Difference	Standard Error Difference	p-value (Student's t Each Pair)	p-value (Tukey-Kramer HSD All Pairs)
5.0 ms – 2.5 ms	0.064	0.021	0.0022	0.0063
3.8 ms – 2.5 ms	0.043	0.018	0.0164	0.0430
5.0 ms – 3.8 ms	0.021	0.021	0.3121	0.5690

Table 2.12. ZPL by Carbon anneal time – Mean Comparison Tests $\alpha = 0.05$ significance level, unbalanced, unequal variance

Anneal Time 1 – Anneal Time 2	Difference	Standard Error Difference	p-value (Student's t Each Pair)	p-value (Tukey-Kramer HSD All Pairs)
2.5 hr – 1.25 hr	0.068	0.029	0.0213	0.0964
5 hr – 1.25 hr	0.063	0.022	0.0049	0.0252
2.5 hr – 20 min	0.036	0.028	0.1885	0.5509
20 min – 1.25 hr	0.032	0.024	0.1871	0.5481
5 hr – 20 min	0.031	0.020	0.1172	0.3954
2.5 hr – 5 hr	0.006	0.026	0.8247	0.9961

Figure 2.16 demonstrates examples of spectra that were similar to the ZPL shape but had $g^2(0) > 0.5$. From this data, we conclude that at these pattern sites where we did not find SPE, we fabricated clusters of defects, with multiple excited at once by a single laser excitation spot.

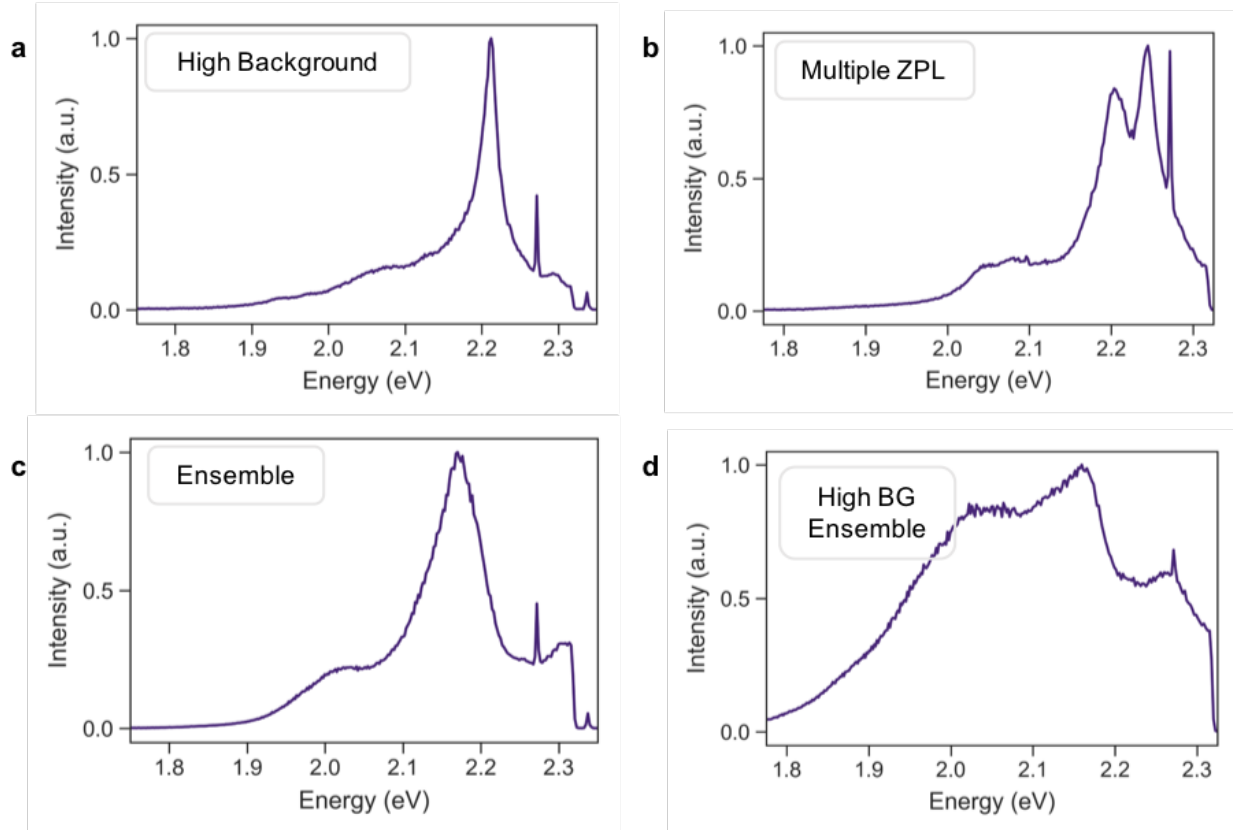


Figure 2.16. Example zero phonon line spectra shapes for $g^2(0) > 0.5$ Many of the color centers characterized for this work exhibited spectral lineshapes similar to ZPL, with a distinct peak and secondary phonon sideband ~ 160 meV, but with either (a) high background, (b) multiple ZPL, or (c)-(d) broad linewidths characteristic of ensemble emission.

2.6. Bridge

In this chapter, I have reported a technique we developed to deterministically and repeatably engineer carbon-based defects in hexagonal boron nitride using a combination of focused ion beam patterning and carbon diffusion. By designing experiments to optimize the yield of single photon emitters and characterize photophysical properties including emission energy and quantum purity, we found that these outputs depended strongly on the combination of FIB

exposure dose and the length of the carbon diffusion step chosen for fabrication. However, we were unable to improve our SPE yields over ~11.5% and our results are inconclusive in identifying a particular defect candidate responsible for this emission. To improve our SPE yields and potentially reduce variations in defect type produced, we need to better control defect creation as well as the material conditions surrounding the desired defects.

FIB patterning is a ballistic process known to cause structural damage to materials at the beam energy we employ. Because the FIB exposure dose had strong independent effects on optical outputs, we therefore set out to investigate how the FIB dose, independent of carbon annealing time, impacts the host material and therefore color center creation. We achieve this via atomic force microscopy (AFM) height topography measurements and Stopping Range of Ions in Matter (SRIM) simulations to quantify damage and correlate FIB damage characteristics to optical outputs. The following chapter details our AFM characterization, observed damage characteristics, FIB exposure simulations, and correlation analysis, as well as proposes a preliminary physical mechanism for how FIB exposure dose influences color center creation that is consistent with the observed morphological damage features and optical characteristics.

CHAPTER III

UNCOVERING THE MORPHOLOGICAL EFFECTS OF HIGH ENERGY GA⁺ FOCUSED ION BEAM MILLING ON HBN SINGLE-PHOTON EMITTER FABRICATION

This chapter contains previously published co-authored material; it has been reproduced with permission from: R. Klaiss, J. Ziegler, D. Miller, K. Zappitelli, K. Watanabe, T. Tanaguchi, B. J. Alemán, “Deterministic Quantum Emitter Formation in Hexagonal Boron Nitride via Controlled Edge Creation.” *J Chem Phys.* 2022, 157 (074703), 1-10. Copyright 2022 American Institute of Physics. In this work, I contributed to designing the research, performing the research, analyzing the data, and writing the paper.

3.1. Introduction

The advancement of quantum information technologies (QITs) such as quantum transducers and sensors require solid-state qubit platforms that host optically addressable single-photon or spin states that couple strongly to external degrees of freedom and can be easily engineered for integration into hybrid systems^{1,4,57,58}. Low dimensional materials are desirable solid-state single photon emitter (SPE) hosts because they exhibit unique electronic, magnetic, and mechanical properties impossible for their bulk counterparts^{32,35,59–62}. Two-dimensional wide bandgap insulator hexagonal boron nitride (hBN) hosts bright and stable room temperature SPEs that couple strongly to applied electric^{32,59} and strain^{31,63} fields, as well as optically detectable magnetic resonance (ODMR) with spin state splitting sensitive to external magnetic

fields^{29,38,64,65}. Furthermore, hBN functions well as both a dielectric substrate for other 2D materials such as graphene^{62,66,67} and transition metal dichalcogenides (TMDCs)^{46,68,69} and as a monolithic platform for photonic circuits⁷⁰⁻⁷², making it a versatile material to integrate into QITs.

Fabrication challenges such as patterning hBN SPEs^{23,43,50,73-77} and direct-writing nanostructures in hBN⁷⁸⁻⁸⁰ have been resolved using focused ion beam (FIB) exposure. However, the high energies required to pattern emitters at precise locations and mill nanostructures cause changes to the morphology of thin hBN crystals that may influence further fabrication steps and impact the material's ability to host SPEs^{46,80}. Moreover, while SPEs found in hBN after FIB exposure have been attributed to either vacancies created deep within the crystal or edges created due to milling, it is not understood how changes to surface morphology that occur due to FIB exposure influence the probability of SPE creation.

To uncover the morphological life-story of hBN crystals to support SPEs while undergoing high energy Ga⁺ FIB exposure, we fabricated samples with a range of exposure doses and characterized changes to the surface roughness, milling depth, swelling, and single photon emission photophysics. Then, we analyzed the correlation between morphological factors and photophysical responses. Furthermore, we performed Stopping Range of Ions in Matter (SRIM) calculations⁸¹ to investigate how vacancy concentration influences morphology and SPE creation. This work provides a necessary framework to elucidate how pristine hBN crystals become damaged in controlled ways at the atomic and nano- scales to perform as needed for quantum technologies.

3.2. Results and discussion

To create samples that contain many visible hBN crystals, we performed an exfoliation transfer of high-pressure high temperature (HPHT) grown hBN crystals onto Si/SiO₂ substrates using heat-release tape and annealed samples at 500°C to clean residual tape from the surface. Once we identified crystals of area $\sim 200 \mu\text{m}^2$ [Figure 3.1(a)] and thickness in the range of 10-17 nm [see

Supplementary information Figure 3.15], we performed Ga⁺ FIB patterning tests. Based on our previous work²³ that created SPEs at precise locations, we patterned arrays of 500 nm diameter circles with beam acceleration

voltage 20 kV and beam current 59 pA. The Ga⁺ FIB used for this work had a minimum exposure time of 1.3 ms for the specified pattern size and current, corresponding to the shortest loop time the FIB can direct-write the circle pattern. We adjusted the ion fluence by changing the exposure time, thereby changing the number of passes performed by the software to pattern the circle and tested 1.3 ms (FIB Level 1: 1 pass), 2.5 ms (FIB Level 2: 2 passes), 3.8 ms (FIB Level 3: 3 passes), and 5.0 ms (FIB Level 4: 4 passes) [Figure 3.1(b)]. We annealed the exposed samples in a home-built chemical vapor deposition (CVD) system used for vertically-aligned carbon nanotube (VACNT) growth with C₂H₄:H₂:Ar flowing gas mixture at 1000°C for 5 hr in

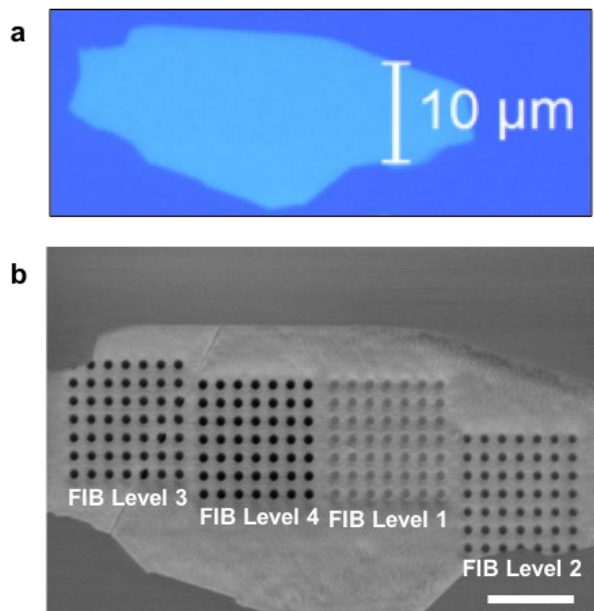


Figure 3.1. Testing FIB exposure on a single hBN flake (a) Optical microscope image of an exfoliated HPHT hBN flake studied in this work prior to FIB exposure. (b) Scanning electron microscope (SEM) image of an hBN flake after patterning arrays of 500 nm circles with Ga⁺ FIB at the four studied exposure times, from left to right, labeled by FIB Level: (3) 3.8 ms FIB Level, (4) 5.0 ms, (1) 1.3 ms, and (2) 2.5 ms. Scale bar: 5 μm

order to create a carbon-rich environment that is expected to activate hBN quantum emitters^{37,40,41}. For more information about the emitter fabrication process, refer to **3.4 Methods**.

After the full emitter fabrication process, we performed tapping-mode atomic force microscopy (AFM) to measure the topography of nanoscale surface features and observed qualitatively different morphological features at each exposure level [**Figure 3.2**].

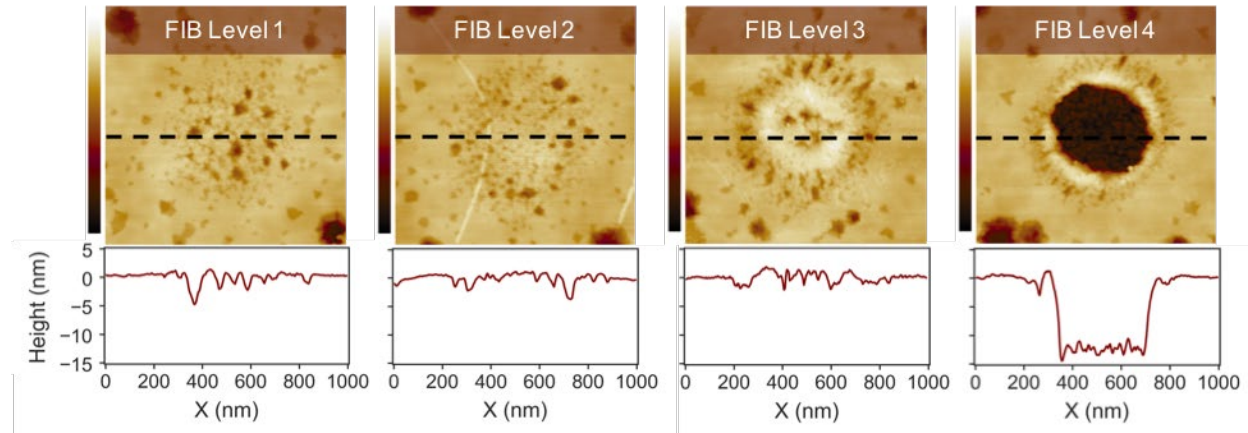


Figure 3.2. AFM characterization of FIB exposure levels AFM height scan images for circles patterned at each of the studied exposure levels marked with black dashed lines where line cuts (below) were taken. AFM height color bar range: [-15 nm, 5 nm]. Line cut: 1 μm

From the AFM height data, we calculated the following morphological characteristics of 1 $\mu\text{m} \times 1 \mu\text{m}$ regions containing one exposed circle each: average mill depth $\overline{\Delta z^-}$, maximum mill depth Δz^-_{max} , mill volume ΔV^- , average swell height $\overline{\Delta z^+}$, maximum swell height Δz^+_{max} , swell volume ΔV^+ , and exposed edge surface area SA [**Figure 3.3**]. Local unexposed surface height z_0 and RMS roughness RMS_0 for each 1 $\mu\text{m} \times 1 \mu\text{m}$ region were calculated from points outside of the exposed pattern area and used as the zero height for calculations and as the threshold for identifying FIB induced damage, respectively. Milling values $\overline{\Delta z^-}$, Δz^-_{max} , and ΔV^- were calculated from data points with height below $z_0 - RMS_0$ and characterized the depth of milled locations and total amount of material removed from the exposed regions. Swelling values $\overline{\Delta z^+}$, Δz^+_{max} , and ΔV^+ were calculated from data points above $z_0 + RMS_0$ and

characterized the height and total amount of FIB induced swelling observed in exposed regions. Exposed edge surface area calculations were performed using all data points in the region, with baseline area of $1 \mu\text{m}^2$ subtracted. For more details about the calculations, refer to **3.4 Methods**.

We report the average values for all calculated morphological characteristics for each exposure level in **Table 3.1** and show the average values of Δz^+_{max} and Δz^-_{max} for each exposure level in **Figure 3.4(a)**, with average values for ΔV^+ and ΔV^- for each exposure in **Figure 3.4(b)**. Plots showing the average values for all calculated morphological characteristics as a function of FIB exposure level can be found in **3.5**

Supplementary information. Based on these calculated values as well as observations made from the data visualized as AFM scan plots in **Figure 3.2**, we found that swelling characteristics and milling characteristics evolve differently with increasing levels of FIB exposure.

Starting at the lowest FIB exposure level (1.3 ms), exposed regions contained small and randomly located areas of milling and swelling within the patterned area with $\overline{\Delta z^-}_1 = -3.26 \pm 0.15 \text{ nm}$ and $\overline{\Delta z^+}_1 = 1.92 \pm 0.09 \text{ nm}$. Regions exposed at the second FIB level (2.5 ms) showed qualitatively similar milling and swelling characteristics and calculated values were similar to the first exposure level, with $\overline{\Delta z^-}_2 = -2.89 \pm 0.11 \text{ nm}$ (**Table 3.1** Student's t-test: $p = 0.1566$) and

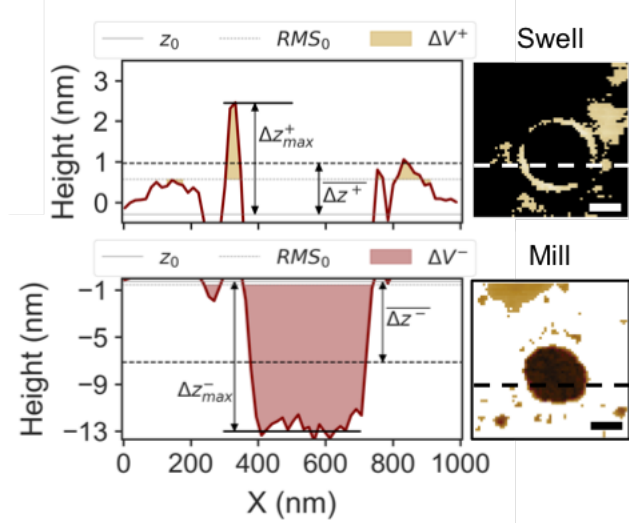


Figure 3.3. Morphological characteristics calculated from AFM height data AFM height profile showing RMS_0 threshold for swell and mill Δz and ΔV calculations from AFM height data with corresponding AFM height image showing points above (**top**) and below (**bottom**) the calculated roughness threshold included in swelling (**top**) and milling (**bottom**) calculations. AFM height image scale bar: 200 nm

Table 3.1. Morphological Characteristics Calculated from AFM mean \pm standard error

FIB Level	$\overline{\Delta z^-}$ (nm)	Δz^-_{max} (nm)	ΔV^- (10^5 nm^3)	$\overline{\Delta z^+}$ (nm)	Δz^+_{max} (nm)	ΔV^+ (10^5 nm^3)	SA (10^3 nm^2)
1	-3.26 ± 0.15	-8.63 ± 0.33	-3.87 ± 0.26	1.92 ± 0.09	2.92 ± 0.18	1.37 ± 0.15	2.03 ± 0.11
2	-2.89 ± 0.11	-7.92 ± 0.22	-3.33 ± 0.22	1.81 ± 0.06	2.57 ± 0.11	1.33 ± 0.14	1.77 ± 0.06
3	-3.25 ± 0.14	-8.19 ± 0.27	-2.53 ± 0.15	2.20 ± 0.08	3.70 ± 0.23	1.89 ± 0.22	1.67 ± 0.07
4	-6.23 ± 0.29	-13.23 ± 0.32	-9.79 ± 0.67	2.12 ± 0.08	3.96 ± 0.25	2.44 ± 0.23	4.12 ± 0.29

$\overline{\Delta z^+}_2 = 1.81 \pm 0.06 \text{ nm}$ (Table 3.1 Student's t-test: $p = 0.3245$). The largest change observed was an 8% decrease in the magnitude of Δz^-_{max} , with $\Delta z^-_{max_1} = -8.63 \pm 0.33 \text{ nm}$ and $\Delta z^-_{max_2} = -7.92 \pm 0.22 \text{ nm}$, but the difference between these values was not strong enough to draw any conclusions about the evolution of morphological characteristics from the first exposure level to the second (Table 3.1 Student's t-test: $p = 0.0837$). Therefore, we determine that there are no significant morphological differences between regions exposed for 1.3 ms and those exposed for 2.5 ms.

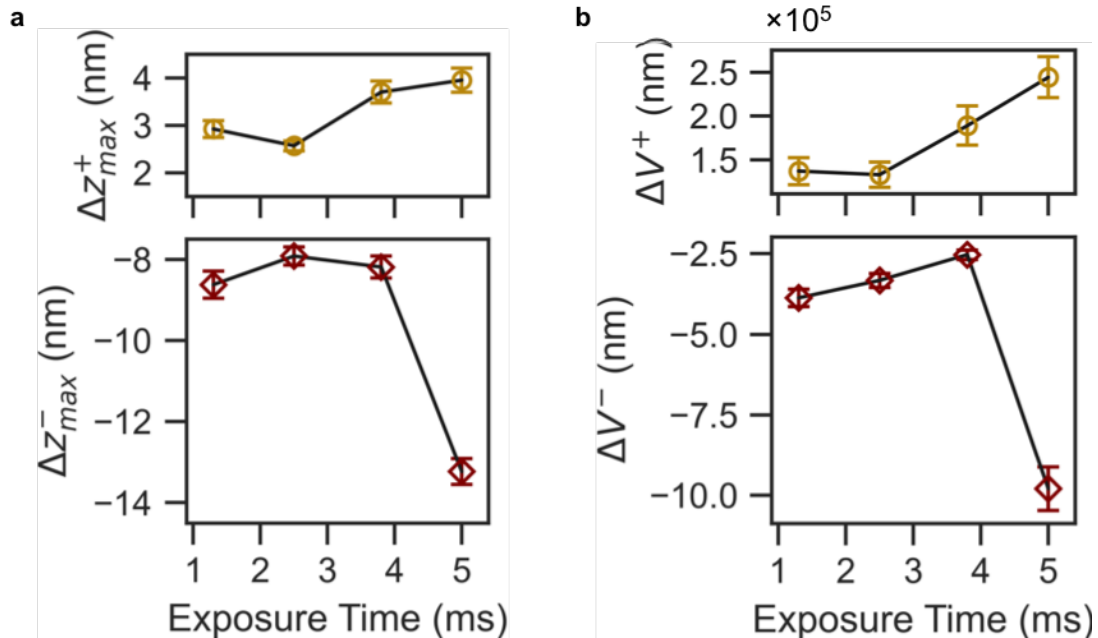


Figure 3.4. Average morphological characteristics for each FIB exposure level (a) Mean calculated values for maximum swell height and maximum mill depth at each FIB exposure level of all samples included in this work. (b) Mean calculated values for swell volume and mill volume at each FIB exposure level of all samples included in this work. The lines connecting data points are a guide to the eye. Error bars on show standard error on the mean.

At the third exposure level (3.8 ms), we began to observe significant changes to morphological characteristics. While regions exposed at the third exposure level were milled similarly to those at the second with $\overline{\Delta z^-}_3 = -3.25 \pm 0.14$ nm (**Table 3.1** Student's t-test $\overline{\Delta z^-}$: $p = 0.1742$), both the average and maximum swell heights increased from the second to the third FIB level (t-test $\overline{\Delta z^+}$: $p = 0.0006$, t-test Δz^+_{max} : $p < 0.0001$), with the mean Δz^+_{max} increasing 44% from $\Delta z^+_{max_2} = 2.57 \pm 0.11$ nm to $\Delta z^+_{max_3} = 3.70 \pm 0.23$ nm.

Regions exposed at the fourth level (5.0 ms) showed swell heights similar to the values calculated at the third (t-test $\overline{\Delta z^+}$: $p = 0.4653$, t-test Δz^+_{max} : $p = 0.3754$). However, ΔV^+ increased 23% from $\Delta V^+_3 = 1.89 \pm 0.22 \times 10^5$ nm³ to $\Delta V^+_4 = 2.44 \pm 0.23 \times 10^5$ nm³ (t-test: $p = 0.0444$). The areas of swelling for regions exposed at the fourth level appeared more localized to the pattern edges, away from the pattern center whereas swelling for regions exposed at the third level was observed within the pattern center. While the swelling was pushed out to the pattern edges, we observed deeper milling more localized to the circle pattern at this level, with the magnitude of Δz^-_{max} increasing 62% from $\Delta z^-_{max_3} = -8.19 \pm 0.27$ nm to $\Delta z^-_{max_4} = -13.23 \pm 0.32$ nm (t-test: $p < 0.0001$). Furthermore, we observed similar behavior in the exposed surface area SA , where $SA_3 = 1.67 \pm 0.07 \times 10^3$ nm² increased 147% to $SA_4 = 4.12 \pm 0.29 \times 10^3$ nm² (t-test: $p < 0.0001$) most likely due to the increase in directional milling forming connected sidewalls at the fourth exposure level. We conclude that swelling is the dominant morphological characteristic starting at the third exposure level and is a precursor to the deeper directed milling that began at the fourth level.

To determine how the targeted morphological characteristics influenced emitter creation, we identified fluorescent locations via confocal microscopy with 532 nm excitation [**Figure 3.5(a)**] and characterized quantum emission via Hanbury Brown and Twiss experiment, fitting $g^2(t)$

data to the three-level system model for antibunching and using the accepted threshold of $g^2(0) < 0.5$ to denote SPE.⁴⁶ To further confirm the quantum nature of emitters, we measured zero-phonon line (ZPL) spectra [see **Figures 2.2(b), 2.16, and Supplementary information Figure 3.17**] within the expected range of 1.8 eV-2.2 eV for room-temperature visible range emission in hBN under 532 nm (2.33 eV) excitation^{15,23,40}. We calculated the average PL of exposed regions at each level by image analysis on confocal PL scan plots segmented into regions of $4 \mu\text{m}^2$, with 1 patterned site per $1 \mu\text{m}^2$. We also calculated the average SPE yield of each segmented $4 \mu\text{m}^2$ region by counting the number of emitters with $g^2(0) < 0.5$ and dividing by 4, the number of patterned sites. For more details on the average PL and SPE yield calculations, refer to **3.4 Methods**.

We observed PL emission from successfully patterned sites exposed at all levels with region PL and SPE yield dependent on exposure level. Patterned sites that bordered or overlapped with an hBN flake edge accounted for $\sim 1\%$ of all patterned sites and exhibited low PL and SPE yield regardless of exposure level. We expect that partially patterned circles created structural environments inconsistent with the fully contained patterned sites intended. Therefore, we considered circle patterns bordering or overlapping with hBN edges to be unsuccessfully fabricated and excluded those sites from our analysis. Of the regions that hosted non-zero SPE yields, we found that patterned sites exposed at the third level hosted SPEs with a yield of 0.047 ± 0.016 (mean comparison test to zero: $p = 0.0027$) and the fourth hosted SPEs with a yield of 0.115 ± 0.025 (mean comparison test to zero: $p < 0.0001$) [**Figure 3.5(c)**]. The regions exposed at the two lowest levels, that did not host SPEs, exhibited brighter regions on confocal scan plots, with $PL_1 = 573 \pm 27$ cts and $PL_2 = 1097 \pm 56$ cts, while the third level exhibited

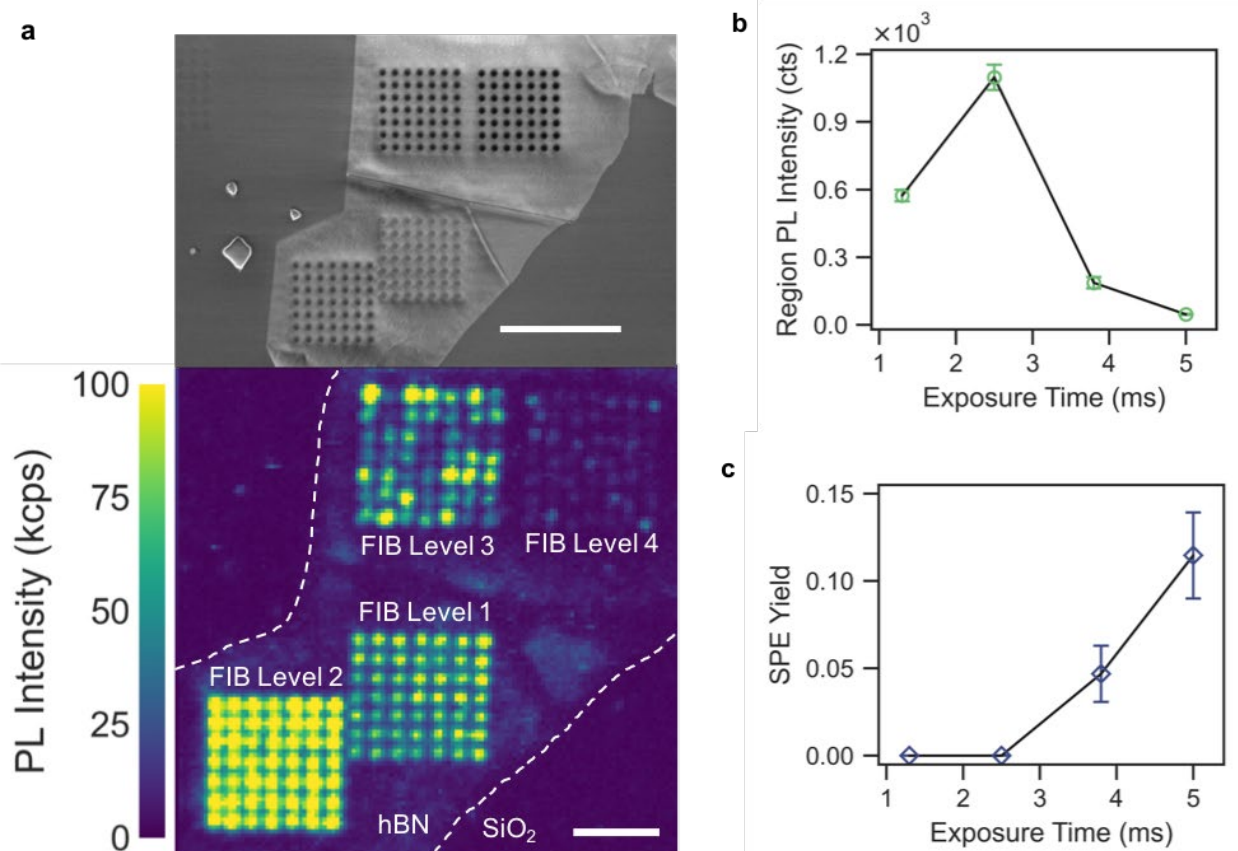


Figure 3.5. Summary of photophysical characterization by FIB exposure (a) Confocal PL map showing all 4 levels of FIB exposure. Dashed line marks the flake edges. Scale bar: $4 \mu\text{m}$. (b) Mean values Region PL intensity as a function of FIB exposure time, showing statistically significant differences between each level when compared via Tukey-Kramer HSD all-pairs comparison test. (c) Mean values SPE Yield (number of SPEs per 4 milled sites) as a function of FIB exposure time, showing statistically significant differences between the highest exposure times and all others when compared via Tukey-Kramer HSD all-pairs comparison test. The lines connecting data points in (c) and (d) are guides to the eye. Error bars in both plots show standard error on the mean.

lower PL on average with $PL_3 = 186 \pm 25$ cts (Tukey test: $p < 0.0001$) and the fourth even lower on average with $PL_4 = 46 \pm 3$ cts (Tukey test: $p < 0.0001$) [**Figure 3.5(b)**].

We conjecture that brighter PL indicates that many optically active vacancy defects remained within the crystal at exposed regions, so excited locations within the diffraction limited spot exhibited ensemble emission rather than single photon emission. We further expect that higher SPE yields were possible when many optically active defects were removed by milling, reducing the overall background PL. This conjecture is consistent with the highest SPE yield, lowest

region PL, and largest milling observed at the highest FIB exposure level. However, it is inconsistent with the non-zero SPE yield, lower region PL, and lower milling observed at the third exposure level. Therefore, the morphological characteristic of deep and directed milling cannot be fully responsible for the optical characteristics of FIB exposed hBN crystals.

When comparing all calculated morphological characteristics to the measured optical characteristics [Figure 3.6(a)], we found that the PL intensity at each FIB exposure level was strongly correlated only to the maximum swell height at each FIB level, with $c(PL, \Delta z^+_{max}) = -0.969$ ($p = 0.0309$), while the SPE yield at each FIB level was strongly correlated only to the average volume of swell areas at each FIB level with $c(SPE, \Delta V^+) = 0.9955$ ($p = 0.0045$) [Figure 3.6(b)]. Furthermore, the observed increases in material swell height and volume were the only morphological features that correlated even weakly ($0.05 < p < 0.20$) to increased SPE

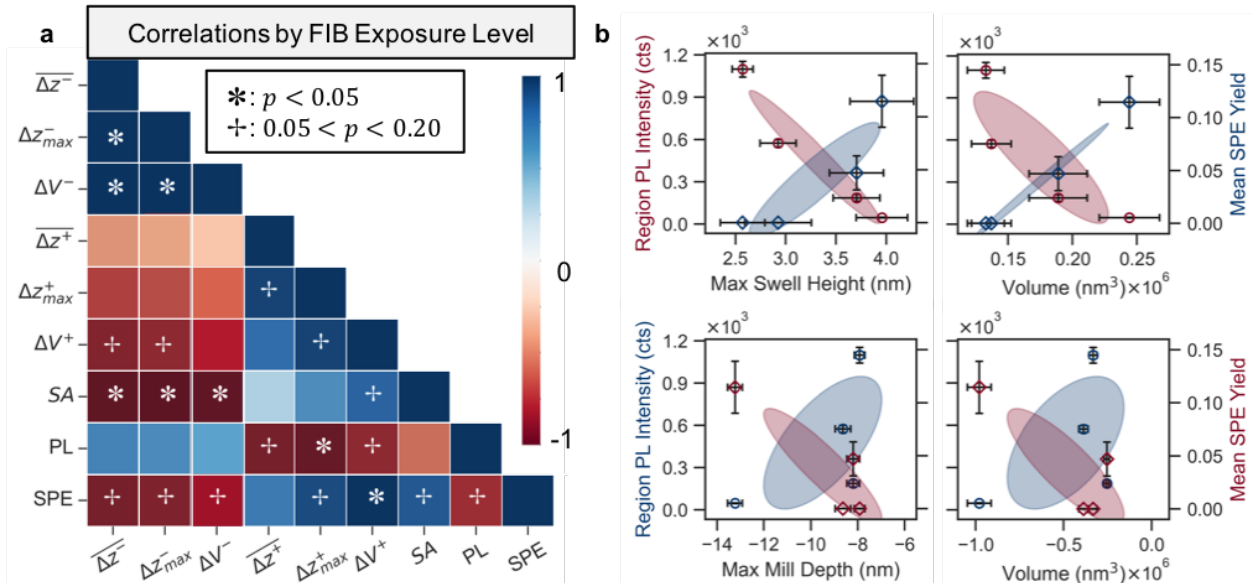


Figure 3.6. Correlating material damage to SPE yield and photoluminescence (a) Correlation matrix for calculated morphological characteristics and measured optical characteristics, with p-value denoting the significance of the correlation strength (b) Plots showing the correlation by 1σ density ellipse between the morphological characteristics and optical characteristics. Each data point represents the mean calculated value of the specified optical characteristic at a given exposure level plotting at the corresponding mean calculated value of the specified morphological characteristic at the same exposure level. Error bars show standard error on the mean for the calculated values at each exposure level along the specified axis.

yield and diminished PL simultaneously. We expect that the morphological characteristic of swell is indicative of damage levels within the crystal that decrease PL and increase the likelihood of hosting SPEs prior to deep and directed milling.

To elucidate possible shared causes for both the observed swelling due to FIB damage and the observed optical characteristics on the atomic level, we performed SRIM calculations for vacancy concentrations. We performed the Monolayer Collision Steps/Surface Sputtering calculation, which was considered optimal for the thickness range of flakes studied in this work⁸¹. From the SRIM calculations, we acquired the vacancy number per ion as a function of depth and lateral position $N_{v/Ga^+}(x, z)$ for a 20 keV Ga⁺ beam entering the material at a single point, where SRIM assumes a beam diameter of 0.

To determine the ion exposure profile $D_{Ga^+}(x, y)$ for the full 500 nm circular pattern, we modeled the beam as a 2D gaussian⁸² and summed over all points in the pattern following a circular beam path, with the beam pitch set constant as in the patterning software for all patterning experiments [Figure 3.7].

We simulated the vacancy concentration $n_v(x, z)$ in exposed regions by convolving $N_{v/Ga^+}(x, z)$ at a given point with the simulated exposure profile $D_{Ga^+}(x)$ at that point over a 1 μm position range. Lastly, to mimic the material conditions upon which optical data was collected, we further convolved $n_v(x, z)$ with the height data

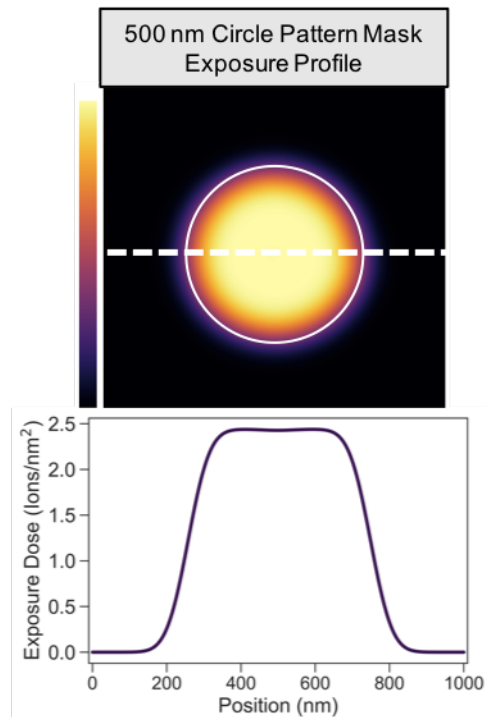


Figure 3.7. Simulated FIB exposure dose profile calculated using a 2D Gaussian beam [Equation 3.15] scanned in a circular trajectory for a 500 nm circle pattern as set in the FIB patterning software with corresponding profile showing ions/nm² as a function of position

collected by AFM at each point, removing areas of the simulated material at locations where the experimental material was milled a depth $-\Delta z$. For more information about simulation parameters and how we accounted for milling at each increased FIB exposure level, refer to **3.4 Methods**.

Based on the results of these simulations, shown in **Figure 3.8**, we observed that the $n_v(x, z)$ increased steadily with each increase in FIB exposure level. Furthermore, while the significant increase in milling at the fourth exposure level removed a large volume of regions with high vacancy concentrations, many regions with high n_v remained due to Δz^-_{max} less than the starting thickness of material h_0 . This is consistent with our hypothesis that although milling away high n_v areas contributed to an overall lower number of optically active defects at the

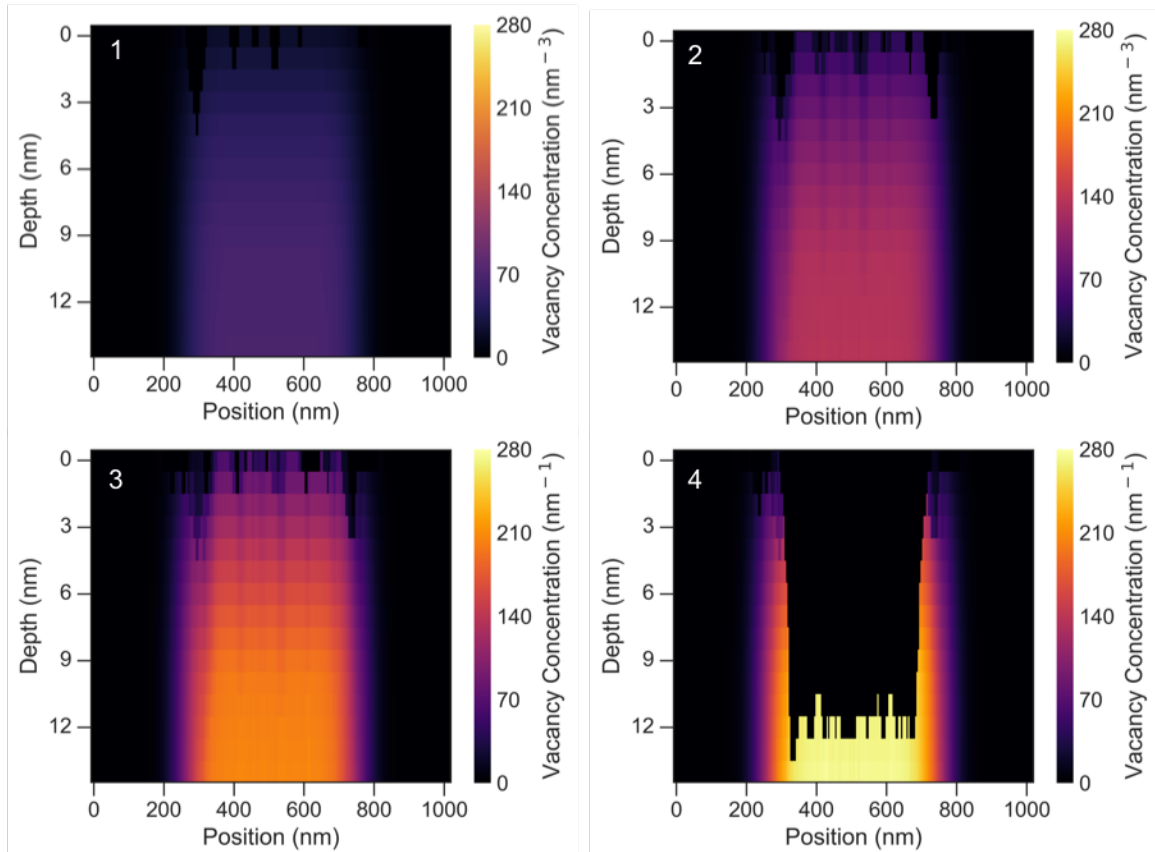


Figure 3.8. SRIM vacancy concentration profile $n_v(x, z)$ for FIB exposure level 1 (top left), 2 (top right), 3 (bottom left) and 4 (bottom right) with milled regions removed according to representative AFM line cuts

fourth level, the onset of milling distinct circular holes alone cannot fully justify the PL decrease and onset of isolated SPEs we observed. Furthermore, since the level of swelling correlated strongly to these observed optical characteristics, we expect that there exists some threshold vacancy concentration n_v^{swell} that leads to the observed increase in swelling and therefore the observed changes to optical characteristics. In addition, by combining n_v^{swell} with a corresponding threshold vacancy concentration n_v^{mill} that leads to the observed onset of directed and localized milling, we expect that we can determine different regimes of material damage and qualitatively describe how they influence the material's ability to support SPEs at patterned locations.

To find the value for n_v^{mill} from our simulated data, we first calculated the onset exposure time t_{0-} by fitting the normalized remaining thickness $1 - |\overline{\Delta z^-}(t)|/h_0$ to a complementary error function with constant offset, finding the intersection t_{0-} of the maximum amplitude with the negative slope linear regime, and calculated $n_v(t_{0-})$ from a linear fit of $n_{v\ max}(t)$. This

process is illustrated in **Figure 3.9**, which shows the normalized remaining thickness fit plotted with $n_{v\ max}(t)$. We similarly found n_v^{swell} by fitting $\overline{\Delta z^+}(t)$ to an error function with constant offset, finding the intersection t_{0+} of the minimum amplitude with the positive slope linear regime, and calculated $n_v(t_{0+})$ from the linear fit $n_{v\ max}(t)$. From these calculations, we found $n_v^{swell} \sim 150\ \text{nm}^{-3}$ and $n_v^{mill} \sim 243\ \text{nm}^{-3}$. Furthermore, we

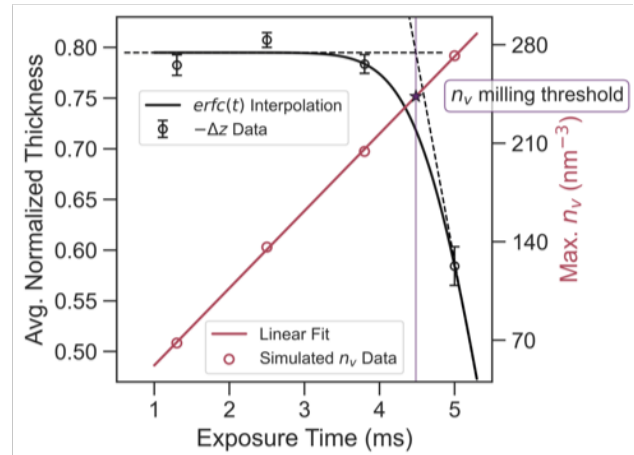


Figure 3.9. Estimating damage thresholds from simulated vacancies Average remaining thickness calculated from average mill depth at each exposure level used to find t_{0-} , denoted by the vertical line between 4.0 ms and 5.0 ms, and calculate n_v^{mill} , marked by the star at $n_{v\ max}(t_{0-})$. Error bars on thickness points are standard error on the mean.

similarly fit Δz^+_{max} to calculate a simulated concentration that corresponded to the maximum observed swelling and obtained $n_v^{max. swell} \sim 186 \text{ nm}^{-3}$.

Using these threshold values, we simulated the change in thickness profile as a function of position $\Delta z(x)$ for the third and fourth FIB exposure levels by plotting the maximum vacancy concentration as a function of position $n_{v max}(x)$ with positive increasing values if the swell threshold was crossed and before the maximum swell, positive decreasing values if the swell threshold was crossed and after the maximum swell, and with negative values if the mill threshold was crossed, as shown in **Figure 3.10**. For more details about the simulated thickness profile calculations and fits, refer to **3.4 Methods**.

We observed that the simulated height profile was highest towards the center of the exposed region for the third exposure level, whereas the simulated height profile for the fourth exposure level was highest towards the edges, corresponding to the locations where swelling was observed, in good qualitative agreement with our AFM height data [**Figure 3.10**], as well as results from Glushkov et. al.⁷³ that show swelling around the edges of circles patterned with high-energy Xe+ FIB. Additionally, results from Glushkov et. al. show that emission is localized to the edges of these patterned circles with swelling, thereby demonstrating that optically active vacancy defects that exhibit photophysical properties of SPEs remain in regions where swelling is observed. Because we only observed swelling in exposed regions with $n_v^{swell} < n_v < n_v^{mill}$, we expect that vacancy concentrations within this range correspond to a distinct type of crystallographic defect, causing higher swelling, reduced region PL, and the onset of non-zero SPE yield.

Supported by the morphological characteristics calculated from AFM height data, the optical characteristics calculated from confocal PL and antibunching data, and the vacancy

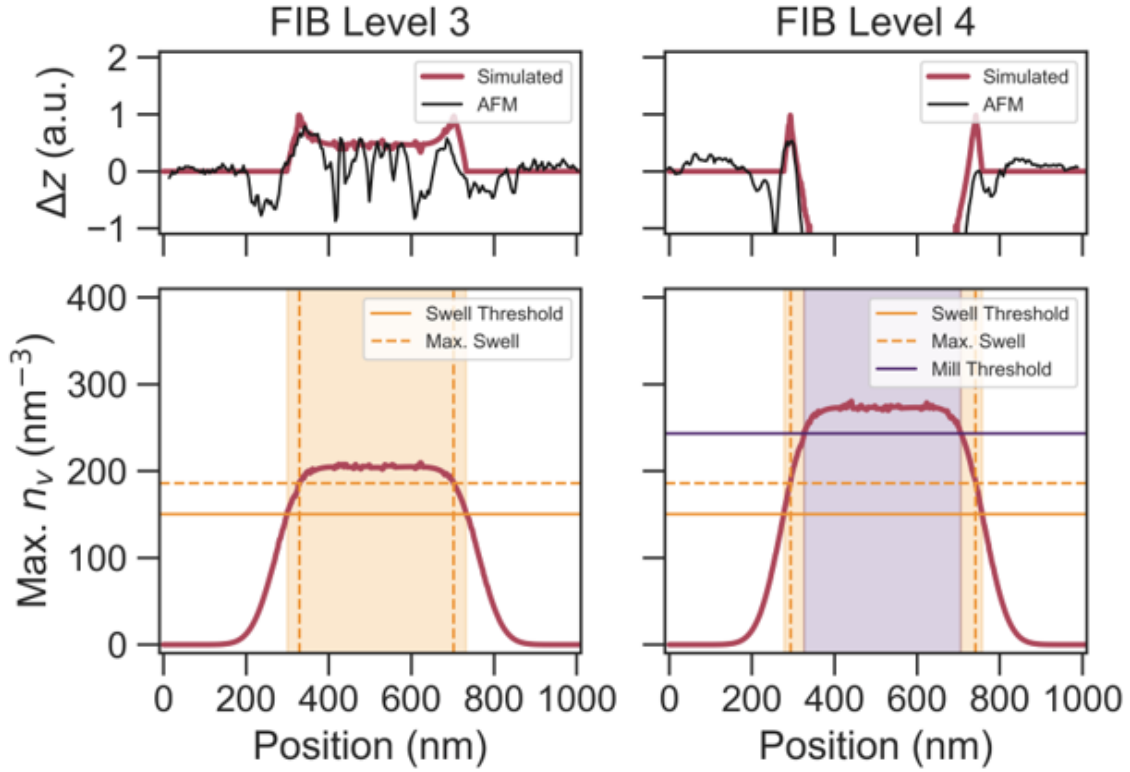


Figure 3.10. Simulated swelling and milling via vacancy concentration thresholds Simulated change in height profile $\Delta z(x)$ calculated from normalizing $n_{v\ max}(x)$ according to n_v^{swell} , $n_v^{max.\ swell}$, and n_v^{mill} , with positions where these thresholds are met denoted on $n_{v\ max}(x)$. AFM height profile as plotted in Fig. 1(b) for the corresponding exposure level is reproduced here to show qualitative agreement with the simulated height profile.

concentration characteristics calculated from SRIM and ion exposure simulations, we expect that at some critical vacancy concentration $n_v^{swell} < n_v < n_v^{mill}$ present after FIB exposure at the third and fourth levels studied in this work, vacancies coalesce into larger volumetric crystal defects, or voids, indicated by the swelling level^{56,73,81}, that are not optically active at an excitation wavelength of 532 nm [Figure 3.11]. The process of void nucleation and growth in irradiated materials is well studied for materials similar to hBN^{83,84} and is consistent with recent investigations into nanopore growth in irradiated monolayer hBN^{85–87}. Furthermore, the atomic density n/V_c of multilayer hBN with lattice constants $a = 2.5 \text{ \AA}$ and $c = 6.6 \text{ \AA}$ ⁸⁸ with AA' stacking⁵⁵ is approximately 166 nm^{-3} , which lies within the simulated range for n_v where

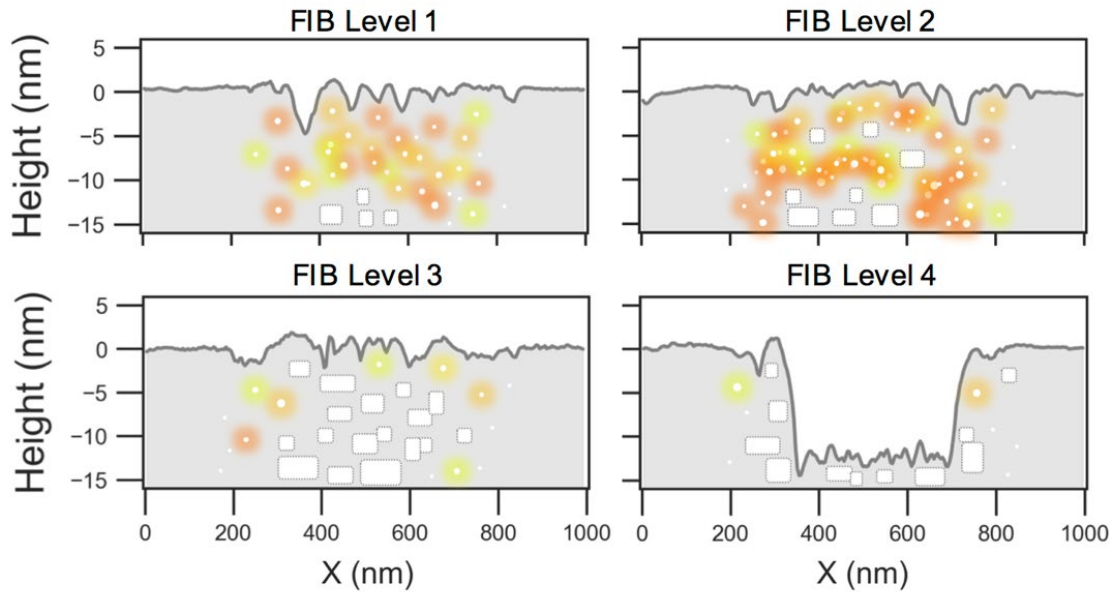


Figure 3.11. Illustration of vacancy distribution, void nucleation and growth, and milling, demonstrating the observed PL and SPE yield for each FIB exposure level as dependent on the distribution of optically active vacancies and non-optically active voids. Gray areas illustrate hBN, white circles with glowing edges illustrate vacancy defects that are color centers, and white rectangles illustrate voids

swelling is observed. This is consistent with our expectation that voids form when vacancies dominate the underlying crystal structure, which can be described as $n_v > n/V_c$.

While local layer mixing⁵⁶, Ga⁺ and recoil ion implantation⁸¹, and carbon impurity doping from the emitter activation process may contribute in small parts to the observed swelling, they cannot fully describe the sudden transition in optical characteristics observed between the second and third FIB exposure levels without considering a critical n_v that causes void nucleation. Because voids act as sinks for vacancies⁸⁹, the presence of voids in higher quantities starting at the third exposure level further supports the observed decrease in region PL and better isolation of SPEs at patterned sites despite similar milling to the first and second exposure levels. Smaller, optically active vacancy defects would no longer be evenly distributed within the crystal causing background fluorescence during emitter excitation and would instead be concentrated at the void locations, coalesced as part of the large volumetric defects that would have different optical

characteristics, and would not change the overall vacancy number, remaining consistent with our vacancy concentration calculations.

Considering the results, calculations, and analysis presented in this work, we propose the following model for the fabrication of isolated SPEs via high-energy Ga⁺ FIB milling of pristine hBN crystals:

With no FIB exposure, pristine hBN hosts no SPEs. Un-exposed and carbon-annealed hBN hosts randomly located SPEs with a density of 0.0125/μm² (mean comparison test to zero: p = 0.0416) likely due to low concentrations of native vacancy defects forming complexes with carbon impurities^{41,90}.

At the lowest FIB exposure level (1.3 ms), exposed areas host many optically active vacancy defects [**Figure 3.5(a)-(b), Figure 3.8**] with visible-range emission under 532 nm excitation, and we do not observe isolated SPEs and ZPLs with traditional diffraction limited confocal techniques. This is characterized by the high region PL [**Figure 3.5(b)**] and zero SPE yield [**Figure 3.5(c)**]. Some surface level milling and sputtering occurs and few areas with particularly high vacancy concentrations contain voids. This is characterized by randomly located pockets of milling and nonzero swelling within the exposed area [**Figure 3.2**].

At the next FIB exposure level (2.5 ms), exposed areas host more optically active vacancy defects [**Figure 3.5(a)-(b), Figure 3.8**], and we again did not isolate SPEs with traditional confocal techniques. This is characterized by the similar inconsistent sputtering of the exposed surface compared to the first level (t-test: p = 0.1566) [**Figure 3.2, Figure 3.4**], the 90% increase in region PL (t-test: p < 0.0001) [**Figure 3.5(b)**], and zero SPE yield [**Figure 3.5(c)**]. Areas with particularly high vacancy concentrations host voids. This is characterized by small areas of

randomly located nonzero swelling similar to the first level (t-test: $p = 0.3245$) [**Figure 3.2, Figure 3.4**].

At the third FIB exposure level (3.8 ms), exposed areas have even higher concentrations of vacancies [**Figure 3.8**]. Many more regions have reached a critical concentration of vacancies, and therefore contain more voids than optically active vacancies or complexes, but voids have not coalesced into structural defects that cause significant material breakage and directed milling. This is characterized by surface level milling and sputtering similar to the previous level (t-test: $p = 0.5058$) [**Figure 3.2, Figure 3.4**], the 44% increase in surface swelling height (t-test: $p < 0.0001$) [**Figure 3.4**] localized towards the center of the exposed area [**Figure 3.2, Figure 3.10**], the 83% decrease in region PL (t-test: $p < 0.0001$) [**Figure 3.5(a)-(b)**], and the onset of non-zero SPE yield (mean comparison test to zero: $p = 0.0027$) [**Figure 3.5(c)**].

At the fourth and highest FIB exposure level tested (5.0 ms), exposed areas have the highest concentrations of vacancies, but as voids continue to grow, complete breakage and therefore milling of the material occurs, leaving behind voids and vacancies along the edges of the milled pattern [**Figure 3.8, Figure 3.10**]. This is characterized by the 62% increase in mill depth (t-test: $p < 0.0001$) [**Figure 3.2, Figure 3.4(a)**], the 147% increase in exposed edge surface area (t-test: $p < 0.0001$) [see **Supplementary information Figure 3.11**], the 287% increase in milled volume (t-test: $p < 0.0001$) [**Figure 3.2, Figure 3.4(b)**], and the similar level of surface swelling height (t-test: $p = 0.8108$) but 23% increase in swelling volume (t-test: $p = 0.0444$) [**Figure 3.2, Figure 3.4**]. Furthermore, voids act as sinks for many remaining vacancies causing the growth of voids and decrease in isolated vacancies in nearby regions, further driven by diffusion during the high temperature annealing used to activate emitters. Therefore, the number of optically active defects causing background continues to decrease. This is characterized by the

75% decrease in region PL (t-test: $p = 0.0174$) [Figure 3.5(a)-(b)] and the 147% increase in SPE yield (t-test: $p = 0.0073$) from the third level [Figure 3.5(c)].

The spatial distribution and relative concentrations of vacancies, complexes, and voids could be confirmed by high resolution electron microscopy characterization techniques such as transmission electron microscopy (TEM) or scanning transmission electron microscopy (STEM) performed on cross-sections sliced from hBN crystals deterministically patterned with high-energy Ga⁺ FIB. Studies that explore the large range of Ga⁺ ion energies and fluences with fine control could quantitatively measure damage thresholds that correlate to the observed morphological characteristics. Furthermore, combining these characterization techniques with computational studies such as Molecular Dynamics (MD) and Density Functional Theory could elucidate void nucleation and growth dynamics while also considering stable quantum emitter defect candidates that include carbon incorporated during the annealing process and allow for the creation of SPEs fabricated with this technique.

3.3. Conclusions

In this work, we demonstrated that morphological characteristics due to FIB exposure play an important role in the deterministic placement of SPEs by patterning SPEs in hBN with four levels of FIB exposure and characterizing surface topography via AFM. From our analysis, we found that the evolution of swelling most strongly correlates to the number of SPEs we observed and anticorrelates to PL intensity. We expect that swelling indicates volumetric voids and local amorphization of hBN layers, with these conclusions supported by SRIM calculations and literature that employ MD modeling^{25,56,89}. Therefore, we conjecture that while fluorescent vacancy defects are present at all FIB doses, the increased damage indicated by the swelling onset at the third exposure level and the milling onset at the fourth actually decreases the total

number of optically active defects at a given milled site, allowing for the localization of single emitters.

Further experimental and computational studies are necessary to identify the ideal damage threshold to localize emitters in hBN without high-cost and high-precision individual defect placement techniques. For suspended structures such as photonic waveguides and optomechanical transducers, it may be desirable to identify an ion species that can produce a higher yield of localized emitters with minimal sputtering, demonstrated at our third FIB level.^{70-72,91,92} Another possible route could be to optimize the milled edge profile for SPE creation and design photonic devices that rely on the creation of these edges. By identifying the morphological characteristics that can be leveraged to engineer hBN SPEs for quantum technologies, we have provided insight into the evolution of these defects-by-design that can be applied to the expanding field of solid-state single-photon emitter sources.

3.4. Methods

Sample Preparation

HPHT hBN Exfoliation: We prepared the samples studied in this work on Si/SiO₂ substrates with 300 nm of thermal wet oxide in order to optically observe hBN thin films. Substrates were patterned with a number array via laser writing and reactive ion etching for labeling purposes only. After the labeling process, chips were cleaned in acetone sonication bath for 5 min and IPA sonication bath for 5 min. Cleaned chips were exposed to 300 mTorr O₂ plasma at 300 W RF power in a March plasma cleaner for 1 min to create a hydrophilic surface for material transfer adhesion. HPHT hBN crystals were prepared for exfoliation transfer on thermal release tape. The thermal release tape with hBN crystals was placed on the substrate surface immediately after oxygen plasma exposure. The substrate-hBN-tape stack was placed on a hot plate 120°C for 5

minutes to release the tape from the substrate-hBN stack. The sample was cleaned of any tape residue in a quartz tube furnace open to air at 500°C for 3 hours with no gas flow.

FIB Patterning: FIB exposure was performed in a FEI Helios Dual Beam with Ga⁺ source. Prior to sample loading, the chamber was plasma cleaned with air for 5 min. The FIB was set to acceleration voltage 20 kV and beam current 59 pA for all experiments according to main text reference ²³. The 500 nm diameter circular pattern exposure mask was drawn directly in the Ion Beam quadrant of the instrument user interface with the following pattern parameters: Overlap X = 50%, Overlap Y = 50%, Pitch X = 12.64 nm, Pitch Y = 12.64 nm, Loop Time = 1.3 ms, Scan Type = Circular, Fill Style = Solid, Total Diameter = 25.3 nm. Once the pattern was drawn in the quadrant, we created an array of 500 nm circles with 1 μm pitch. To vary the ion fluence, the exposure time was set in pattern execution tool to 1.3 ms, 2.5 ms, 3.8 ms, or 5.0 ms depending on the experiment, thereby increasing the number of passes where 1.3 ms = 1 pass, 2.5 ms = 2 passes, 3.8 ms = 3 passes, and 5.0 ms = 4 passes. The order of exposure times varied for each hBN flake patterned.

SPE Activation: Carbon-rich annealing was performed according to **2.4 Methods**.

AFM Characterization and Calculations: AFM height data was collected with a Bruker Dimension FastScan AFM in Tapping Mode. AFM scans were collected with a 1:1 aspect ratio with 256 points per line and 256 lines per scan. Scans was post-processed with NanoScope Analysis Flatten and Plane Fit tools.

Morphological characteristics were calculated from AFM height data collected during 16 μm² AFM scans on each hBN flake at each exposure level, for a total of 16 AFM scan images. Scans were segmented into $A_R = 1 \mu\text{m}^2$ area regions, so each region would contain one exposed 500 nm circle per region. Segmented regions contained $N_x = 64$ points per line and $N_y = 64$

lines per scan for a total of $N = 4096$ height data points [Figure 3.12(a)]. Exposed circles were roughly in the center of each region, so data points in the outer perimeter could be taken as unexposed [Figure 3.12(b)]. To determine the unexposed zero height z_0 for calculations in each region, height values z_i in the region perimeter were averaged together by

$$z_0 = \frac{\sum_i^{N_0} z_i}{N_0} \quad (3.1)$$

where N_0 is the number of data points in the designated unmilled perimeter. The average unmilled roughness of each region was calculated from the same data points relative to the zero height:

$$RMS_0 = \frac{\sum_i^{N_0} (z_i - z_0)^2}{N_0 - 1} \quad (3.2)$$

All height data points in the region were shifted by z_0 [Figure 3.12(c)] and used to calculate the morphological characteristics below, where $z_{<RMS_0}$ denotes height values less than $-RMS_0$, $z_{>RMS_0}$ denotes height values greater than RMS_0 , $N_{z_{<RMS_0}}$ is the number of data points with height values less than $-RMS_0$, $N_{z_{>RMS_0}}$ is the number of data points with height values greater than RMS_0 , $\Delta x = \frac{1 \mu\text{m}}{N_x}$ is the distance between points in a line, and $\Delta y = \frac{1 \mu\text{m}}{N_y}$ is the distance between lines in a scan.

Average mill depth:

$$\overline{\Delta z_-} = \frac{\sum_{i,j}^{N_x, N_y} z_{<RMS_0}(x_i, y_j)}{N_{z_{<RMS_0}}} \quad (3.3)$$

Maximum mill depth:

$$\Delta z_{-max} = \frac{\sum_0^{10} (z_{<RMS_0})_{max}}{10} \quad (3.4)$$

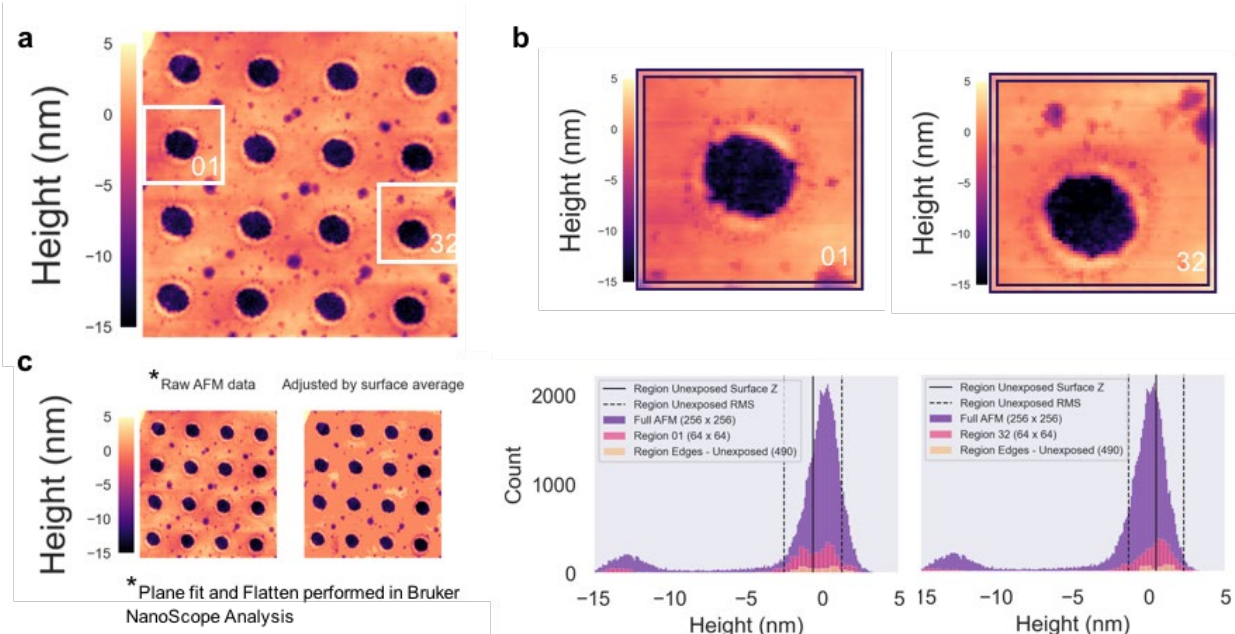


Figure 3.12. Analyzing AFM height data to calculate morphological characteristics, (a) AFM height scan image (size $4 \mu\text{m} \times 4 \mu\text{m}$) of 500 nm circles patterned at the highest FIB dose showing holes milled in the hBN surface. White boxes show examples of $1 \mu\text{m}$ by $1 \mu\text{m}$ segmented regions, labeled by column and row: 01 and 32 (b) AFM height scan images of segmented regions 01 (left) and 32 (right) with border edges boxed in purple outline used to calculate average unmilled height and unmilled roughness for thresholding (c) Comparison of original AFM height scan image (processed with Plane Fit and Flatten functions in NanoScope Analysis) with the same AFM height scan image after thresholding. Histograms show the distribution of height data points for the full $4 \mu\text{m} \times 4 \mu\text{m}$ scan (purple), the segmented $1 \mu\text{m} \times 1 \mu\text{m}$ regions (pink), and edges used in threshold calculation (tan). Solid black line shows average surface height and dotted black lines show the threshold for average unexposed roughness.

Average swell height:

$$\overline{\Delta z_+} = \frac{\sum_{i,j}^{N_x, N_y} z_{>RMS_0}(x_i, y_j)}{N_{z>RMS_0}} \quad (3.5)$$

Maximum swell height:

$$\Delta z_{+max} = \frac{\sum_0^{10} (z_{>RMS_0})_{max}}{10} \quad (3.6)$$

Exposed edge surface area:

$$SA = \left[\frac{1}{4} \sum_{i,j}^{N_x-1, N_y-1} \frac{\sqrt{(a1 + b1 + c) * (-a1 + b1 + c) * (a1 - b1 + c) * (a1 + b1 - c)} + \sqrt{(a2 + b2 + c) * (-a2 + b2 + c) * (a2 - b2 + c) * (a2 + b2 - c)}}{-A_R} \right] \quad (3.7)$$

where

$$a1 = \sqrt{(z_{i,j} - z_{i+1,j})^2 + \Delta x^2} \quad (3.8)$$

$$b1 = \sqrt{(z_{i+1,j} - z_{i+1,j+1})^2 + \Delta y^2} \quad (3.9)$$

$$c = \sqrt{(z_{i,j} - z_{i+1,j+1})^2 + \Delta x^2 + \Delta y^2} \quad (3.10)$$

$$a2 = \sqrt{(z_{i,j} - z_{i,j+1})^2 + \Delta y^2} \quad (3.11)$$

$$b2 = \sqrt{(z_{i,j+1} - z_{i+1,j+1})^2 + \Delta x^2} \quad (3.12)$$

Mill volume:

$$\Delta V_+ = \sum_{i,j}^{N_x, N_y} z_{<RMS_0}(x_i, y_j) * \Delta x * \Delta y \quad (3.13)$$

Swell volume:

$$\Delta V_- = \sum_{i,j}^{N_x, N_y} z_{>RMS_0}(x_i, y_j) * \Delta x * \Delta y \quad (3.14)$$

Optical Characterization: Confocal PL and time correlated photon counting were performed according to **2.4 Methods**.

Statistical Analysis: All statistical tests were performed in JMP analysis software. For analysis of number of SPEs (QEs) and sample PL, samples were divided into $4 \mu\text{m}^2$ regions, which corresponds to 4 FIB patterned locations for patterned samples because we patterned exactly one circle per $1 \mu\text{m}^2$. To calculate the mean PL map intensity, we converted all confocal

image points from kcps to cts by the APD detection bin size of 0.1 s and plotted in grayscale where 0 corresponded to the minimum counts value and 255 corresponded to the maximum counts value for the given PL map. We recorded the mean pixel height in ImageJ for each region, converted it to the mean PL intensity in counts, and averaged all regions processed with a given combination of experimental input factors. To calculate mean SPE yield, we recorded the number of emission sites with $g^2(0) < 0.5$ in each $4 \mu\text{m}^2$ region and averaged all regions processed with a given combination of experimental input factors. We performed mean hypothesis tests, pairwise t-tests, and all pairs Tukey-Kramer HSD tests with $\alpha = 0.05$ significance level to compare SPE yield and region PL intensity across FIB exposure levels. Morphological and optical characteristic correlation was performed in JMP for the average value of each property at each FIB exposure level with an $\alpha = 0.05$ significance level.

Vacancy Concentration Simulation: Vacancy profiles were simulated using Stopping Range of Ions in Matter (SRIM-2013) Monte-Carlo program with 20 keV Ga⁺ ion source up to 2000 ions. The target was set as an hBN-SiO₂ stack to mimic experimental conditions [Figure 3.13].

hBN target layer thickness was varied for each run within the range from 1 nm to 15 nm in 1 nm increments for a total of 15 simulation runs. Damage calculation was set to Monolayer Collision Steps/Surface Sputtering according to recommendations for targets of low thickness found in the SRIM documentation. hBN layer density was set to 2.1 g/cm³. The hBN displacement energies were set according to ⁹³. SiO₂ target layer thickness was varied with the hBN thickness to maintain a constant 100 nm total target thickness for the hBN-SiO₂ stack. We obtained a set of single-point vacancy distribution profiles for each of the specified hBN layer thicknesses $h = \{1, 2, \dots, 15\}$ as a function of position and depth $N_{v/Ga^+}^h(x, z)$ in units of

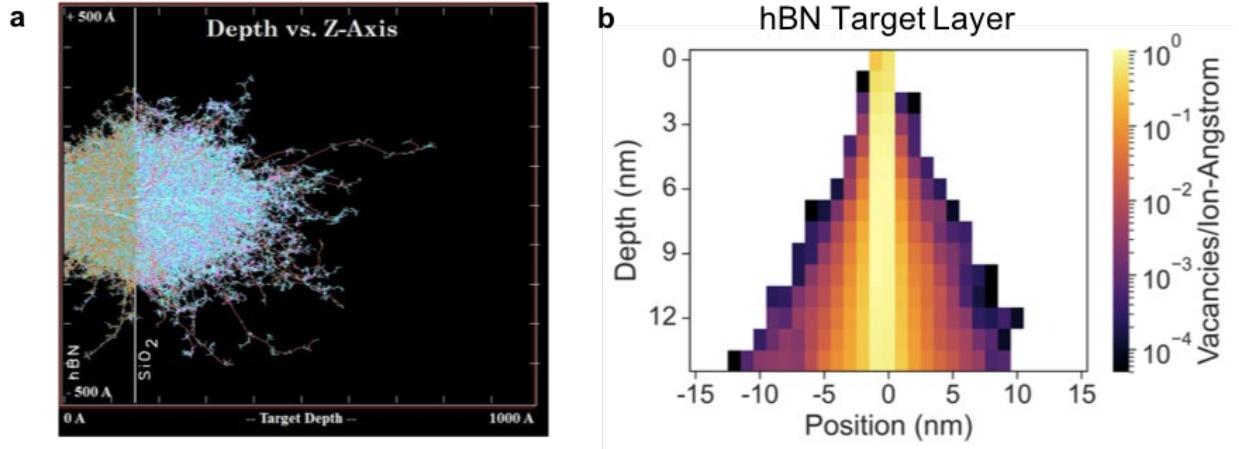


Figure 3.13. Stopping Range of Ions in Matter vacancy concentration (a) SRIM-2013 plot of depth showing monolayer collisions calculation for 20 keV Ga⁺ ions in a 15 nm hBN- 85 nm SiO₂ target layer stack (b) Vacancy concentration profile in hBN target layer as a function of cross-section position and depth

vacancies/ion-Angstrom and were therefore independent of ion dose. SRIM assumes a beam diameter of 0 nm.

We modeled the exposure profile of the full pattern $D(x, y)$ in units of ions/nm² as the superposition of the 2D gaussian beam function of all positions (x_i, y_i) :

$$D_{Ga^+}(x, y) = \sum_{i=1}^P \frac{It_{dwell}}{+e} \frac{1}{2\pi\sigma^2} \exp(-[(x - x_i)^2 + (y - y_i)^2 / 2\sigma^2]) \quad (3.15)$$

where I is the beam current, t_{dwell} is the dwell time at each point, $+e$ is the elementary charge of the Ga⁺ ion, and σ is spread of the gaussian beam. We employed the “apparent beam” model to define σ as the dose distribution with spot size equal to 108 nm according to⁸² due to scattering effects, and not the ideal beam diameter referred to in the FIB Patterning subsection of Methods.

To obtain the ion exposure profile of the full circle pattern, we summed the above 2D gaussian over the circle pattern of diameter d equal to 500 nm, updating x_i and y_i for each subsequent pixel along the circular pattern trajectory with pitch step s as referenced in the **Sample**

Preparation subsection above [Figure 3.14]:

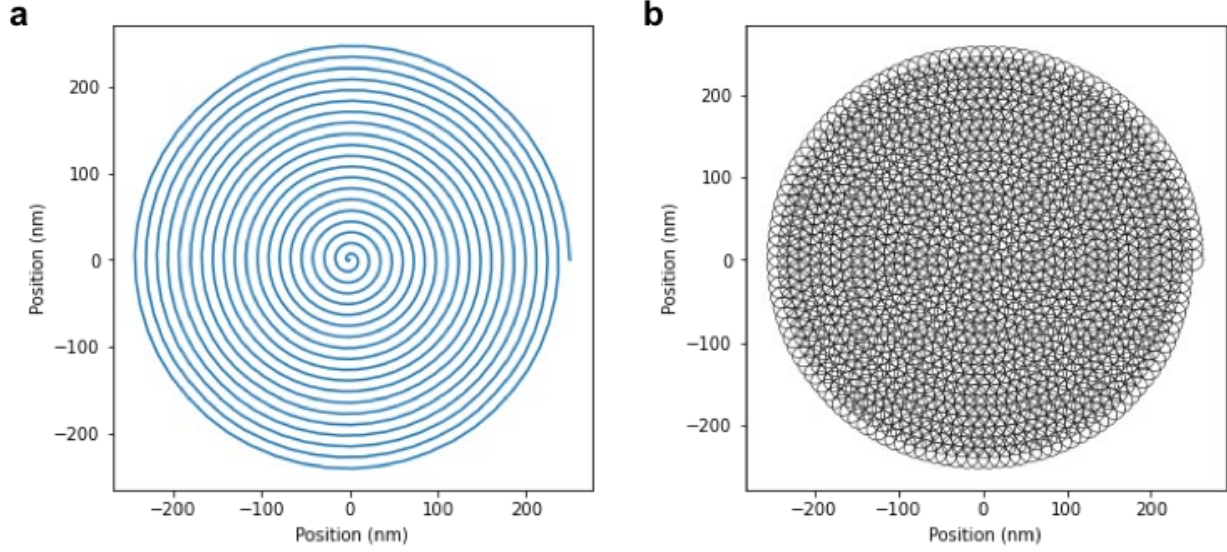


Figure 3.14. Simulating FIB patterning beam path, (a) Plot showing the spiral circle trajectory of the focused ion beam during patterning (b) Plot showing overlapping beam positions at each point along the trajectory for the specified pitch for **Equation 3.15**. Both plots evaluated according to **Equations 3.16-3.18**

$$x_i = \left(\frac{d}{2} - \frac{s\theta_i}{2\pi} \right) \cos \theta_i \quad (3.16)$$

$$y_i = \left(\frac{d}{2} - \frac{s\theta_i}{2\pi} \right) \sin \theta_i \quad (3.17)$$

Where θ_i are given by the pitch constraint:

$$s = \int_{\theta_{i-1}}^{\theta_i} r(\theta) d\theta \quad \text{where } r(\theta) = \frac{d}{2} - \frac{s\theta}{2\pi} \quad (3.18)$$

To model the vacancy concentration profile $n_v(x, z)$ in units of vacancies/nm³ for the 500 nm circle pattern exposed at the lowest FIB level (1 pass), we convolved the single-point vacancy profile for 15 nm hBN $N_{v/Ga^+}^{15}(x, z)$ with the dose profile at $y = 0$ $D_{Ga^+}(x, 0)$:

$$\text{For 1 pass on un-milled surface: } n_v(x, z) = \sum_{x_i=0}^{1000} N_{v/Ga^+}^{15}(x + x_i, z) * D_{Ga^+}(x_i, 0) \quad (3.19)$$

Then, hBN layers that were shown to be milled after 1.3 ms exposure during AFM characterization were then removed from the vacancy profile at the corresponding lateral position according to height versus lateral position data $h_1(x)$:

$$n_{v,1}(x_i, z_i) = \begin{cases} n_v(x_i, z_i), & h_1(x_i) < z_i \\ 0, & h_1(x_i) \geq z_i \end{cases} \quad (3.20)$$

To model the vacancy concentration profile $n_{v,m}(x, z)$ for the next FIB exposure levels ($m = 2, 3,$ and 4 passes), the single-point vacancy profile obtained from SRIM was again convolved with the dose profile at $y = 0$ $D(x, 0)$ for 1 pass with two corrections: (1) $N_{v/Ga^+}^h(x, z)$ used at each x_i of the convolution was dependent on the updated hBN thickness after the previous pass $h_{m-1}(x_i)$. For example, if the AFM height data showed that $h_{m-1}(x_i) = -1$ nm, then the vacancy profile calculated for hBN target layer thickness equal to 14 nm $N_{v/Ga^+}^{14}(x, z)$ was used, if $h_{m-1}(x_i) = -2$ nm, then the vacancy profile obtained for 13 nm hBN $N_{v/Ga^+}^{13}(x, z)$ was used, etc.:

$$\text{For any pass } > 1: n_v(x, z) = \sum_{x_i=0}^{500} N_{v/Ga^+}^{15-h_{m-1}(x_i)}(x + x_i, z) * D_{Ga^+}(x_i, 0) \quad (3.21)$$

(2) This new thickness dependent vacancy profile was added on to the complete vacancy concentration profile for the previous exposure level before removing layers at positions determined by the AFM height data.

$$n_{v,m}(x_i, z_i) = \begin{cases} n_v(x_i, z_i) + n_{v,m-1}(x_i, z_i), & h_m(x_i) < z_i \\ 0, & h_m(x_i) \geq z_i \end{cases} \quad (3.22)$$

Simulated Height Profile: In order to find threshold n_v values for swelling and milling regimes, we first found maximum n_v at each FIB exposure time and fit these values to a linear function for $n_{v \max}(t)$:

$$n_{v \max}(t) = m_v t + b_v \quad (3.23)$$

where m_v is the positive slope in vacancies/(nm³ ms) that characterizes the increase in vacancy concentration with increased FIB exposure levels and b_v is the y-axis intercept.

To determine the vacancy concentration threshold n_v^{mill} after which milling of material would be expected, we normalized and converted calculated $\overline{\Delta z_-}$ values to normalized remaining thickness at each FIB exposure level:

$$h(t) = 1 - \left| \frac{\overline{\Delta z_-(t)}}{h_0} \right| \quad (3.24)$$

where h_0 is the starting un-milled thickness of the flake from which $\overline{\Delta z_-}$ was measured. We fit $h(t)$ to an error function with constant offset c_{mill} , which denotes the maximum value of $h(t)$, and extracted best fit parameters:

$$h_{fit}(t) = \frac{A_{mill}[1 + erf(\alpha_{mill})]}{2} + c_{mill} \quad (3.25)$$

where A_{mill} is the negative amplitude from maximum value to minimum value ($c > A$ with $A < 0$ gives a complementary error function as expected for milling) and $\alpha_{mill} = (t - \mu_{mill})/\sigma_{mill}$ where μ_{mill} is the center location of $A_{mill}/2$ and σ_{mill} sets the characteristic width. We then found a linear fit for the linear regime of the error function:

$$h_{lin}(t) = m_- t + b_{mill} \quad (3.26)$$

where m_- is the negative slope in nm/ms that characterizes the milling rate after the exposure threshold is reached and b_{mill} is the y-axis intercept. To find the threshold exposure level for milling t_{0-} we set the linear model equal to the maximum value $A_{mill} + c_{mill}$:

$$t_{0-} = (A_{mill} + c_{mill} - b_{mill})/m_- \quad (3.27)$$

and then obtained:

$$n_v^{mill} = n_{v_{max}}(t_{0-}) = m_v t_{0-} + b_v \quad (3.28)$$

To determine a vacancy concentration threshold n_v^{swell} for the onset of swelling, values for $\overline{\Delta z_+}$ at each exposure time were fit to an error function with constant offset of the same form as $h_{fit}(t)$ above, but with $A_{swell} > 0$, and best fit parameters were extracted. Then, a linear fit was found for the now positively sloped linear regime and threshold exposure level for swelling to start t_{0+} was found by setting the linear model equal to the minimum value c_{swell} :

$$t_{0+} = (c_{swell} - b_{swell})/m_+ \quad (3.29)$$

and obtaining:

$$n_v^{swell} = n_{v \max}(t_{0+}) = m_+ t_{0+} + b_v \quad (3.30)$$

To determine a vacancy concentration $n_v^{max \ swell}$ where maximum swelling would be observed, after which the swelling goes down until it reaches 0 prior to milling, values for Δz_{+max} at each exposure time were fit to an error function and best fit parameters were extracted. Then, a linear fit was found for the positively sloped linear regime. The exposure level for maximum swelling t_{+max} was found by setting the linear model to $A_{max \ swell} + c_{max \ swell}$:

$$t_{+max} = (A_{max \ swell} + c_{max \ swell} - b_{max \ swell})/m_{+max} \quad (3.31)$$

and obtaining:

$$n_v^{max \ swell} = n_{v \max}(t_{+max}) = m_+ t_{+max} + b_v \quad (3.32)$$

Using the calculated values for n_v^{mill} , n_v^{swell} , and $n_v^{max \ swell}$, we simulated the expected height profile as $\pm \Delta z$ from the reference height z_0 for FIB level 3 and FIB level 4:

$$\Delta z(x) = \begin{cases} 0, & n_v(x) < n_v^{swell} \\ \frac{n_v(x) - n_v^{swell}}{n_v^{max \ swell} - n_v^{swell}}, & n_v^{swell} < n_v(x) \leq n_v^{max \ swell} \\ 1 - \frac{n_v(x) - n_v^{max \ swell}}{n_v^{max \ swell} - n_v^{swell}}, & n_v^{max \ swell} < n_v(x) < n_v^{mill} \\ -\frac{n_v(x) - n_v^{mill}}{n_{v \max} - n_v^{mill}}, & n_v(x) \geq n_v^{mill} \end{cases} \quad (3.33)$$

3.5. Supplementary information

Pre-exposure hBN AFM

After transfer and cleaning of exfoliated HPHT hBN flakes on Si/SiO₂ substrates, we characterized the pre-exposure thickness h_0 via Tapping-Mode AFM and measured 1 μm linecut across the step from substrate to hBN, shown in **Figure 3.15**. Furthermore, the AFM height scans provide a baseline for the qualitative morphological features of the hBN used in this work. We observed none of the randomly located milling and swelling observed in **Figure 3.2**, and can therefore attribute all distinctly visible regions of milling and swelling to be FIB induced.

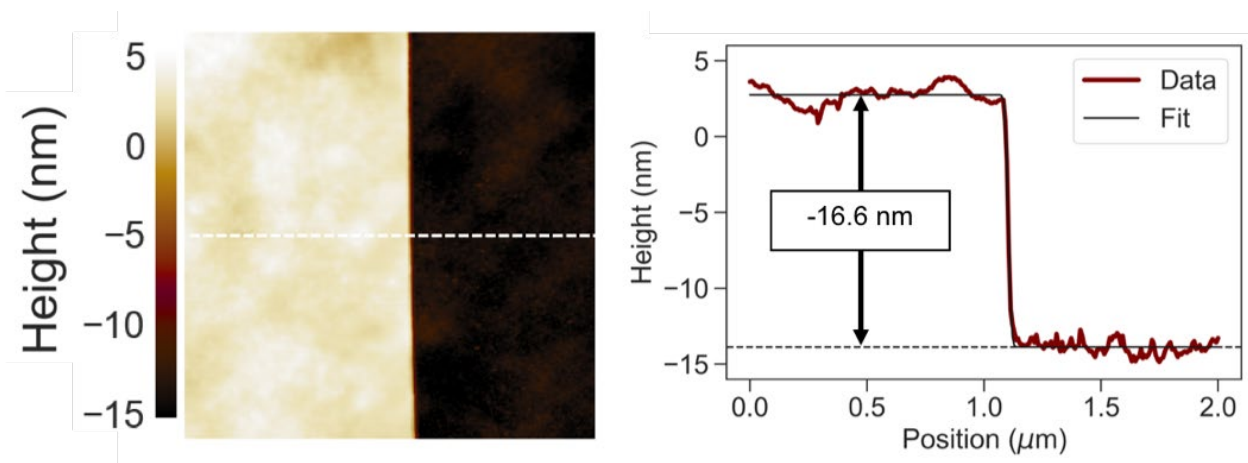


Figure 3.15. Representative AFM height scan data of pre-exposure hBN flake studied in this work, with corresponding linecut and height measurement.

Morphological characteristics as a function of exposure time

Mean calculated values for average swell height, average mill depth, and exposed edge surface area at each FIB exposure level of all samples included in this work are shown below in **Figure 3.16**. The plots for maximum swell height, maximum mill depth, swell volume, and mill volume are shown in the main text in **Figure 3.4**. Average and maximum swell height show similar behavior, as do average and maximum mill depth, mill volume, and exposed edge surface area.

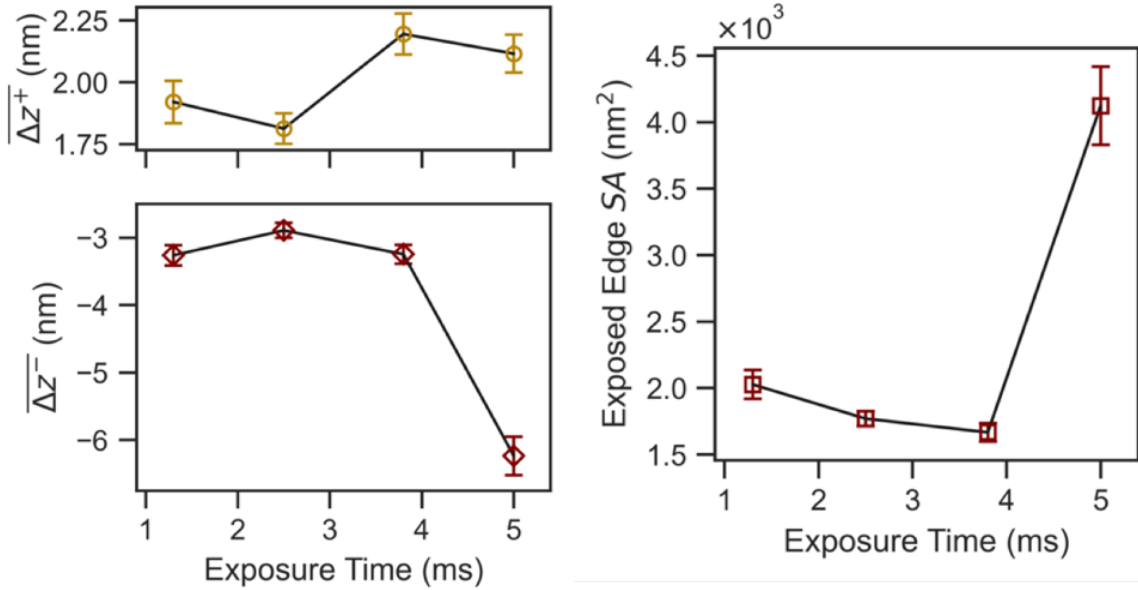


Figure 3.16. Mean calculated values for average heights $\pm\Delta z$ and exposed edge surface area SA at each FIB exposure level of all samples included in this work. The lines connecting data points in are a guide to the eye. Error bars show standard error on the mean.

ZPL & $g^2(0)$ range

We find ZPL in agreement with expected values for hBN quantum emission and observe a distribution of $g^2(0)$. In **Figure 3.12**, we show the ranges of ZPL energies and $g^2(0)$ for all emission sites included in the data and analysis in the main text, a subset of data from **Chapter**

II.

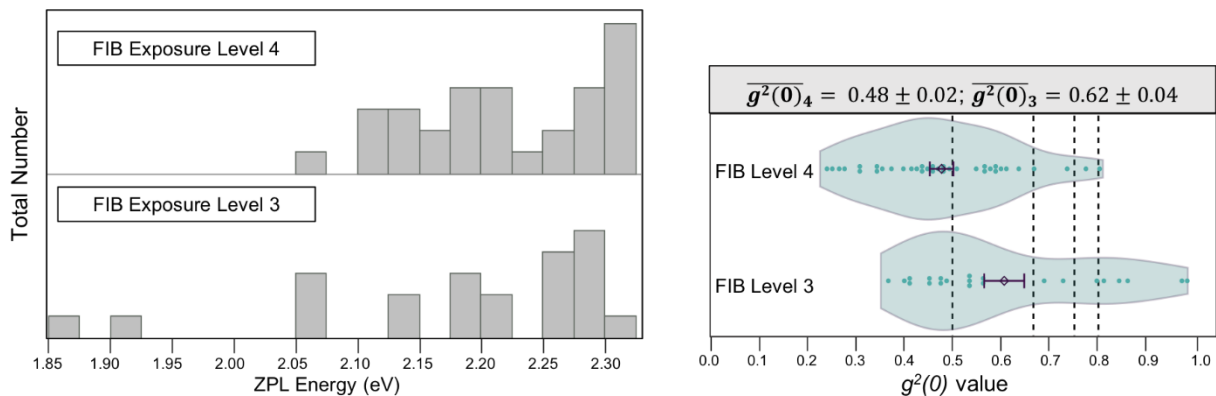


Figure 3.17. Measured values for ZPL and $g^2(0)$ found from the three-level system fit of all emitters optically characterized in this work, showing different values for FIB exposure level 3 and 4. On the $g^2(0)$ distribution, purple diamonds show the average $g^2(0)$ at the specified exposure level and error bars show standard error on the mean standard error on the mean.

3.6. Bridge

In this chapter, I have reported our analysis of focused ion beam induced morphological and structural damage to hexagonal boron nitride crystals during defect engineering. These results allowed us to peek “under the surface” so to speak and therefore correlate quantifiable damage characteristics to color center creation, which provides a route to better control of single photon emitter yields and properties such as the emission energy and quantum purity. While FIB exposure damage alone is an important piece of the SPE fabrication process, we also reported in Chapter II that the interaction of FIB exposure and carbon annealing time influenced optical outputs. Therefore, the next chapter reports our extension of the AFM characterization and correlation of observed damage and optical characteristics across multiple anneal times in order to refine our model for the physical mechanism of defect creation with the combined FIB-carbon annealing technique. Additionally, the simulation results of this chapter are applied to developing the diffusion and defect formation parameters used for our calculations to visualize the refined model in the following chapter.

CHAPTER IV

MODELING EXTRINSIC IMPURITY DIFFUSION FOR COLOR CENTER FORMATION

This chapter contains in-preparation co-authored material; it has been reproduced with permission from: R. Klaiss, J. Ziegler, D. Miller, K. Zappitelli, K. Watanabe, T. Tanaguchi, S.K. Narayanan, P. Dev, B. J. Alemán, “An adjustable focused ion beam – impurity diffusion approach to pattern hexagonal boron nitride quantum emitters.” In this work, I contributed to designing the research, performing the research, analyzing the data, and writing the paper.

4.1. Introduction

Practical devices applied to quantum information technologies require predictable quantum emitter (QE) yields and minimal variation in the emitter properties. However, even the QE fabrication techniques that produce the highest yields are extremely material dependent, only successful in particular regions of the same sample, while others make it challenging to isolate single photons (SPEs). Methods to localize and align hybrid nanostructures to randomly located or unstable emitters do succeed at addressing some of these challenges, but these techniques are not scalable to technologies that rely on arrays of SPEs or simplified device geometries. Therefore, optimizing a pick-and-place defect engineering technique such as the combined focused ion beam (FIB) exposure and carbon annealing technique to pattern SPEs in hexagonal boron nitride (hBN) detailed in Chapter II would provide a more controlled route to scalable emitter integration. However, the number of experiments required to test the many possible

parameter combinations to optimize this technique scales exponentially, making fabrication tedious and impractical.

While our results engineering carbon-based QEs in hBN provide an avenue to integrate emitters in deterministic locations for photonics and quantum sensing applications, our ability to fully optimize this technique is limited by the length of time it takes to fabricate many samples to test different fabrication parameters. In order to reduce our reliance on performing many fabrication experiments, we develop a model for the proposed physical mechanism of our fabrication process by analyzing the interaction of FIB exposure and carbon anneal time through material damage characterization. Furthermore, we apply the model to predict and constrain optimal annealing time ranges for various material damage levels. Additionally, we discuss limitations to the model and how different factors and further calculations could mitigate these limitations, leading to a more robust model.

4.2. Results and discussion

Results from our work using atomic force microscopy (AFM) to characterize surface morphology [**Chapter III**] reveal that the four FIB exposure levels on a single sample (no variation in anneal time) show distinct differences in mill depth and swell/re-deposition height, corresponding to differences in SPE yield and region PL⁵¹. Therefore, we extended this characterization and analysis to samples fabricated with anneal times 1-3 to elucidate how FIB induced damage may be influencing the structural environment for SPE formation and optical characteristics at different anneal times [**Figure 4.1(a)**].

In general, regions fabricated with the 3.8 ms and 5.0 ms FIB exposure times had higher swelling, deeper milling, and dimmer PL (“high damage”) than regions fabricated with the 1.3 ms and 2.5 ms exposure times (“low damage”) [**Supplementary information Tables 4.1-4.2**,

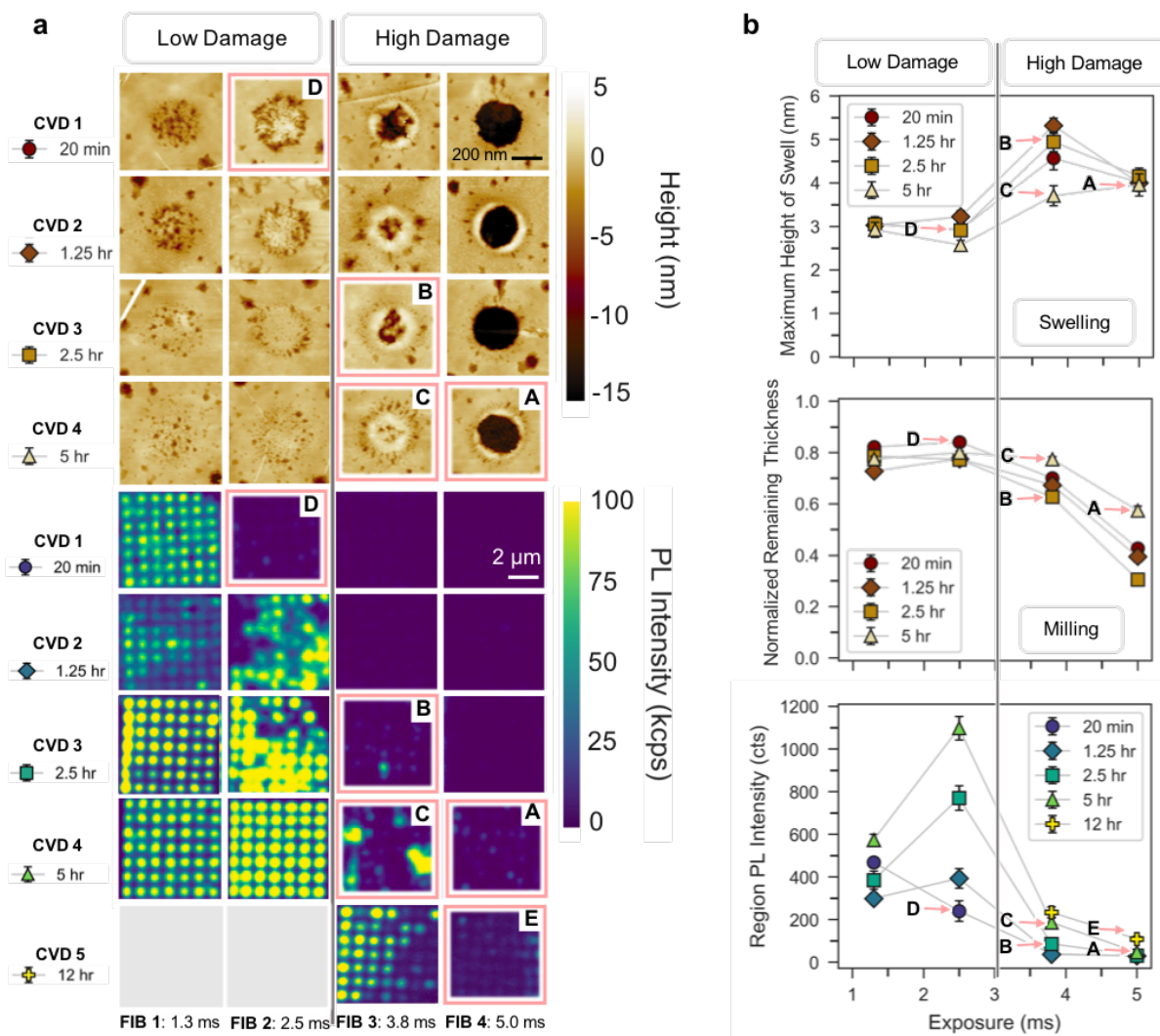


Figure 4.1. Extended atomic force microscopy and photoluminescence characterization (a) Top: Array of AFM height scans of 500 nm holes patterned at all 4 FIB exposure and 4 carbon anneal times; Bottom: Array of 7 μm x 7 μm representative confocal PL scans for each combination of FIB exposure and carbon annealing times (b) Top: Corresponding plots of average magnitude swell height and average normalized remaining thickness (calculated from mill depth) at each FIB exposure time calculated from AFM scans; Bottom: Interaction plot showing average PL map intensity for each combination of FIB exposure and carbon annealing times. A, B, C, D, E labels correspond to the same FIB and carbon annealing combinations from Figure 2.5 for the conditions that produced the highest probability of QEs. Error bars indicate standard error on the mean.

Chapter II Supplementary information Table 2.9 Tukey-Kramer HSD: $p < 0.0001$] [Figure 4.1(b)]. Consistent with our previous results for all but the 20 min anneal, PL got brighter first at the 2.5 ms exposure time before it got dimmer [Chapter II Supplementary information Table

2.9 Tukey-Kramer HSD: $p < 0.0001$]. In fact, 2.5 ms FIB exposure and 20 min anneal (D) was the only combination that produced SPEs in low damage samples. We conjecture that due to the longer exposure time compared to 1.3 ms exposure, the 2.5 ms exposed regions actually contained more surface damage not quantifiable as swelling or milling and therefore fewer atomic defects available near the surface to form color centers, thereby leading to isolated SPEs and dimmer PL overall at the shortest anneal time.

Carbon annealing is required for color center formation with this technique. The carbon we deposit with this process must diffuse into the crystal and annihilate or bind with point vacancies created by FIB exposure. FIB exposure also creates high defect density regions that are extremely damaged, demonstrating swelling due to amorphous binding, structural voids, and breakage. We expect that this damage changes the migration barrier E_b for impurity in the material due to screening, trapping in voids, etc., thereby changing the diffusion constant $D \propto e^{-E_b/k_B T}$ and ultimately the time it takes for impurities to diffuse through material ($t \sim l^2/D$).

Based on our data that regions patterned with longer FIB exposure (thereby sustaining high levels of damage) required longer anneal times to yield SPEs, we propose a multi-layer diffusion model for the physical mechanism of defect formation where carbon diffuses through two distinct morphologies to form color centers: 1) highly damaged due to continuous, directed exposure leading to swelling and milling (D_{HD}) and 2) lower damaged due to the gaussian tail of the FIB leading to overall lower dose exposure creating isolated vacancies (D_{LD}) [(**Figure 4.2(a)**)]. Stopping and Range of Ions in Matter (SRIM) calculations from our previous work⁵¹ show clear distinctions between high defect concentration and low defect concentration regions for each dose. We denote the dose dependent characteristic lateral damage length as l . [(**Figure 4.2(b)**)].

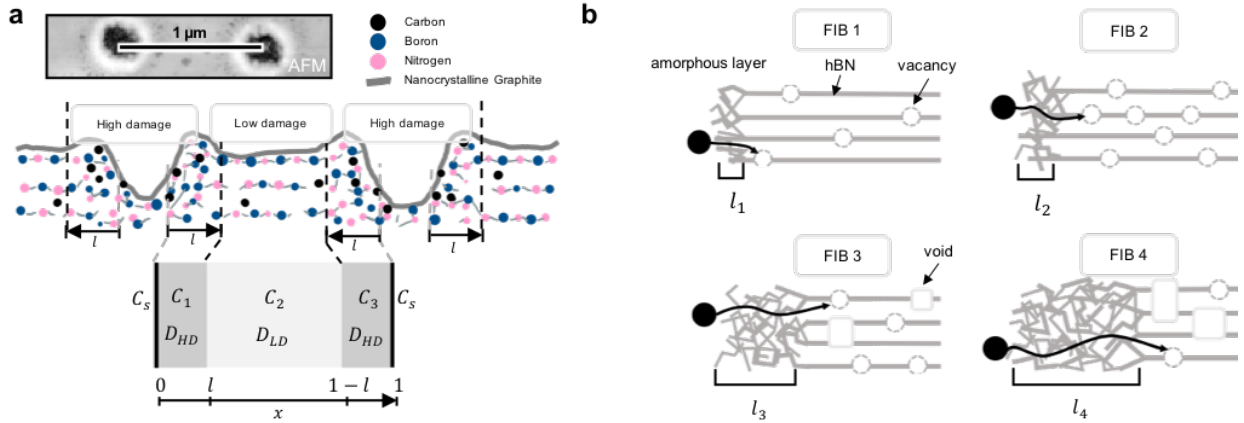


Figure 4.2. Illustrations demonstrating multilayer diffusion model formulation (a) Sketch showing the region limits for multilayer diffusion model based on FIB damage, where labels are defined in main text Inset: AFM image of FIB patterned holes showing swelling around edge region (b) Sketch demonstrating how FIB induced damage influences the number of potential color centers (and therefore dimmer or brighter PL) based on the conditions that impurity carbon must diffuse through for each FIB exposure level.

We model the carbon concentration for a given FIB exposure level (constant l) via diffusion in composite media in 1D:

$$\frac{\partial C_i}{\partial t} = D_i \frac{\partial^2 C_i}{\partial x^2} \quad (4.1)$$

$$i = 1,2,3 ; D_1 = D_3 = D_{HD} ; D_2 = D_{LD}$$

with perfect matching at interfaces:

$$D_i \frac{\partial C_i}{\partial x} \Big|_{l_-} = D_{i+1} \frac{\partial C_{i+1}}{\partial x} \Big|_{l_+} \quad (4.2)$$

and constant surface concentration:

$$C(0, t) = C_s \quad (4.3)$$

$$C(1, t) = C_s \quad (4.4)$$

where C_s is the surface concentration of nanocrystalline graphite deposited on the hBN surface during the anneal process.

For a given color center with formation energy ΔE_f^D , the probability that impurity carbon of concentration $C(t)$ will annihilate with one vacancy out of N_v^D vacancies to yield a single color center (i.e. one isolated SPE) as a function of time would follow a Boltzmann distribution:

$$p_{SPE}(t) = \frac{\frac{N_v^D C(t)}{n_S} e^{-\beta n \Delta E_f^D}}{1 + \sum_{n=1}^{N_v^D} \frac{1}{n!} \left(\frac{N_v^D C(t)}{n_S}\right)^n e^{-\beta n \Delta E_f^D}} \quad (4.5)$$

This model for the SPE yield predicts the experimentally observed behavior of longer carbon annealing producing higher SPE yields for high FIB exposure, but lower yields for lower exposure [Figure 4.3]. For more information about the calculations and system parameters used to evaluate the model, refer to 4.4 Methods and 4.5 Supplementary information.

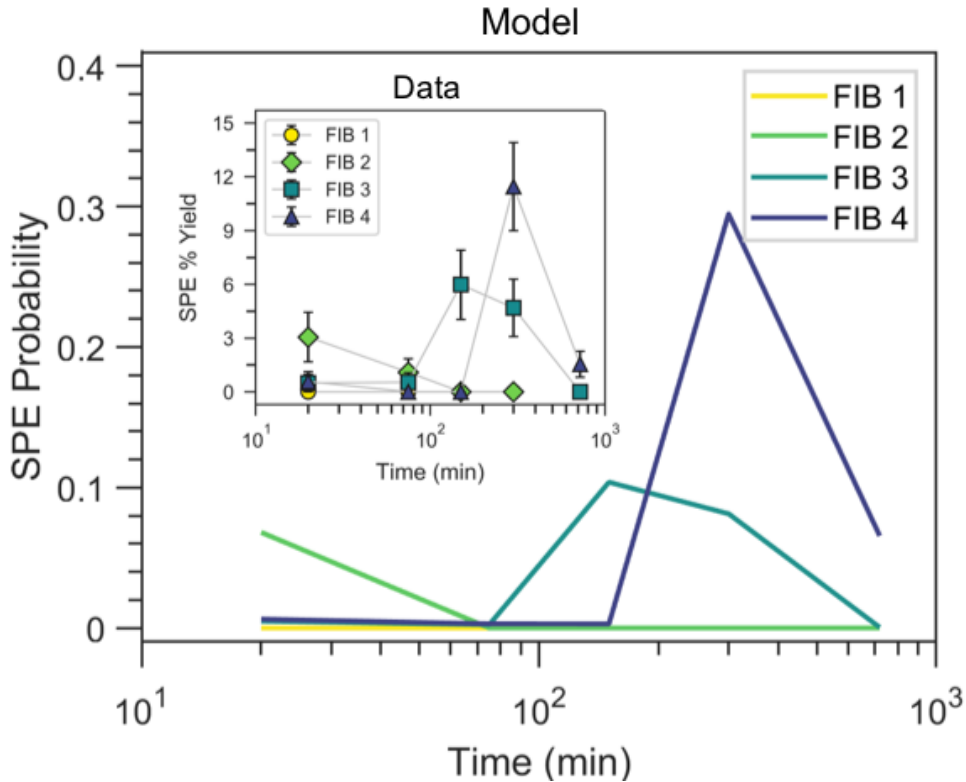


Figure 4.3. Evaluated model at tested anneal times Plot of results from the evaluated model using a parameter set [Supplementary information Table 4.3] that reproduces the behavior we see in data for SPE yield at the tested anneal times

Furthermore, when we extended this multi-layer diffusion model to anneal times not tested, we observed that the anneal time when the SPE yield peaks was highly dependent on the damage diffusion constant, the damage length, the number of vacancies available, and the defect formation energy, but preserves the same qualitative behavior and saturates at the expected Poissonian limit [Figure 4.4]. Full results analyzing these single factor effects on the model output as well as interaction effects can be found in 4.5 Supplementary information.

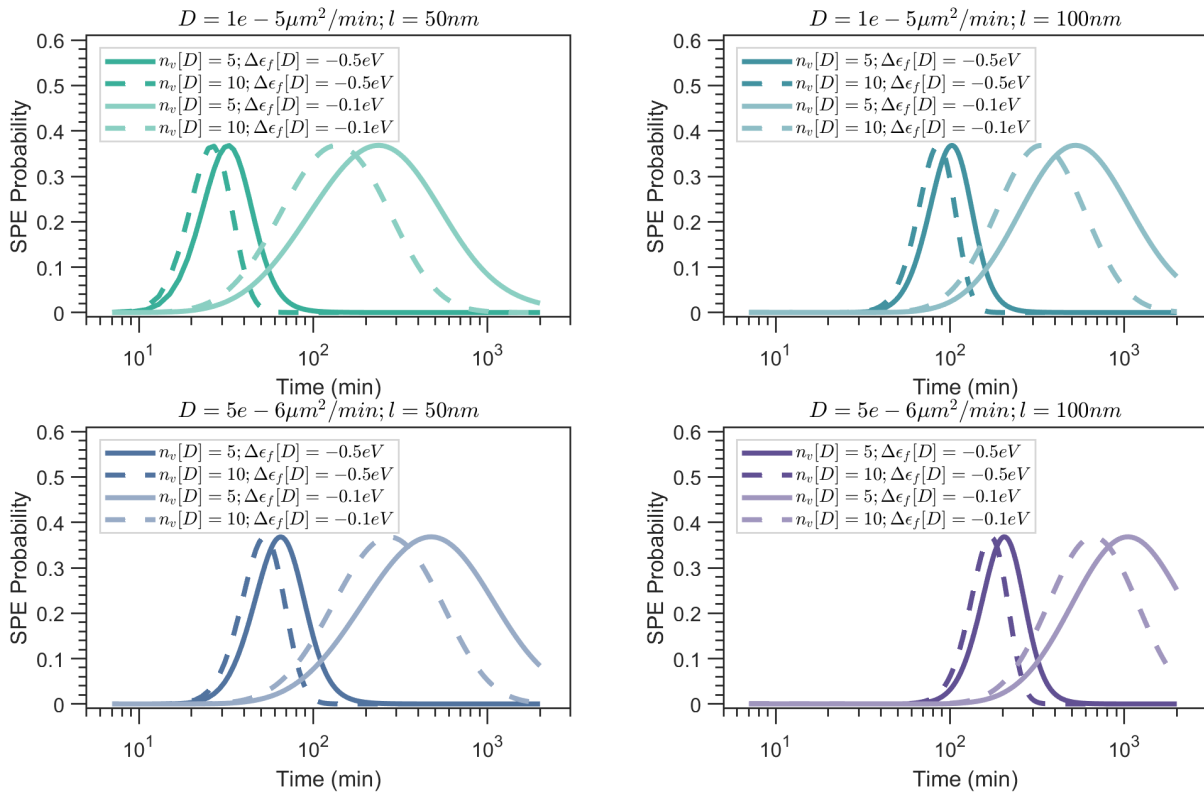


Figure 4.4. Model parameter dependence of SPE supersaturation characteristics Plot of results from the evaluated model labeled by variations to the default parameter set, demonstrating the dependence of the single-color center creation probability on the high damage diffusion constant, damage length, available vacancy number, and defect formation energy

Based on this result, we expect that the ideal annealing time to produce SPEs on samples exposed at our first two FIB exposure levels lies below 20 min, as those regions quickly reached supersaturation of color centers. Ultimately, we conjecture that SPE fabrication would be most successful for a given FIB exposure level with known or calculated damage region length and

vacancy concentration at some onset time prior to the supersaturation limit. Moreover, a more complete model including formation energies for multiple defect types could provide a value for this time parameter, as the defect formation energy strongly influences the anneal time response for optimal SPE probability.

To constrain the likely defects formed under these conditions, we refer to previous studies that have matched observed ZPLs to calculated ZPLs via Density Functional Theory (DFT) and molecular dynamics (MD). Mendelson et. al. put forth the $V_{\text{B}}\text{C}_{\text{N}}^-$ defect center as the source of observed visible range single photon emission with ZPL in the range of 585 ± 10 nm (2.12 eV)⁴⁰, while Fischer et. al. favor the $V_{\text{N}}\text{C}_{\text{B}}$ defect center with ZPL observed at 2.2 eV³⁷. However, it should be pointed out that, to date, the aforementioned defects remain controversial. For instance, our DFT calculations show that $V\text{BCN}^-$ is a spin-1/2 defect, and not a spin-3/2 defect as was calculated for a small few-ring flake of hBN⁴⁰. **Supplementary information Figure 4.8(b)** shows defect formation energy for the VBCN defect in different charge states as a function of electronic chemical potential. The three most favorable charge states are 0, -1 and -2, out of which only first two are spin active, with spins of 1 and 1/2, respectively and so, this defect might not be the one observed in experiment by Mendelson et. al.. Also, according to our DFT calculations, the neutral $V\text{NCB}$ is not spin active, with the non-magnetic solution being the lower energy state, which was missed by earlier works⁹⁴. Amongst the energetically most favorable charge states (+2, +1 and 0) shown in **Supplementary information Figure 4.8(c)**, only +1 charge state is spin-active and has a spin-1/2, which was also reported previously⁹⁵. Additionally, our high-energy FIB exposure technique likely produces not only single point vacancies and divacancies, but also larger clusters, allowing a class of emitters that contain many carbons in a

cluster⁹⁶. One such defect candidate in the range of our observed emission is C₂C_N, modeled by Li et. al. with ZPL of 2.13 eV⁹⁷.

We expect that likely defect candidates will vary based on the particular combination of FIB exposure and carbon annealing time due to differences in vacancy concentration, cluster size, and carbon concentration profile among the samples studied in this work. This is supported by the observed ZPL differences reported in Chapter II [**Figure 2.6(b)**]. Additionally, the structural environment within the 2.5 ms exposed regions is markedly different from the environment for the 3.8 ms and 5.0 ms exposed regions, altering the initial vacancy concentration and cluster size conditions, as well as local strain gradients and substrate interactions as reported in Chapter III and in **Figure 4.1**. Furthermore, the SPEs fabricated with the 2.5 ms exposure time were possible only when annealed for the shortest time, while those created in the 3.8 ms and 5.0 ms exposed material were created with the highest carbon annealing times, directly impacting the total carbon dose available. While we cannot conclusively put forth a particular defect complex responsible for the emission we observe from SPEs fabricated with this technique, further characterization of the photophysics of these emitters such as polarization and ODMR as well as DFT and MD calculations for larger carbon-based defects could narrow the range of defect candidates possible for different combinations of FIB exposure and carbon doping levels and provide more information to elucidate the anneal time dynamics of color center creation.

There are further non-trivial limitations to elucidating a quantitative model for defect formation in FIB exposed hBN doped via carbon diffusion. The Monte Carlo method used by SRIM to calculate ion induced vacancy concentration do not fully account for sputtering and self-annealing, whereas the sputtered volume and stability of large structural voids are important considerations in our study of optimal SPE creation. Additionally, evaluating the diffusion

problem in greater than one dimension would provide a more precise concentration model. Furthermore, the diffusion constants of carbon in hBN could be even more strongly dependent on the surrounding damage environment and vary not just between the high damage and low damage regimes but may be a continuous function of position $D(x)$ that is unique for each exposure level. However, comparing our results to this qualitative model allows us to constrain different testable regimes of FIB exposure and carbon annealing time to optimize and expand this fabrication technique. Allowing for more refined control over the design of devices and selection of fabrication parameters to align with requirements for different hBN QE reliant applications.

4.3. Conclusions

In this work, we used AFM height data and confocal PL images of hBN regions subjected to 18 different combinations of FIB exposure dose and carbon diffusion time to elucidate that carbon impurities likely diffuse through layers of highly damaged material indicated by swelling in order to activate color centers. Additionally, by simulating our technique using SRIM and a multilayer-diffusion model, we determined that in general, less damaged regions required shorter diffusion times with more precision on the order of minutes, while more damaged regions required longer diffusion times with less precision on the order of hours, and demonstrated a method to constrain the optimal range of diffusion time for a given amount of FIB induced damage to produce SPEs. These results, combined with DFT calculations and potential future work to characterize polarization and spin characteristics of these patterned emitters could allow for both higher resolution spatial control and predictable chemical structure control over defect creation, thereby making hBN SPE integration more broadly applicable and scalable for a range of quantum information technologies.

4.4. Methods

AFM Characterization: AFM height data was collected and analyzed according to **3.4**

Methods.

Multi-layer Diffusion Defect Formation Model: We employed the semi-analytical solution to the multilayer diffusion problem based on the Laplace transform eigenfunction expansion and corresponding MATLAB code published by Carr and Turner to solve for $C_i(x, t)$ at each anneal time⁹⁸. Parameter values for diffusivities and damage lengths were determined by order of magnitude estimations informed by literature, previous work, and data, and can be found in the **Supplementary information**.

We determined an estimate for $N_{v[D]}(x)$ at each tested exposure dose by convolving SRIM calculations with AFM linecuts [refer to morphology paper] and assuming that of all of the calculated point vacancies and vacancy complexes, only a small percentage (~1%) would 1) have a formation energy low enough to form a defect complex with carbon and 2) when the complex is formed, would be optically active under 532 nm excitation. $p_{SPE}(t)$ to produce **Figures 4.3** and **4.4** were calculated in MATLAB using the evaluated solutions for $C_i(x, t)$.

Ab-initio Calculations: Spin-polarized DFT calculations were performed within the generalized gradient approximation⁹⁹ of Perdew-Burke-Ernzerhof¹⁰⁰ as implemented in the Quantum Espresso package.¹⁰¹ A $6 \times 6 \times 1$ (72-atoms) supercell of hBN was used in the calculations. The Brillouin zone was sampled using a Γ -centered, $4 \times 4 \times 1$ k-grid, which was created within the Monkhorst-Pack scheme.¹⁰² A 20 Å vacuum layer was added in the direction normal to the hBN surface, ensuring minimal interactions between periodic images in the z-direction. The formation energies of the defects were calculated according to the following expression¹⁰³:

$$\Delta E_{form}^{Defect;q} = E_{Total}[defect, q] - E_{Total}[pristine] - \sum n_i \mu_i + q(E_{VBM}[defect] + E_F) \quad (4.6)$$

Here, q is the charge of the defect, n_i (μ_i) represent the number (chemical potential) of the i^{th} species of atoms that are removed and/or added, E_{Total} represents total energy of the defective/pristine supercell, E_F is the Fermi level (electronic chemical potential) relative to the valence band maximum (VBM). The E_{VBM} of the defective supercell is calculated using:

$$E_{VBM}[defect] = E_{VBM}[pristine] + V_{av}[defect] - V_{av}[pristine] \quad (4.7)$$

where, the difference in the average potentials (V_{av}) is used to line up the band structures of the perfect and the defective supercells. Also, for the pristine supercell, one finds the VBM as follows: $E_{VBM}[pristine] = E_{Total}[pristine, q = 0] - E_{Total}[pristine, q = +1]$. The growth conditions are accounted for in the choice of chemical potentials (μ_i), which represent energies of reservoirs with which atoms are being exchanged, along with the requirement that under equilibrium conditions: $E(hBN) = \mu_B + \mu_N$. Here, $E(hBN)$ is total energy of pristine hBN unit cell. For example, in the boron rich conditions, the chemical potential for boron, μ_B , is obtained using the total energy of α -boron unit cell: $\mu_B = E(\alpha B)/12$, while $\mu_N = E(hBN) - \mu_B$. In nitrogen-rich condition, N_2 is used as a reference to obtain the chemical potential for nitrogen, μ_N , giving $\mu_N = E(N_2)/2$ and $\mu_B = E(hBN) - \mu_N$. Also, we used graphene as a reference to obtain the chemical potential for carbon, μ_C , in these calculations. We neglected charged defect corrections because they are not expected to affect the qualitative behavior comparing reference structure defect formation energies nor spins calculated for this work. Therefore, our calculations provide an upper bound on the defect formation energies.

4.5. Supplementary information

AFM Characterization

We report the results of Student's t and Tukey-Kramer HSD Mean Comparison Tests for average mill depth and swell height at each exposure time averaged over all anneal times in **Tables 4.1** and **4.2** respectively, as referenced in **4.2 Results and discussion**.

Table 4.1. Average Mill Depth by FIB Exposure time– Mean Comparison Tests where averages contain values for samples carbon annealed for 20 min, 1.25 hr, 3 hr, and 5 hr. $\alpha = 0.05$ significance level, unequal variance

Exposure 1 – Exposure 2	Difference	Standard Error Difference	p-value (Student's t Each Pair)	p-value (Tukey-Kramer HSD All Pairs)
2.5 ms – 5.0 ms	5.22	0.16	< 0.0001	< 0.0001
1.25 ms – 5.0 ms	4.93	0.16	< 0.0001	< 0.0001
3.75 ms – 5.0 ms	3.69	0.16	< 0.0001	< 0.0001
2.5 ms – 3.75 ms	1.52	0.16	< 0.0001	< 0.0001
1.25 ms – 3.75 ms	1.23	0.16	< 0.0001	< 0.0001
2.5 ms – 1.25 ms	0.29	0.16	0.0718	0.2729

Table 4.2. Average Swell Height by FIB Exposure time– Mean Comparison Tests where averages contain values for samples carbon annealed for 20 min, 1.25 hr, 3 hr, and 5 hr. $\alpha = 0.05$ significance level

Exposure 1 – Exposure 2	Difference	Standard Error Difference	p-value (Student's t Each Pair)	p-value (Tukey-Kramer HSD All Pairs)
3.75 ms – 2.5 ms	0.570	0.064	< 0.0001	< 0.0001
3.75 ms – 1.25 ms	0.518	0.064	< 0.0001	< 0.0001
5.0 ms – 2.5 ms	0.498	0.064	< 0.0001	< 0.0001
5.0 ms – 1.25 ms	0.446	0.064	< 0.0001	< 0.0001
3.75 ms – 5.0 ms	0.072	0.064	0.2650	0.6801
1.25 ms – 2.5 ms	0.052	0.064	0.4163	0.8482

Data for all calculations from AFM height data collected for this chapter is shown in **Figure 4.5**.

Multi-layer diffusion model

When determining the diffusion time for carbon impurities during the CVD/anneal process, we do not account for the mass transport time of reactants to the hBN surface due to the high concentration of ethylene flow and low-pressure conditions of the CVD process causing growth

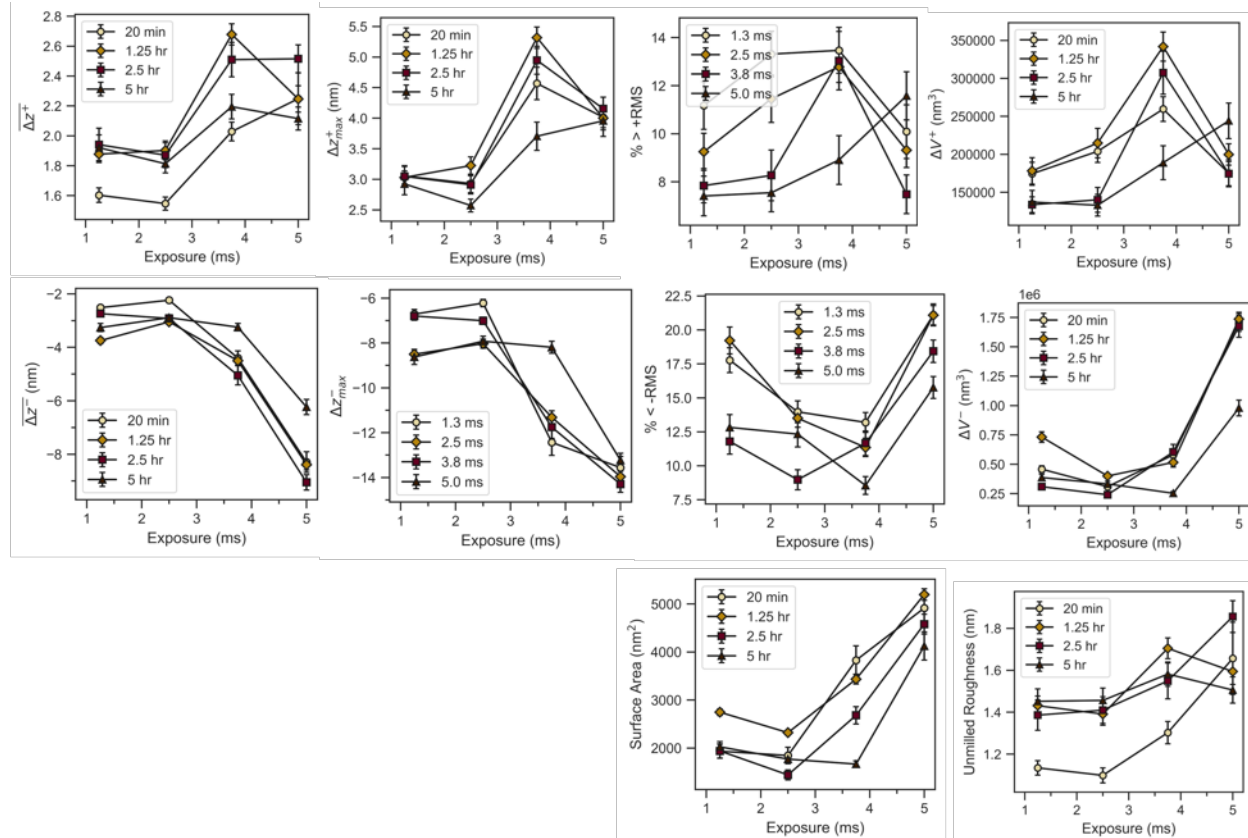


Figure 4.5. Full AFM characterization at 4 different anneal times Plots showing average values and standard error on mean for all morphological characteristics outlined in **Chapter III** for all FIB exposure-carbon annealing combination (12 hour anneal samples not characterized)

to occur on shorter time scales than the diffusion. We choose to model in 1D because the in-plane (between layers) diffusivity of impurities in hBN is orders of magnitude higher than the out-of-plane (through layers) diffusivity. Additionally, we do not account for the diffusion of vacancy defects because at the process temperature, mono- and di-vacancies quickly reach equilibrium concentrations.

We determined four different values of l corresponding to expected damage levels for FIB exposure based on AFM data, swelling and milling calculations, and SRIM studies performed for our previous work. We set the ratio of diffusivities in the high damage and low damage regions based on literature values for intercalated carbon in hBN and order of magnitude estimations. All model parameters used in the MATLAB calculations are shown in **Table 4.3**. Furthermore, the

evaluated carbon concentrations for each of the simulated FIB levels intended to replicate our experimental conditions are displayed in **Figure 4.6**.

Table 4.3. Model Parameters Used for Figure 4.3

Parameter	Variable	Value
Normalized Surface Concentration	C_S	1
High-Damage Diffusion Constant ($\mu\text{m}^2/\text{min}$)	D_{HD}	9×10^{-6}
Low-Damage Diffusion Constant ($\mu\text{m}^2/\text{min}$)	D_{LD}	10^2
Lateral Damage Length (nm)	$\{l_1, l_2, l_3, l_4\}$	$\{5, 72, 187, 240\}$
Unbound Site Concentration	n_S	1
Number of Sites to form defects	$\{N_{v_1}^D, N_{v_2}^D, N_{v_3}^D, N_{v_4}^D\}$	$\{5, 15, 3, 2\}$
Defect Formation Energy (eV)	ΔE_f^D	-0.8

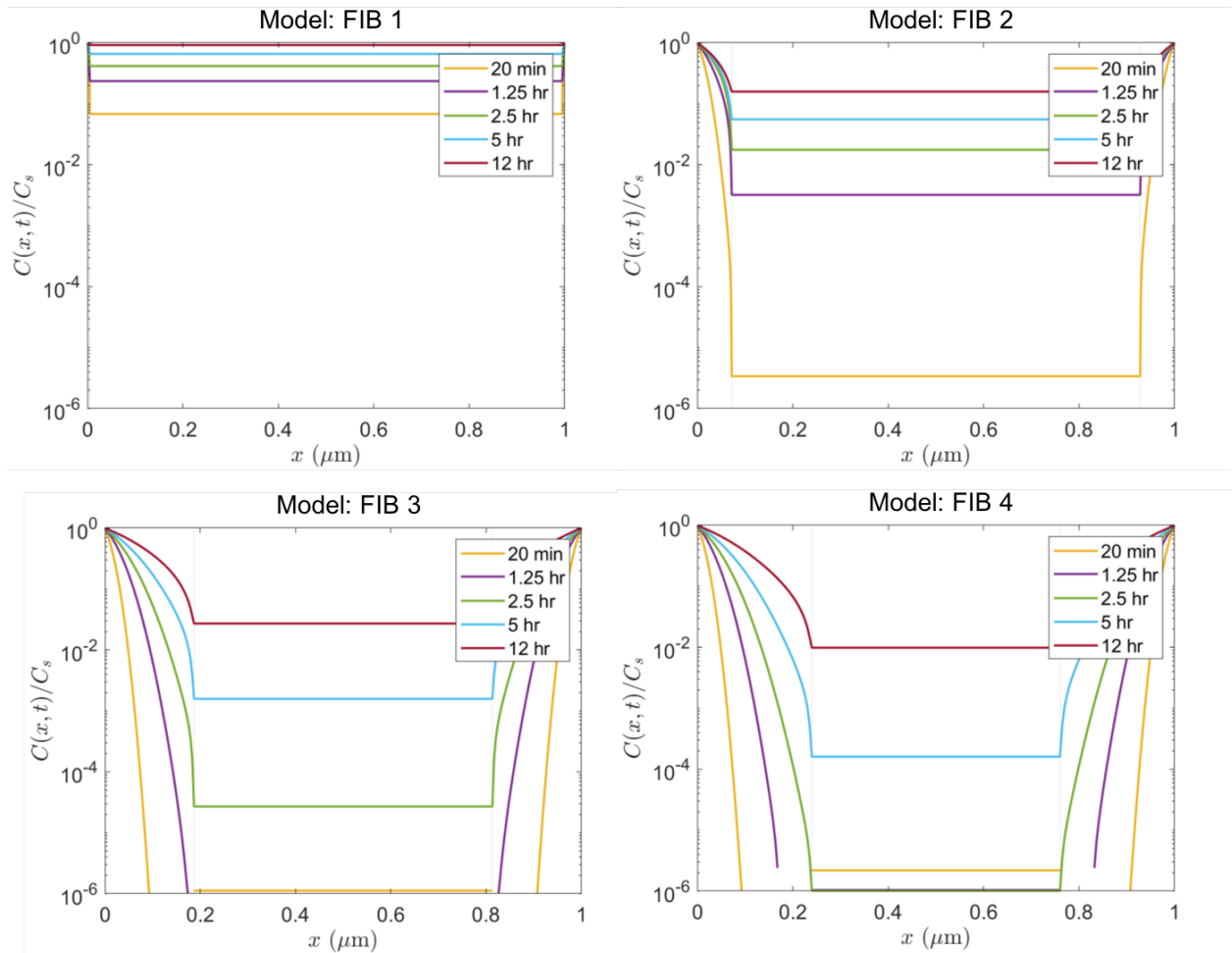


Figure 4.6. Multi-layer diffusion carbon concentration profiles evaluated using the semi-analytical solution multilayer diffusion problem in MATLAB for parameters [Table 4.3] used to calculate the probability of 1 color center at a pattern [Figure 4.3]

Color Center Yield Calculation

Calculating Boltzmann distribution: The diagram shown in **Figure 4.7** demonstrates the process for calculating the single color center probability as a function of time via the Boltzmann distribution, where N_C is the number of carbon impurity atoms, N_S is the number of free sites for intercalated carbon with energy E_{C_i} , and N_v^D is the number of sites where carbon can form a stable, optically active defect with energy E_f^D .

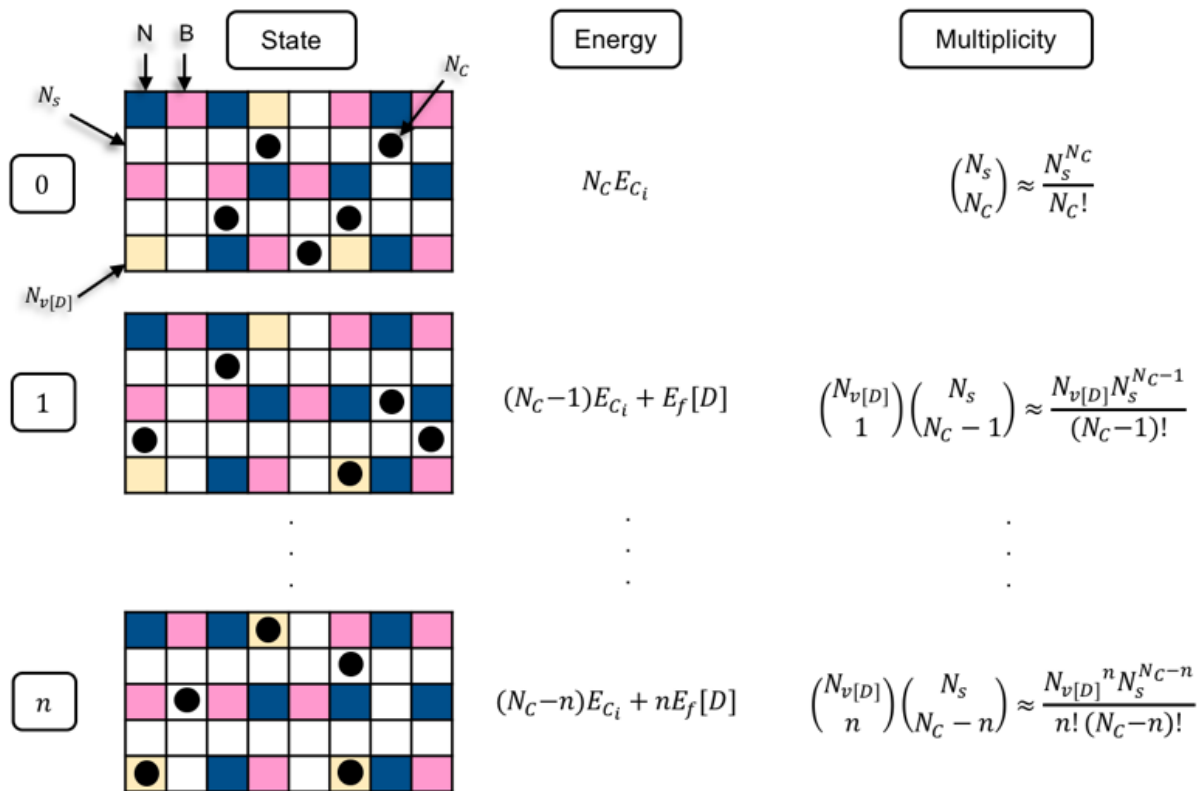


Figure 4.7. Illustration of Boltzmann distribution model for defect formation demonstrating the energy and multiplicity calculations for the no color center ($n = 0$) state, the single color center ($n = 1$) state, and the many color center ($n = n$) state

For state with no carbons in stable optically active defect, the energy is $N_C E_{C_i}$ and the multiplicity of that state is

$$\binom{N_S}{N_C} = \frac{N_S!}{N_C! (N_S - N_C)!} \approx \frac{N_S^{N_C}}{N_C!} \quad (4.8)$$

For state with 1 carbon in stable optically active defect, the energy is $(N_C - 1)E_{C_i} + E_f^D$ and the multiplicity of that state is

$$\binom{N_v^D}{1} \binom{N_S}{N_C - 1} = \frac{N_v^D!}{1! (N_v^D - 1)!} \frac{N_S!}{N_C! (N_S - N_C + 1)!} \approx \frac{N_v^D N_S^{N_C - 1}}{(N_C - 1)!} \quad (4.9)$$

Generalizing to n carbons in stable optically active defect, the energy is $(N_C - n)E_{C_i} + nE_f^D$ and the multiplicity of that state is

$$\binom{N_v^D}{n} \binom{N_S}{N_C - n} = \frac{N_v^D!}{n! (N_v^D - n)!} \frac{N_S!}{N_C! (N_S - N_C + n)!} \approx \frac{N_v^{Dn} N_S^{N_C - n}}{n! (N_C - n)!} \quad (4.10)$$

The probability of forming exactly 1 defect in the region with N_C carbons and $N_{v[D]}$ available defect sites follows the Boltzmann distribution, generally:

$$p_{SPE} = \frac{\sum \text{all 1 states}}{\sum \text{all possible states}} \quad (4.11)$$

And substituting the state energies and multiplicities from **Equations 4.8-4.10**:

$$p_{SPE} = \frac{\frac{N_v^D N_S^{N_C - 1}}{(N_C - 1)!} e^{-\beta((N_C - 1)E_{C_i} + E_f^D)}}{\sum_{n=0}^{N_v^D} \frac{N_v^{Dn} N_S^{N_C - n}}{n! (N_C - n)!} e^{-\beta((N_C - n)E_{C_i} + nE_f^D)}} \quad (4.12)$$

Which we then evaluate:

$$\begin{aligned} &= \frac{\frac{N_C}{N_C} \frac{N_v^D N_S^{N_C - 1}}{(N_C - 1)!} e^{-\beta N_C E_{C_i}} e^{\beta E_{C_i}} e^{-\beta E_f^D}}{\frac{N_S^{N_C}}{N_C!} e^{-\beta N_C E_{C_i}} + \sum_{n=1}^{N_v^D} \frac{N_C!}{N_C!} \frac{N_v^{Dn} N_S^{N_C - n}}{n! (N_C - n)!} e^{-\beta N_C E_{C_i}} e^{\beta n E_{C_i}} e^{-\beta n E_f^D}} \\ &= \frac{\frac{N_S^{N_C}}{N_C!} e^{-\beta N_C E_{C_i}} \frac{N_v^D N_C}{N_S} e^{\beta E_{C_i}} e^{-\beta E_f^D}}{\frac{N_S^{N_C}}{N_C!} e^{-\beta N_C E_{C_i}} + \frac{N_S^{N_C}}{N_C!} e^{-\beta N_C E_{C_i}} \sum_{n=1}^{N_v^D} \frac{N_C!}{n! (N_C - n)!} \frac{N_v^{Dn}}{N_S^n} e^{\beta n E_{C_i}} e^{-\beta n E_f^D}} \end{aligned}$$

Simplifying $\frac{N_C!}{n!(N_C - n)!} \approx \frac{N_C^n}{n!}$ and setting the defect formation energy $\Delta E_f^D = E_f^D - E_{C_i} < 1$:

$$p_{SPE} = \frac{\frac{N_v^D C}{n_s} e^{-\beta n \Delta E_f^D}}{1 + \sum_{n=1}^{N_v^D} \frac{1}{n!} \left(\frac{N_v^D C}{n_s} \right)^n e^{-\beta n \Delta E_f^D}} \quad (4.13)$$

where the carbon concentration $C = \frac{N_C}{V}$ and the free site concentration $n_s = \frac{N_S}{V}$.

The same procedure was followed to find the probability of any number of defects, generally:

$$p_D = \frac{\sum \text{all } n > 0 \text{ states}}{\sum \text{all possible states}} \quad (4.14)$$

Substituting again from **Equations 4.8-4.10**:

$$= \frac{\frac{N_S^{N_C}}{N_C!} e^{-\beta N_C E_{C_i}} \sum_{n=1}^{N_v^D} \frac{N_C!}{n! (N_C - n)!} \frac{N_v^D^n}{N_S^n} e^{\beta n E_{C_i}} e^{-\beta n E_f^D}}{\frac{N_S^{N_C}}{N_C!} e^{-\beta N_C E_{C_i}} + \frac{N_S^{N_C}}{N_C!} e^{-\beta N_C E_{C_i}} \sum_{n=1}^{N_v^D} \frac{N_C!}{n! (N_C - n)!} \frac{N_v^D^n}{N_S^n} e^{\beta n E_{C_i}} e^{-\beta n E_f^D}}$$

And simplifying to obtain

$$p_D = \frac{\sum_{n=1}^{N_v^D} \frac{1}{n!} \left(\frac{N_v^D C}{n_s} \right)^n e^{-\beta n \Delta E_f^D}}{1 + \sum_{n=1}^{N_v^D} \frac{1}{n!} \left(\frac{N_v^D C}{n_s} \right)^n e^{-\beta n \Delta E_f^D}} \quad (4.15)$$

Model Parameters Full Model Effects Test

To determine the model parameters that most strongly influence the optimal anneal time to maximize the SPE probability, we tested high and low values of the following four factors: damage diffusion constant (5E-6 $\mu\text{m}^2/\text{min}$, 1E-5 $\mu\text{m}^2/\text{min}$), damage length (50 nm, 100 nm), number of appropriate vacancy sites (5,10), and defect formation energy (-0.5 eV, -0.1 eV), with 11 replicates for each of the 16 parameter combinations. Error was introduced for each replicate via the diffusion time parameter, where all calculations were performed over the time range 7E0 min to 3E3 min for 1000 randomly spaced points and the random seed was different for each calculation.

The response variables tested were time of maximum SPE probability ($t_{max\ SPE}$), time of SPE onset ($t_0 = t(p_{SPE} \geq 0.01)$), and color center saturation time ($t_{sat} = t_{max\ SPE} - t_0$).

Average values for each response variable for all 16 combinations are shown in **Tables 4.4, 4.5, and 4.6** respectively. Single factor and interaction effects with corresponding p-values are shown for each of the response variables in **Tables 4.7, 4.8, and 4.9**, respectively.

Table 4.4. Model Parameter 2⁴ Results –Time of Max SPE Probability

Experiment (D_{HD} , l , N_v^D , ΔE_f^D)	$t_{max\ SPE}$ (Mean \pm Std Err) [min]
1E-6 $\mu\text{m}^2/\text{min}$, 50 nm, 10, -0.5 eV	26.47 \pm 0.22
1E-6 $\mu\text{m}^2/\text{min}$, 50 nm, 5, -0.5 eV	32.96 \pm 0.45
5E-5 $\mu\text{m}^2/\text{min}$, 50 nm, 10, -0.5 eV	52.44 \pm 0.28
5E-5 $\mu\text{m}^2/\text{min}$, 50 nm, 5, -0.5 eV	64.56 \pm 0.40
1E-6 $\mu\text{m}^2/\text{min}$, 100 nm, 10, -0.5 eV	85.94 \pm 0.58
1E-6 $\mu\text{m}^2/\text{min}$, 100 nm, 5, -0.5 eV	102.98 \pm 0.38
1E-6 $\mu\text{m}^2/\text{min}$, 50 nm, 10, -0.1 eV	136.29 \pm 0.25
5E-5 $\mu\text{m}^2/\text{min}$, 100 nm, 10, -0.5 eV	170.61 \pm 0.39
5E-5 $\mu\text{m}^2/\text{min}$, 100 nm, 5, -0.5 eV	204.82 \pm 0.41
1E-6 $\mu\text{m}^2/\text{min}$, 50 nm, 5, -0.1 eV	237.25 \pm 0.56
5E-5 $\mu\text{m}^2/\text{min}$, 50 nm, 10, -0.1 eV	272.41 \pm 0.31
1E-6 $\mu\text{m}^2/\text{min}$, 100 nm, 10, -0.1 eV	332.25 \pm 0.23
5E-5 $\mu\text{m}^2/\text{min}$, 50 nm, 5, -0.1 eV	473.42 \pm 0.45
1E-6 $\mu\text{m}^2/\text{min}$, 100 nm, 5, -0.1 eV	524.87 \pm 0.13
5E-5 $\mu\text{m}^2/\text{min}$, 100 nm, 10, -0.1 eV	665.23 \pm 0.44
5E-5 $\mu\text{m}^2/\text{min}$, 100 nm, 5, -0.1 eV	11050.08 \pm 0.22

Table 4.5. Model Parameter 2⁴ Results –SPE Onset Time

Experiment (D_{HD} , l , N_v^D , ΔE_f^D)	t_0 (Mean \pm Std Err) [min]
1E-6 $\mu\text{m}^2/\text{min}$, 50 nm, 10, -0.5 eV	12.51 \pm 0.45
1E-6 $\mu\text{m}^2/\text{min}$, 50 nm, 5, -0.5 eV	13.87 \pm 0.43
1E-6 $\mu\text{m}^2/\text{min}$, 50 nm, 10, -0.1 eV	21.72 \pm 0.34
5E-5 $\mu\text{m}^2/\text{min}$, 50 nm, 10, -0.5 eV	22.63 \pm 0.29
5E-5 $\mu\text{m}^2/\text{min}$, 50 nm, 5, -0.5 eV	25.13 \pm 0.33
1E-6 $\mu\text{m}^2/\text{min}$, 50 nm, 5, -0.1 eV	25.45 \pm 0.26
1E-6 $\mu\text{m}^2/\text{min}$, 100 nm, 10, -0.5 eV	39.82 \pm 0.44
5E-5 $\mu\text{m}^2/\text{min}$, 50 nm, 10, -0.1 eV	44.05 \pm 0.70
1E-6 $\mu\text{m}^2/\text{min}$, 100 nm, 5, -0.5 eV	44.55 \pm 0.60
5E-5 $\mu\text{m}^2/\text{min}$, 50 nm, 5, -0.1 eV	50.84 \pm 0.46
1E-6 $\mu\text{m}^2/\text{min}$, 100 nm, 10, -0.1 eV	70.40 \pm 0.35
5E-5 $\mu\text{m}^2/\text{min}$, 100 nm, 10, -0.5 eV	78.05 \pm 0.50
1E-6 $\mu\text{m}^2/\text{min}$, 100 nm, 5, -0.1 eV	81.59 \pm 0.41
5E-5 $\mu\text{m}^2/\text{min}$, 100 nm, 5, -0.5 eV	86.42 \pm 0.70
5E-5 $\mu\text{m}^2/\text{min}$, 100 nm, 10, -0.1 eV	140.03 \pm 0.36
5E-5 $\mu\text{m}^2/\text{min}$, 100 nm, 5, -0.1 eV	162.12 \pm 0.33

Table 4.6. Model Parameter 2⁴ Results –Color Center Saturation Time

Experiment (D_{HD} , l , N_v^D , ΔE_f^D)	t_{sat} (Mean \pm Std Err) [min]
1E-6 $\mu\text{m}^2/\text{min}$, 50 nm, 10, -0.5 eV	13.97 \pm 0.45
1E-6 $\mu\text{m}^2/\text{min}$, 50 nm, 5, -0.5 eV	19.09 \pm 0.60
5E-5 $\mu\text{m}^2/\text{min}$, 50 nm, 10, -0.5 eV	29.81 \pm 0.44
5E-5 $\mu\text{m}^2/\text{min}$, 50 nm, 5, -0.5 eV	39.44 \pm 0.60
1E-6 $\mu\text{m}^2/\text{min}$, 100 nm, 10, -0.5 eV	46.12 \pm 0.80
1E-6 $\mu\text{m}^2/\text{min}$, 100 nm, 5, -0.5 eV	58.43 \pm 0.76
5E-5 $\mu\text{m}^2/\text{min}$, 100 nm, 10, -0.5 eV	92.56 \pm 0.73
1E-6 $\mu\text{m}^2/\text{min}$, 50 nm, 10, -0.1 eV	114.56 \pm 0.47
5E-5 $\mu\text{m}^2/\text{min}$, 100 nm, 5, -0.5 eV	118.40 \pm 0.88
1E-6 $\mu\text{m}^2/\text{min}$, 50 nm, 5, -0.1 eV	211.79 \pm 0.46
5E-5 $\mu\text{m}^2/\text{min}$, 50 nm, 10, -0.1 eV	228.36 \pm 0.59
1E-6 $\mu\text{m}^2/\text{min}$, 100 nm, 10, -0.1 eV	262.07 \pm 0.29
5E-5 $\mu\text{m}^2/\text{min}$, 50 nm, 5, -0.1 eV	422.58 \pm 0.56
1E-6 $\mu\text{m}^2/\text{min}$, 100 nm, 5, -0.1 eV	443.29 \pm 0.40
5E-5 $\mu\text{m}^2/\text{min}$, 100 nm, 10, -0.1 eV	525.20 \pm 0.37
5E-5 $\mu\text{m}^2/\text{min}$, 100 nm, 5, -0.1 eV	887.96 \pm 0.36

Table 4.7. Factor Screening Full Model Effects Test for Time of Max SPE Probability $\alpha = 0.05$ significance level

Input Factor or Interaction	Effect Size (F)	p-value
Defect formation energy	3848027	< 0.0001
Damage length	1497734	< 0.0001
Damage diffusion constant	960328	< 0.0001
Damage length \times Defect formation energy	501450	< 0.0001
Damage diffusion constant \times Defect formation energy	429663	< 0.0001
Available vacancy sites	397954	< 0.0001
Available vacancy sites \times Defect formation energy	289418	< 0.0001
Damage diffusion constant \times Damage length	166888	< 0.0001
Damage diffusion constant \times Damage length \times Defect formation energy	56214	< 0.0001
Damage diffusion constant \times Available vacancy sites	43927	< 0.0001
Damage length \times Available vacancy sites	41887	< 0.0001
Damage diffusion constant \times Available vacancy sites \times Defect formation energy	32135	< 0.0001
Damage length \times Available vacancy sites \times Defect formation energy	26010	< 0.0001
Damage diffusion constant \times Damage length \times Available vacancy sites	4772	< 0.0001
Damage diffusion constant \times Damage length \times Available vacancy sites \times Defect formation energy	2889	< 0.0001

Table 4.8. Factor Screening Full Model Effects Test for SPE Onset Time $\alpha = 0.05$ significance level

Input Factor or Interaction	Effect Size (F)	p-value
Damage length	72271	< 0.0001
Damage diffusion constant	27329	< 0.0001
Defect formation energy	22771	< 0.0001
Damage diffusion constant \times Damage length	7922	< 0.0001
Damage length \times Defect formation energy	5754	< 0.0001
Damage diffusion constant \times Defect formation energy	2834	< 0.0001
Available vacancy sites	1126	< 0.0001
Damage diffusion constant \times Damage length \times Defect formation energy	583	< 0.0001
Damage length \times Available vacancy sites	312	< 0.0001
Available vacancy sites \times Defect formation energy	220	< 0.0001
Damage diffusion constant \times Available vacancy sites	107	< 0.0001
Damage length \times Available vacancy sites \times Defect formation energy	56	< 0.0001
Damage diffusion constant \times Damage length \times Available vacancy sites	33	< 0.0001
Damage length \times Available vacancy sites \times Defect formation energy	26	< 0.0001
Damage diffusion constant \times Damage length \times Available vacancy sites \times Defect formation energy	9	0.0036

Table 4.9. Factor Screening Full Model Effects Test for Color Center Saturation Time $\alpha = 0.05$ significance level

Input Factor or Interaction	Effect Size (F)	p-value
Defect formation energy	1363530	< 0.0001
Damage length	348782	< 0.0001
Damage diffusion constant	262489	< 0.0001
Damage length \times Defect formation energy	163738	< 0.0001
Damage diffusion constant \times Defect formation energy	150519	< 0.0001
Available vacancy sites	150034	< 0.0001
Available vacancy sites \times Defect formation energy	116424	< 0.0001
Damage diffusion constant \times Damage length	39092	< 0.0001
Damage diffusion constant \times Damage length \times Defect formation energy	18625	< 0.0001
Damage diffusion constant \times Available vacancy sites	16722	< 0.0001
Damage length \times Available vacancy sites	14476	< 0.0001
Damage diffusion constant \times Available vacancy sites \times Defect formation energy	12903	< 0.0001
Damage length \times Available vacancy sites \times Defect formation energy	9980	< 0.0001
Damage diffusion constant \times Damage length \times Available vacancy sites	1665	< 0.0001
Damage diffusion constant \times Damage length \times Available vacancy sites \times Defect formation energy	1084	< 0.0001

Ab-initio Results

In order to emulate experimental process of FIB followed by CVD, DFT-based calculations were used to determine an upper estimate of defect formation energies for a representative set of carbon-based defect complexes, which consist of substitutional carbons adjacent to different vacancies. **Figure 4.8(a)** gives the formation energy of these defect complexes using two reference structures – pristine hBN and defective hBN with vacancies already present within the matrix. As seen in the histogram, the formation energy of carbon-containing defect complexes is much larger in pristine hBN than the energies required to incorporate carbon once vacancies have already been created in hBN. Additionally, the reported formation energies for carbon-containing defect complexes in defective hBN are consistent with the estimations for defect formation energy used in the color center yield calculations reported in **Figures 4.3-4.4** and **Table 4.3**.

Figure 4.8(b) and **(c)**, for $V_B C_N$ and $V_N C_B$ defects, respectively, show the ranges of electronic chemical potential (Fermi level) over which their different charge states are stable. **Figure 4.8(b)** shows that the three most favorable charge states for $V_B C_N$ are 0, -1 and -2, out of which only first two are spin active, with spins of 1 and $\frac{1}{2}$, respectively and so, this defect might not be the one observed by Mendelson et. al in experiment. Also, according to our DFT calculations, the neutral $V_N C_B$ is not spin active, with the non-magnetic solution being the lower energy state, which was missed by earlier works⁹⁴. Amongst the energetically most favorable charge states (+2, +1 and 0) shown in **Figure 4.8(c)**, only +1 charge state is spin-active and has a spin-1/2, which was also reported previously⁹⁵.

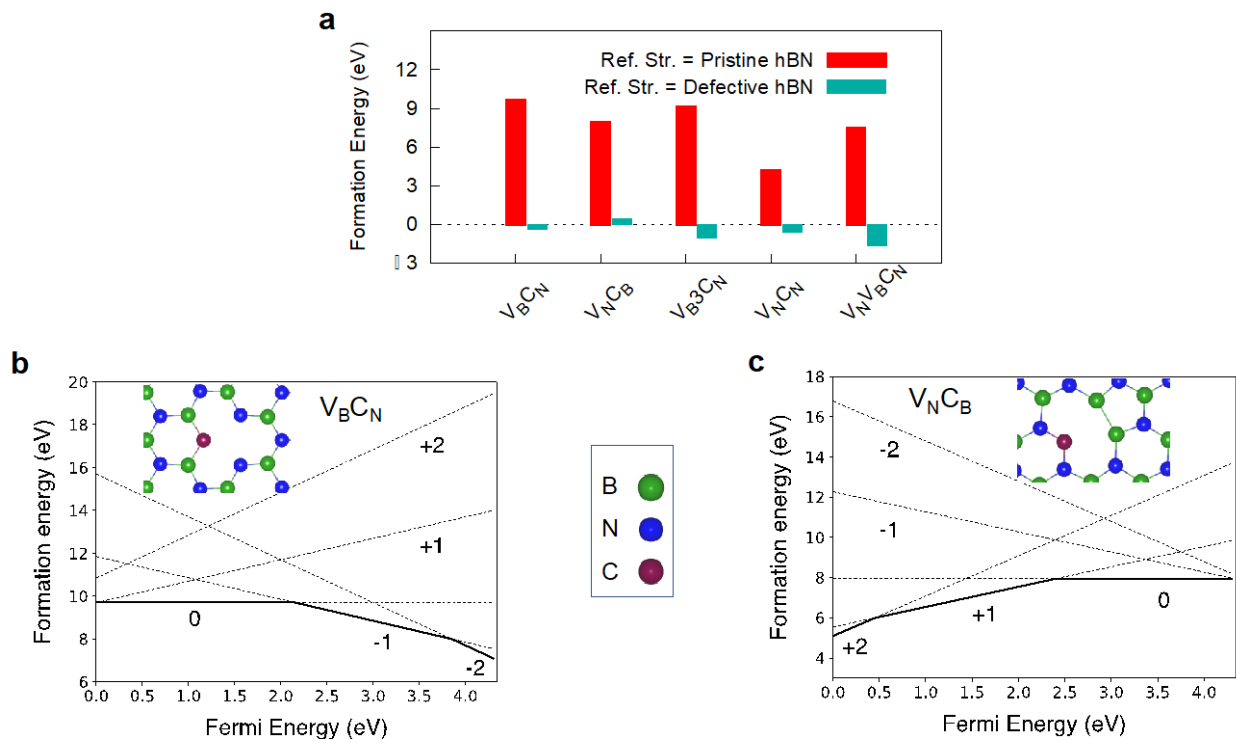


Figure 4.8. Density functional theory (DFT) calculations. (a) Defect formation energies for a representative set of defect complexes consisting of carbon, with two different starting reference structures (abbreviated as Ref. Str.). For sake of comparison, all defect formation energies are calculated for boron-rich conditions. The large reduction in formation energies of carbon-based defects if the vacancies are already present in the hBN matrix (say, introduced via FIB method) as compared to creating these complexes in pristine hBN corroborate the experimental results. (b) Defect formation energy for V_{BCN} defect as a function of electronic chemical potential (Fermi energy). Fermi energy is measured relative to the VBM. The solid line indicates the most stable charge states for a given electronic chemical potential, showing that this defect prefers a charge state of 0, -1 and -2, depending on the Fermi energy. The ball and stick model in the inset shows the equilibrium geometry of the defect in the neutral state. (c) Defect formation energy for V_{NCB} defect as a function of Fermi energy, showing the preferred charge states for any given Fermi level. Only +1 charge state of V_{NCB} is spin active (spin-1/2). The inset shows the equilibrium geometry of the defect in the neutral state, wherein the weak boron-boron bond between the boron atoms surrounding the defect result in a structure without any local magnetic moment.

CHAPTER V

CONCLUDING REMARKS

The primary work in this dissertation to pattern and characterize quantum emitters in 2D insulator hBN makes device integration for quantum information technologies more straightforward and adjustable. We first achieve this via repeatable success of SPE creation by FIB patterning and carbon annealing at multiple parameter combination values with control over ZPL and purity as reported in Chapter II. Additionally, by elucidating a physical mechanism for the defect formation process via AFM characterization in Chapter III and modeling in Chapter IV, we provide an avenue to better control the optimization of color center creation and photophysical properties.

This technique increases the utility of room temperature carbon-based hBN SPEs in photonic nanostructures such as resonant cavities, optomechanical transducers, and magnetic quantum sensors by allowing pick-and-place emitter integration rather than relying on multi-step alignment or scaffolding processes. Furthermore, our analysis and modeling improve this utility by characterizing the effects of FIB exposure and carbon annealing on emitter yields and properties so that future applications of this technique can mitigate undesired damage, reduce diffusion source byproducts, and control the size and type of defects. The increased level of control over SPE creation possible due to this work can be used to improve the stability and indistinguishability of hBN emitters, which are requirements for quantum applications.

Beyond hBN, many solid-state emission sources based on extrinsic defects benefit from adjustable patterning techniques. Color centers in three-dimensional wide bandgap materials

such as diamond, GaN, and SiC as well as defect-induced exciton transitions in 2D transition metal dichalcogenides (TMDCs) all depend on the controlled introduction of impurities to form defect complexes^{8,45}, but current fabrication techniques either rely on niche implantation systems or need multi-step photolithography processes to localize emitters, and sometimes both. The general technique presented in this work depends only on the ability to first open a diffusion window and create vacancies via FIB, then introduce the impurity dopant via CVD or annealing, using equipment and resources more commonly found in standard fabrication facilities. Although other single photon sources are based on different extrinsic defect complexes (e.g. NV in diamond, $V_{Si}V_C$ in 4H-SiC¹⁰⁴, Cr_w in WS₂¹⁰⁵), adjusting the dopant feedstock gas or evaporating a precursor upstream can provide control over impurity sources and concentrations, while adjusting FIB patterning parameters can control the available vacancy concentration and the introduction of impurities via a high damage diffusion barrier. Applying this technique broadly to pattern solid-state single photon emitters can enable widespread emitter integration for quantum photonics and sensors that have unique advantages.

These results provide a scalable technique to create solid-state single photon sources in materials beyond hBN with low native defect densities, allowing exposure dose, impurity species, and diffusion time to be chosen based on system requirements and fabrication constraints. This fabrication and modeling framework can be used to design and integrate monolithic and hybrid quantum systems that rely on coupling single photons in quantum information technologies for transduction, communication, and sensing with more readily accessible resources and more time efficient engineering and optimization.

APPENDICES

APPENDIX A

CORRELATIVE SCANNING NEAR-FIELD OPTICAL FLUORESCENCE AND TOPOGRAPHY OF HBN COLOR CENTERS

This appendix summarizes preliminary results obtained during my work on the WITec alpha 3000 Correlative Scanning Near-Field Optical Microscope (SNOM) housed in the Center for Advanced Materials Characterization in Oregon (CAMCOR) Surface Analytic Facility in order to adapt it for fluorescence measurements. These results were previously reported at the Oregon Center for Optical, Molecular, and Quantum Science (OMQ) Fall 2019 Symposium via poster presentation.

Techniques to engineer quantum emitters (QEs) in deterministic locations in solid-state hosts such as the 2D material hexagonal boron nitride (hBN) rely on ion irradiation or focused ion beam (FIB) patterning that can damage the material surface while creating the desired vacancy or implantation defects. Damage to the material and substrate can produce local strain gradients and charge traps, which can ultimately lead to variation and instabilities in the zero-phonon line (ZPL) energy, fluorescence intensity, and quantum purity. Current techniques to characterize emitters and correlate material damage are limited by optical localization capabilities (i.e. the diffraction limit) and alignment calibrations when transferring samples between optical and topographical characterization tools. It would therefore be advantageous to

develop a technique to simultaneously characterize optical properties of emitters and the local topography of the host material at the defect location with resolutions beyond the diffraction limit.

We leveraged the high-resolution imaging technique of scanning near-field optical fluorescence microscopy (SNOM-f) to investigate the location and correlated topography of activated emitters to elucidate intrinsic strain dependences on QE formation. In order to only collect off-resonant fluorescent color centers, we adapted the WITec alpha 3000 Correlative SNOM transmission collection optics by adding a 532 nm notch filter and 550 nm longpass filter [Figure A.1]. In this particular instrument, a 532 nm excitation laser is focused into a hollow cantilever with 100 nm aperture. The cantilever utilizes AFM feedback principles to maintain a sub-wavelength contact distance from the sample during a scan. The evanescent waves transmitted through the cantilever aperture are within near-field distance of defects to excite, thereby beating the diffraction limit.

We tested the resolution of SNOM-f by characterizing the same region of an exfoliated hBN flake first in a home-built confocal microscope and then in the SNOM. We found that our SNOM-f technique improved the resolution by a factor of 2 [Figure A.2]. For the region labeled Spot 1, we were able to resolve two distinct color centers from the SNOM-f scan, while there was only one present in the corresponding confocal scan. We expect that this indicated there were multiple defect-based color centers present in the same localized region that were unable to be resolved via traditional confocal characterization.

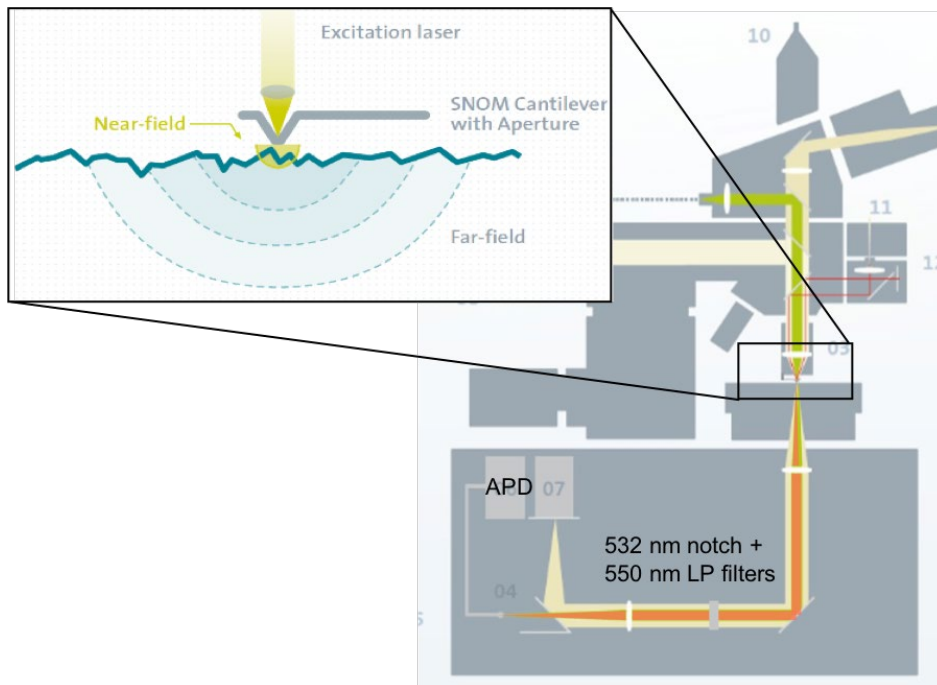


Figure A.1. Schematic of WITec SNOM adapted for fluorescence (Inset) SNOM principles

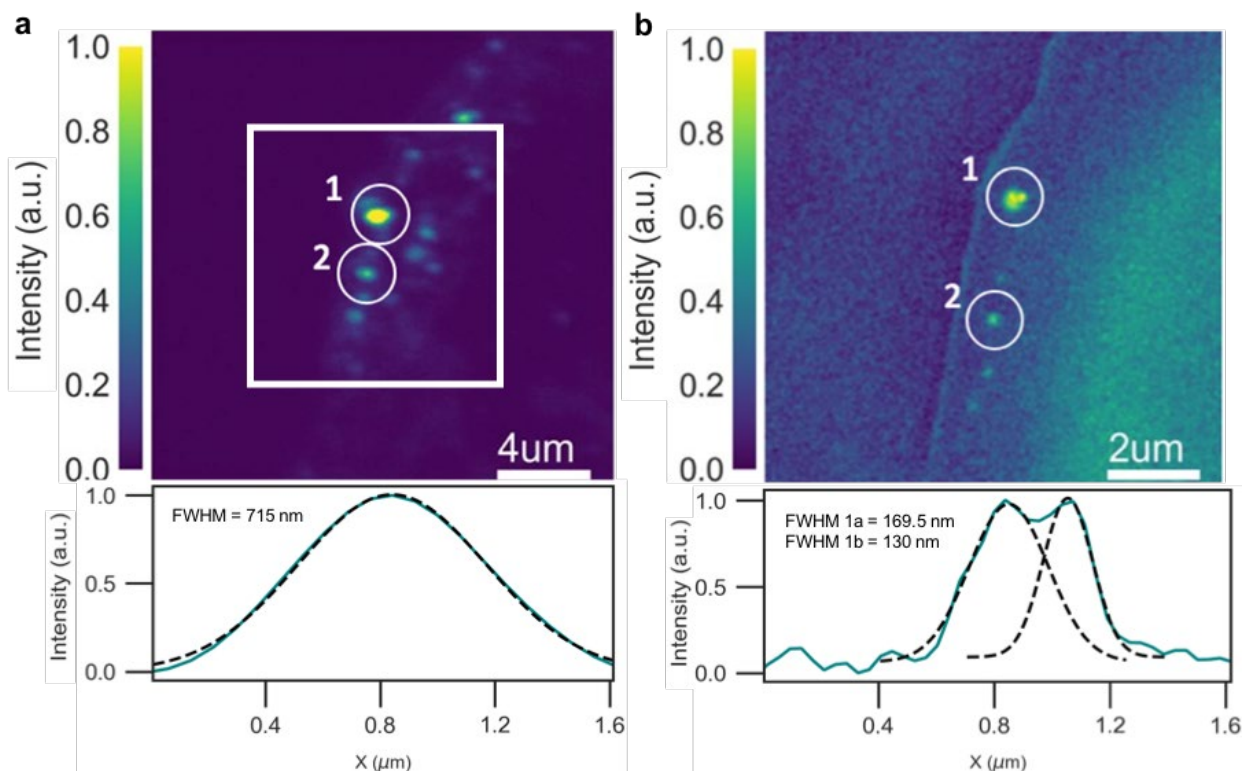


Figure A.2. Improving confocal resolution with SNOM (a) Confocal PL scan of exfoliated hBN flake and corresponding intensity line cut for spot 1 (b) SNOM-f scan of the boxed area and corresponding intensity line cut for spot 1

During optical collection, we obtained simultaneous AFM height topography data as shown in **Figure A.3**. We observed surface features in locations that corresponded to the fluorescent locations, which could indicate that the color centers are either strain activated or were due to some other fluorescent feature on the surface of hBN and not from defects within the hBN itself.

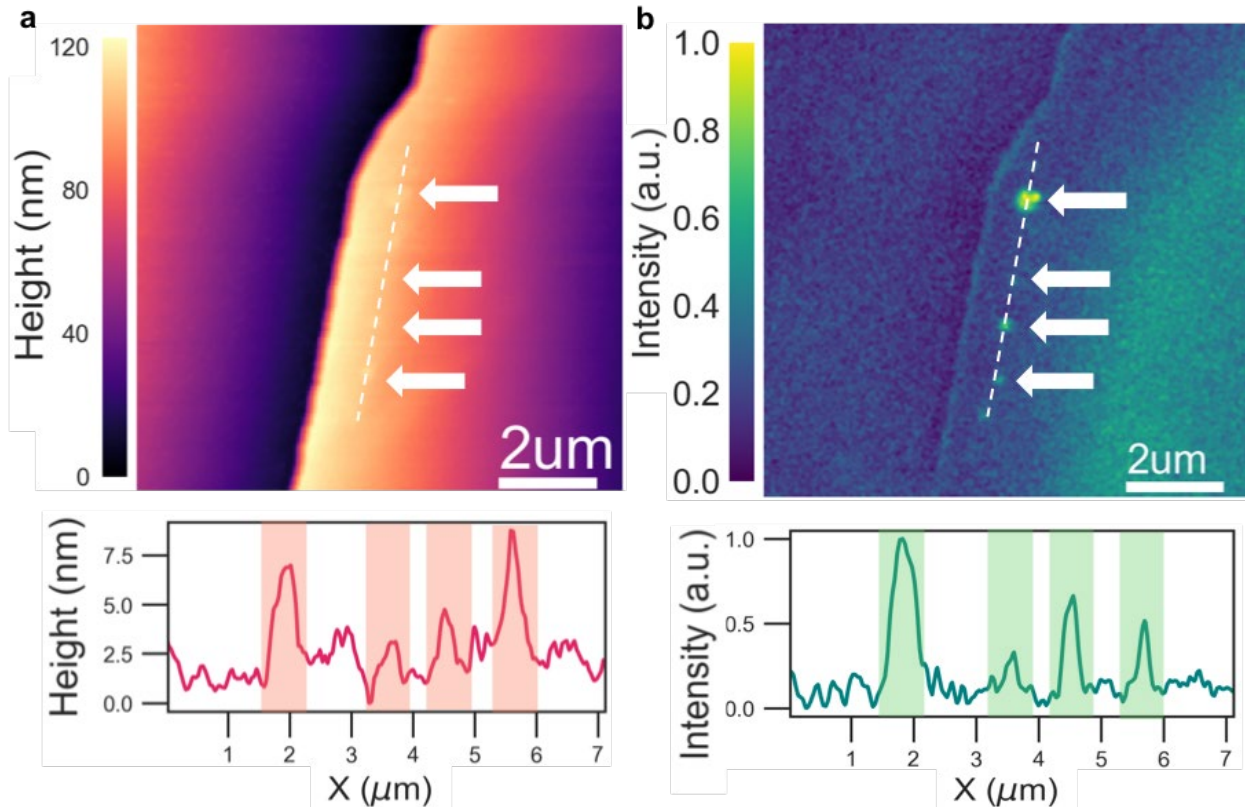


Figure A.3. Simultaneous correlation of hBN color center SNOM fluorescence to AFM height topography (a) AFM height scan and corresponding line cut of marked area (b) SNOM-f scan of the same area taken simultaneously and corresponding intensity line cut on the same line. Highlighted areas and areas on all images correspond to correlated points

To determine if the observed correlations between AFM topography and SNOM fluorescence were due to material dependent defects or were some other imaging artefact, we characterized another sample and identified one of the color centers as a QE [**Figure A.4**]. In particular, the highlighted defect appeared on a flake edge in a folded region, supporting previous work that observed that hBN SPEs prefer to form at edges. Furthermore, the folded area

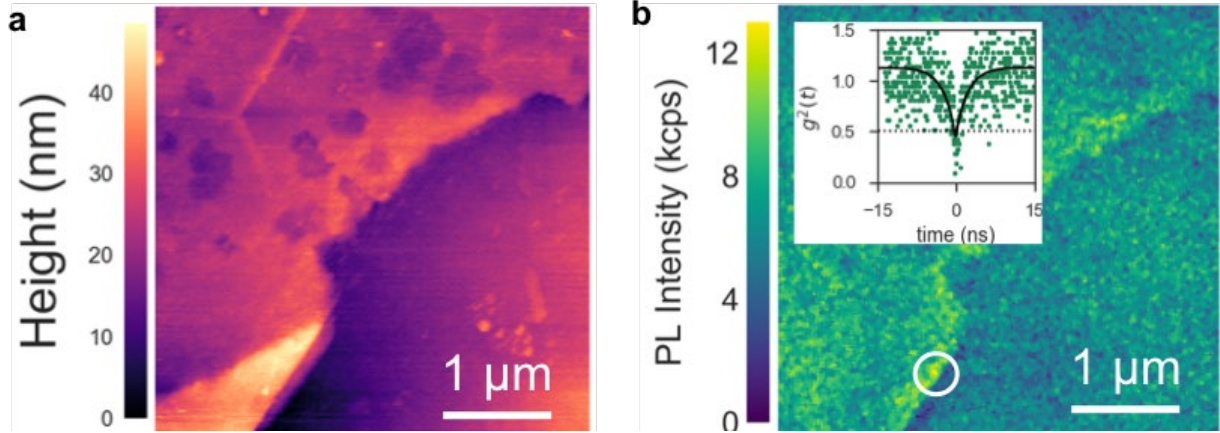


Figure A.4. Correlative imaging of an hBN quantum emitter (a) SNOM fluorescence image of exfoliated hBN with SPE circled (b) AFM topography image taken simultaneously (Inset) Antibunching dip of the emitter circled in (a) with $g^2(0) < 0.5$ characteristic of SPEs

may have introduced further local strain or confinement that allowed this color center to be an isolated SPE.

Acquiring SNOM data on many SPEs could help answer questions about why SPEs tend to form at edges or near grain boundaries, which may be a result of intrinsic strain gradients created by deformations in the material. This technique could be used in future work to identify where SPEs tend to form and potential intrinsic strain, as the tunable range of hBN SPEs depends on intrinsic strain.¹⁰⁶ By understanding under which conditions SPEs prefer to form, we can further tailor our milling parameters.

APPENDIX B

SAMPLE IMAGES

This appendix contains optical microscope, scanning electron microscope, and confocal photoluminescence images of the samples characterized for this dissertation.

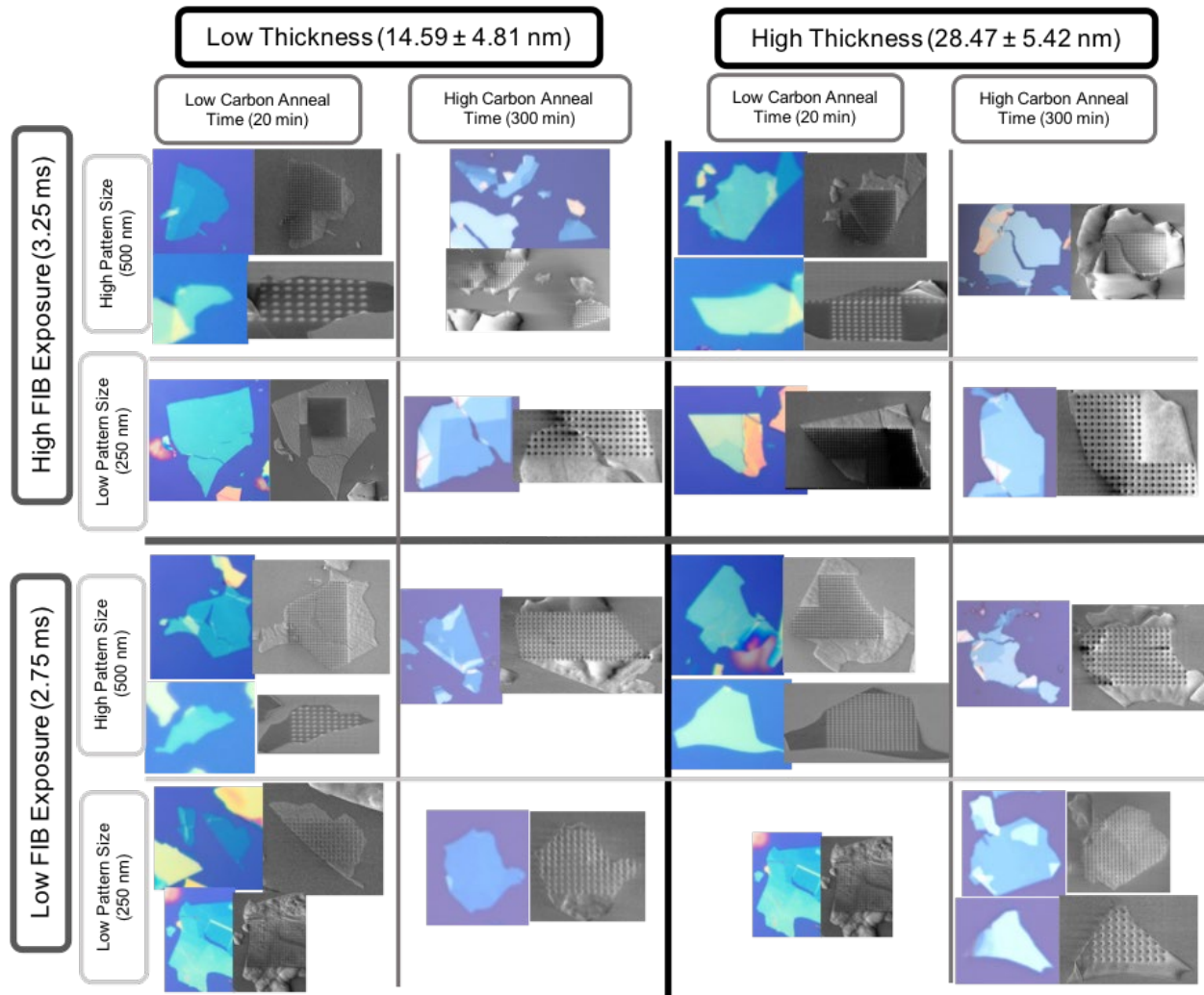


Figure B.1. Optical and SEM of factor screening samples

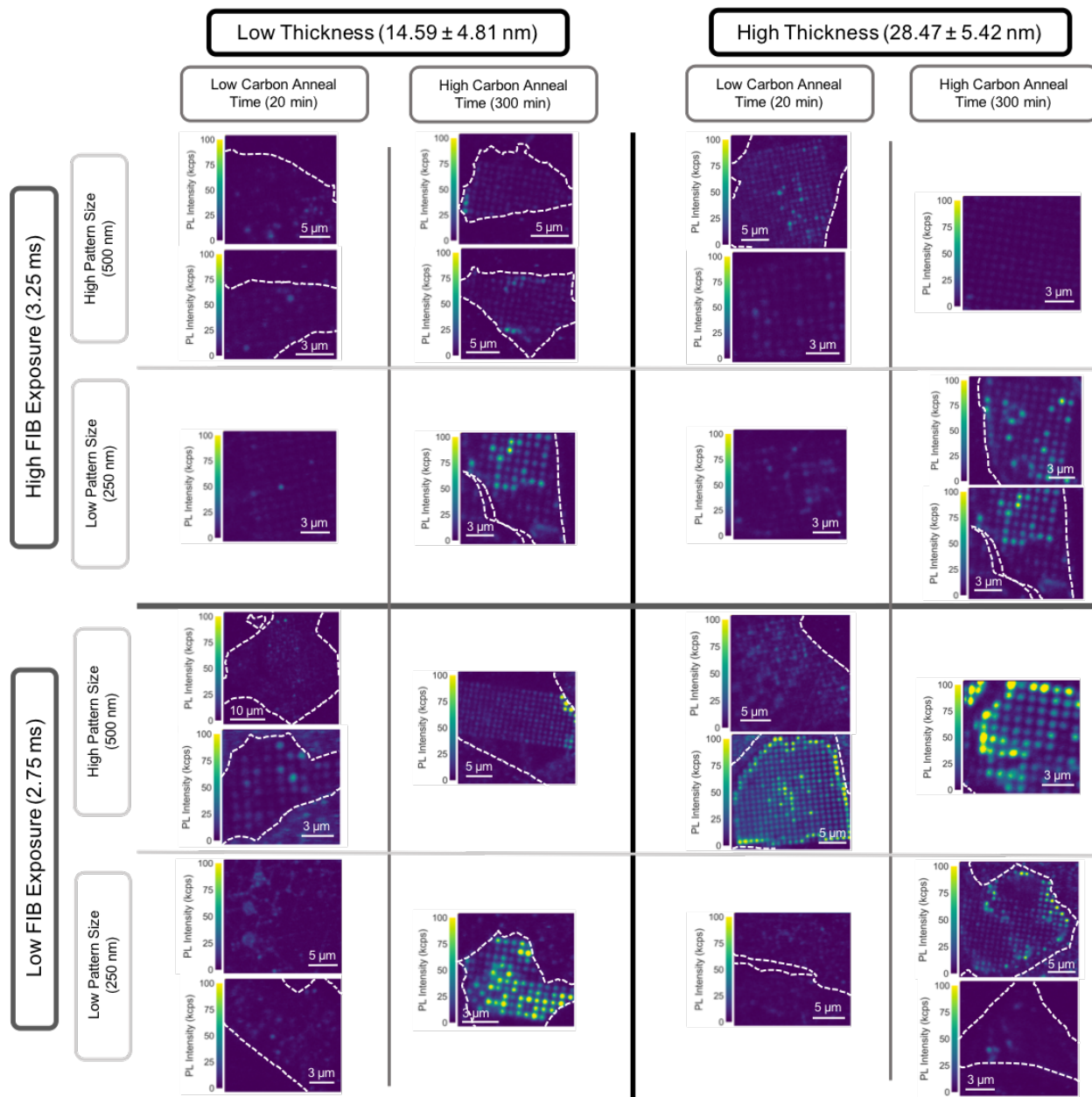


Figure B.2. Confocal PL scans of factor screening samples

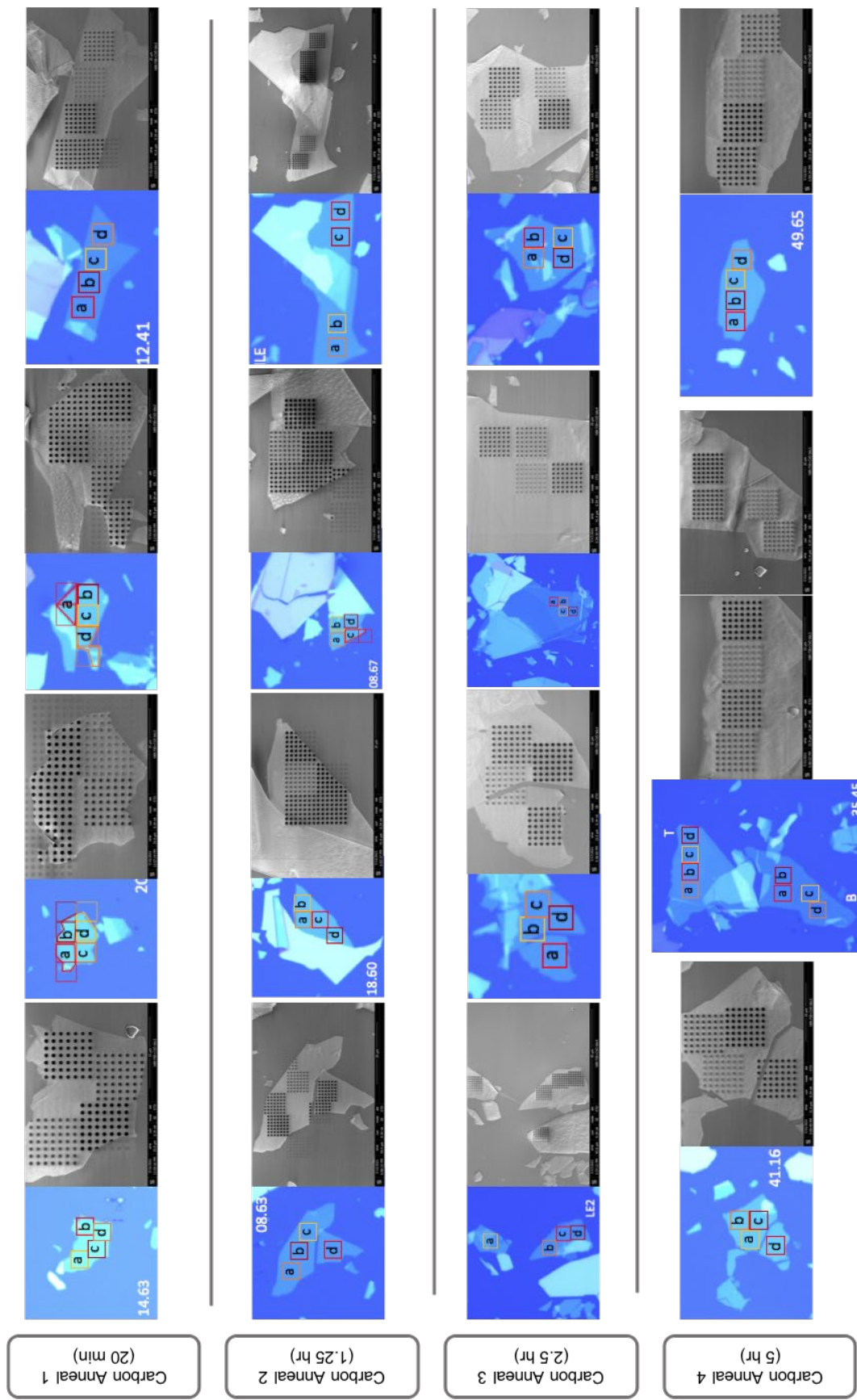


Figure B.3. Optical and SEM of optimization samples

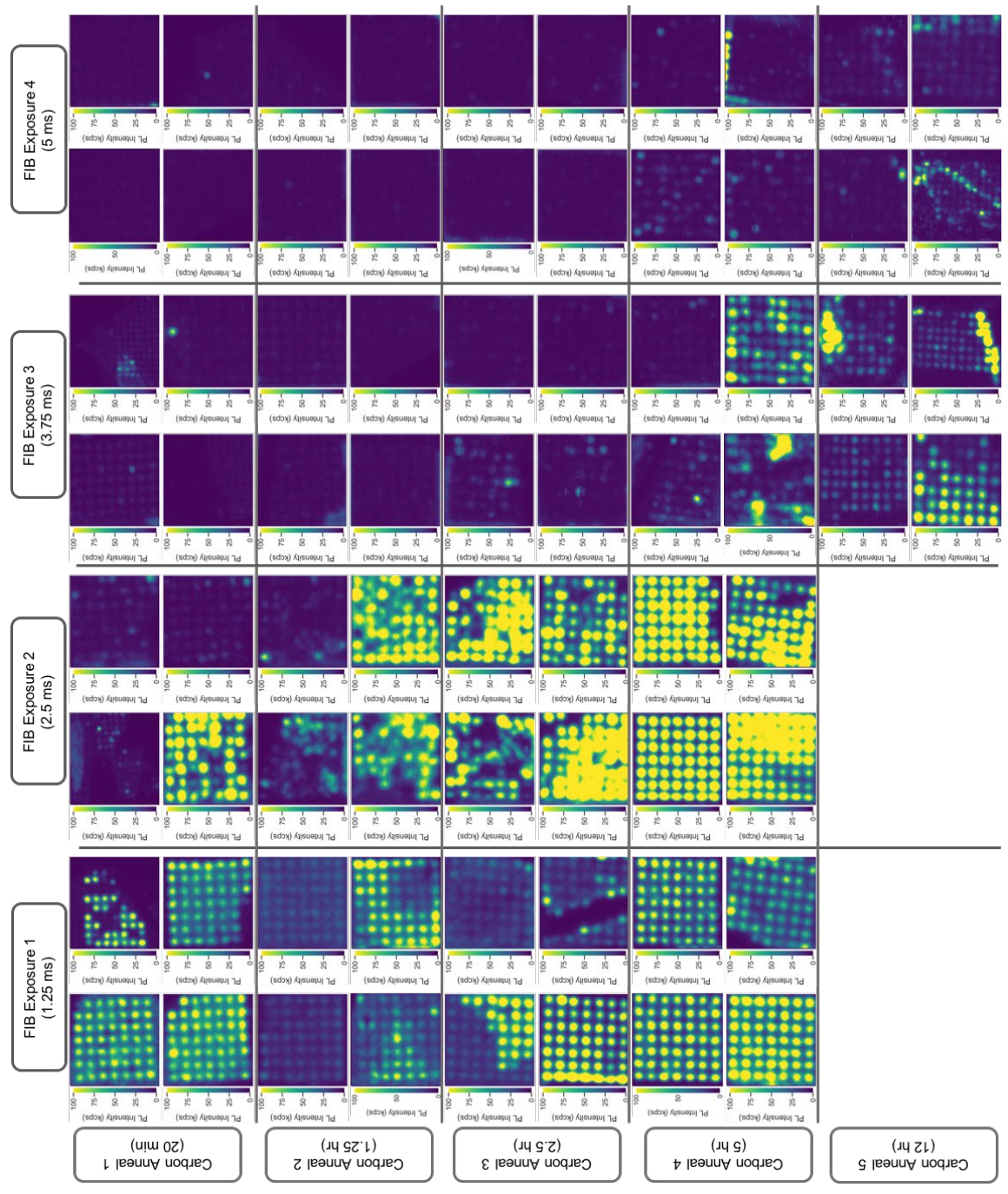


Figure B.4. Confocal PL of optimization samples

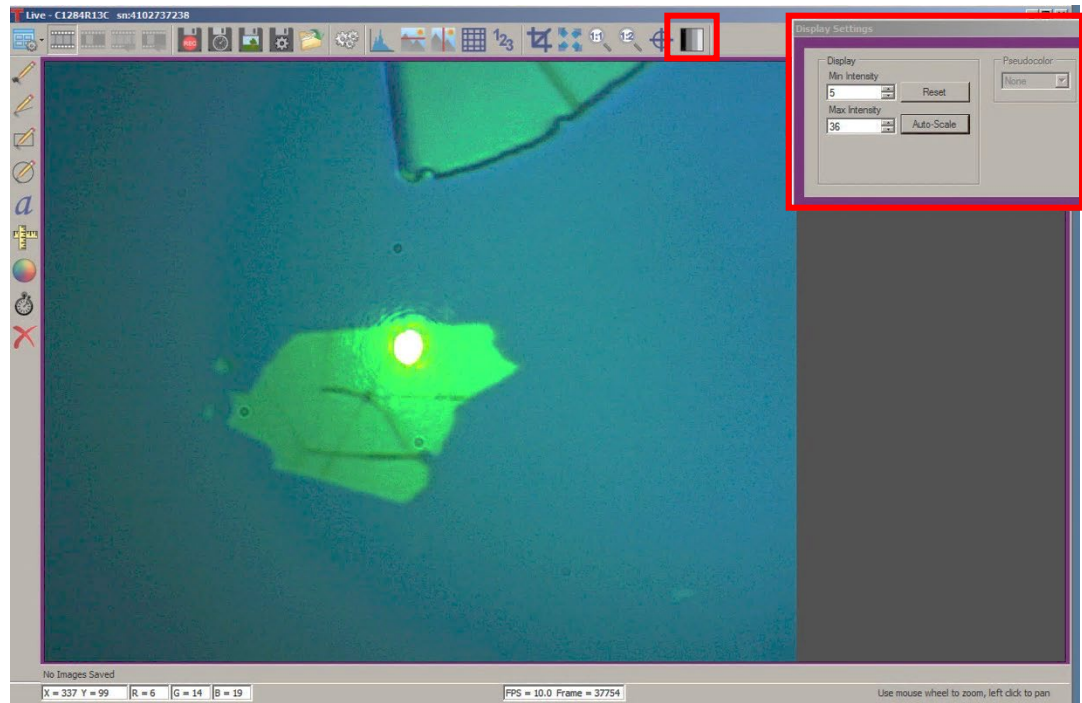
APPENDIX C

HOME-BUILT CONFOCAL MICROSCOPE USE INSTRUCTIONS

This appendix outlines the steps to operate the home-built confocal microscope in the Alemán lab used to collect data for this dissertation.

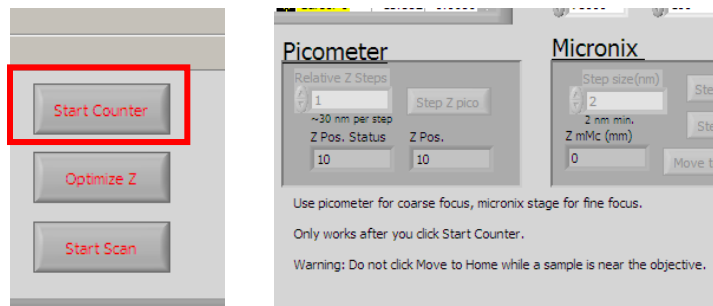
Confocal Scan

- Load Sample
 - Use a **thin** strip of double sided capton tape to adhere sample chip to glass microscope slide
 - Place microscope slide on sample stage by sliding under clips
- Make sure flip mirror is flipped down so that light is collected by camera
- Turn on camera lamp (red box)
- Turn on Laser (black box)
 - Flip switch on back of box
 - Wait until red light turns on, the turn key to horizontal orientation
 - Make sure ND filter is in the range **4.1-4.6**
- Adjust position and focus knobs until you can see the light reflect off the sample by eye
- Open **ThorCam Live** recording on computer



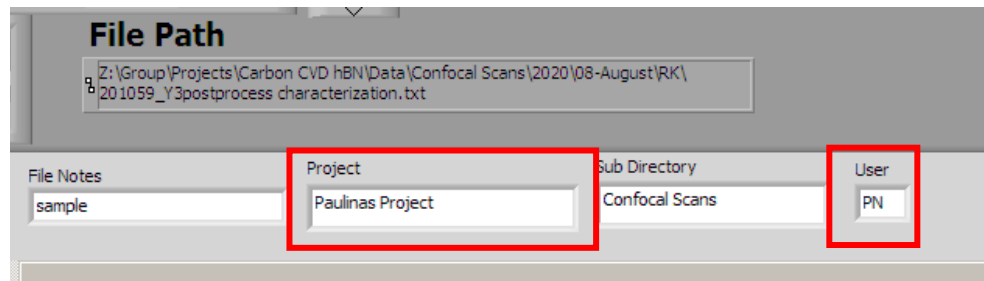
-
- If sample is not visible (typically blue even if unfocused), **Auto-Scale** Display Settings

- Course focus by hand until laser spot is small and round
- Find desired measurement location, adjusting focus along the way
- To fine focus:
 - Make sure APD power supply strip is **OFF**
 - On **Confocal 2** LabVIEW program click **Start Counter**

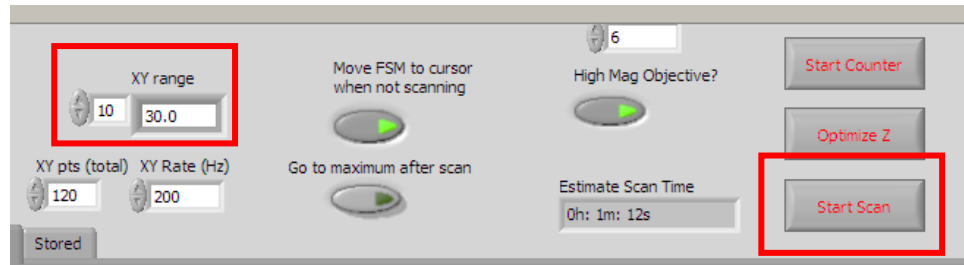


-
- Use **Picometer** on step size + or – 1 to “**Step Z pico**” (move the stage by small amounts), while watching the ThorCam for best focus

- When ready to start Confocal Scan (**must be done in order**):
 - Turn off camera lamp (red box)
 - Push button to flip mirror up (so light goes to collection optics)
 - Change ND filter to **1.6**
 - If taking many measurements over multiple days, measure power output and adjust filter to keep constant excitation power
 - Turn off room lights
 - Decrease computer brightness
 - Right click LED display on bottom task bar (it looks like a blue computer screen)
 - Click **Configure**
 - Slide scale bar to 95%
 - Turn on APD power strip
 - Open up **TimeHarp** software
 - Watch **sync/cps** and **input/cps** count numbers. The APDs are ready once the count numbers flip back to 0 and then show counts again
- Change file location to correct project folder with user initials



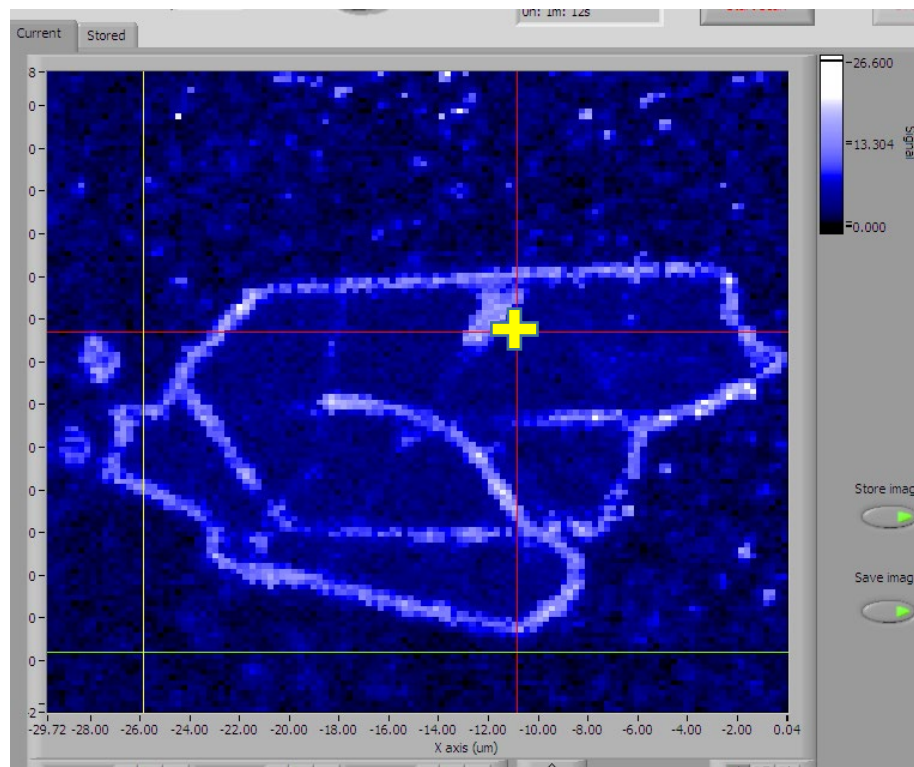
-
- Set scan size by scrolling through pre-set XY sizes (in microns)



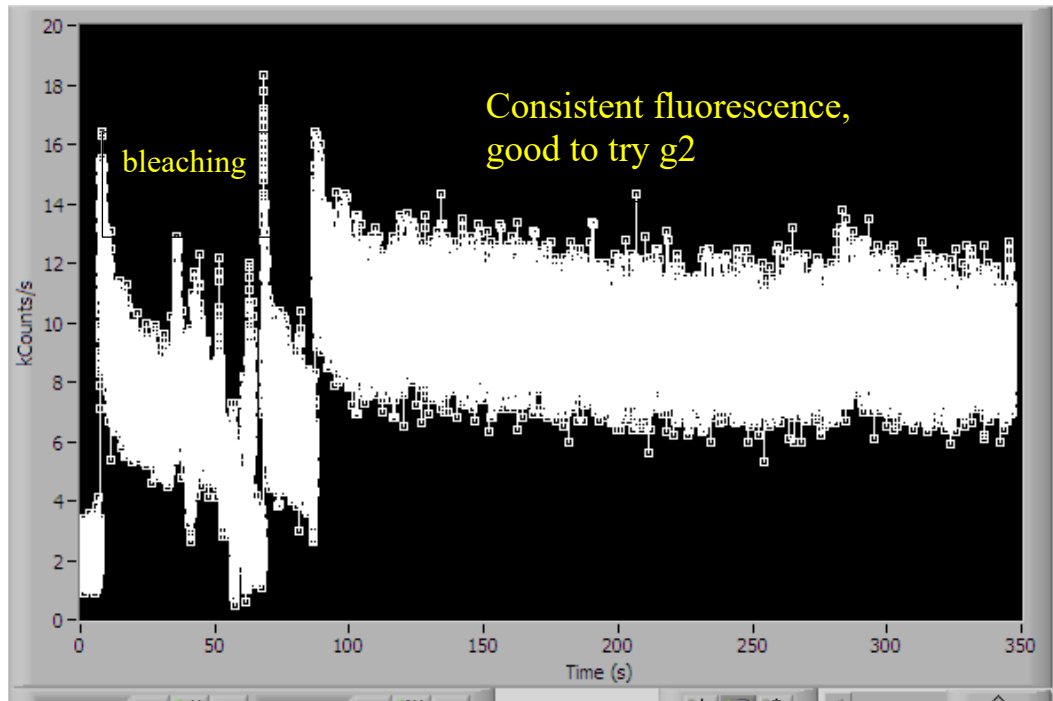
- **Start Scan**

Photon Counting [$g^2(t)$] measurements

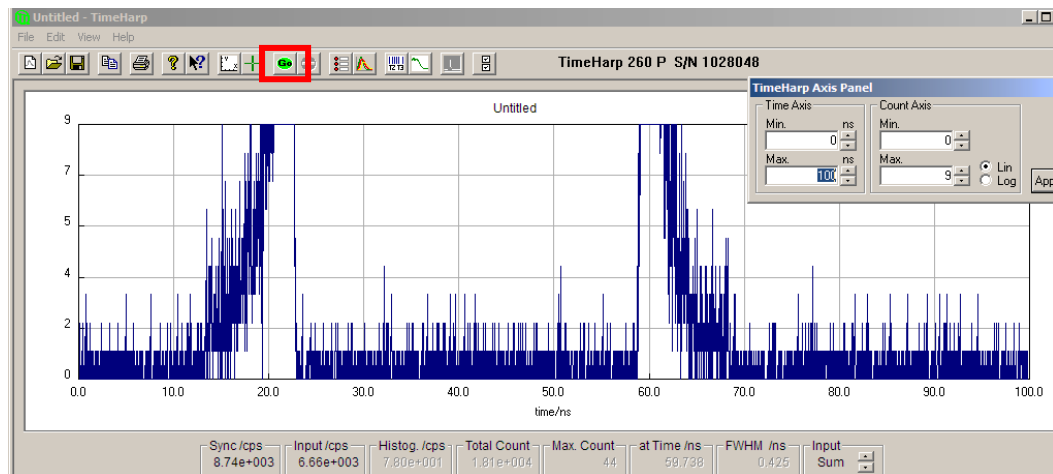
- When Confocal Scan is completed, turn off monitor and move to **Remote Desktop**
- click **Start Counter**
- Drag center cursor over bright spots



- Hover for ~30 seconds to see if signal attenuates or if there is consistent fluorescence



- Open **TimeHarp** software
- Click **GO**



REFERENCES CITED

1. Kimble, H. J. The quantum internet. *Nature* **453**, 1023–1030 (2008).
2. Wang, Y., Li, J., Zhang, S., Su, K., Zhou, Y., Liao, K., Du, S., Yan, H. & Zhu, S. L. Efficient quantum memory for single-photon polarization qubits. *Nat. Photonics* **13**, 346–351 (2019).
3. Schell, A. W., Takashima, H., Tran, T. T., Aharonovich, I. & Takeuchi, S. Coupling Quantum Emitters in 2D Materials with Tapered Fibers. *ACS Photonics* **4**, 761–767 (2017).
4. Gao, X., Yin, Z.-Q. & Li, T. High-Speed Quantum Transducer with a Single-Photon Emitter in a 2D Resonator. *Ann. Phys.* **532**, 2000233 (2020).
5. Hollenbach, M., Berencén, Y., Kentsch, U., Helm, M. & Astakhov, G. V. Engineering telecom single-photon emitters in silicon for scalable quantum photonics. *Opt. Express* **28**, 26111 (2020).
6. Durand, A., Baron, Y., Redjem, W., Herzig, T., Benali, A., Pezzagna, S., Meijer, J., Kuznetsov, A. Y., Gérard, J. M., Robert-Philip, I., Abbarchi, M., Jacques, V., Cassabois, G. & Dréau, A. Broad Diversity of Near-Infrared Single-Photon Emitters in Silicon. *Phys. Rev. Lett.* **126**, 083602 (2021).
7. Prabhu, M., Errando-Herranz, C., De Santis, L., Christen, I., Chen, C., Gerlach, C. & Englund, D. Individually addressable and spectrally programmable artificial atoms in silicon photonics. *Nat. Commun.* **14**, 2380 (2023).
8. Moody, G., Sorger, V. J., Blumenthal, D. J., Juodawlkis, P. W., Loh, W., Sorace-agaskar, C., Jones, A. E., Balram, K. C., Matthews, J. C. F., Laing, A., Davanco, M., Chang, L., Bowers, J. E., Quack, N., Galland, C., Aharonovich, I., Wolff, M. A., Schuck, C., Sinclair, N., Lon, M., Komljenovic, T., Weld, D., Mookherjea, S., Buckley, S., Radulaski, M., Reitzenstein, S., Pingault, B., Machielse, B. & Mukhopadhyay, D. 2022 Roadmap on integrated quantum photonics. *J. Phys. Photonics* **4**, 012501 (2022).
9. Kaur, P., Boes, A., Ren, G., Nguyen, T. G., Roelkens, G. & Mitchell, A. Hybrid and heterogeneous photonic integration. *APL Photonics* **6**, 061102 (2021).
10. Yeo, I., De Assis, P. L., Gloppe, A., Dupont-Ferrier, E., Verlot, P., Malik, N. S., Dupuy, E., Claudon, J., Gérard, J. M., Auffèves, A., Nogues, G., Seidelin, S., Poizat, J. P., Arcizet, O. & Richard, M. Strain-mediated coupling in a quantum dot-mechanical oscillator hybrid system. *Nat. Nanotechnol.* **9**, 106–110 (2014).
11. Golter, D. A., Oo, T., Amezcua, M., Stewart, K. A. & Wang, H. Optomechanical Quantum Control of a Nitrogen-Vacancy Center in Diamond. *Phys. Rev. Lett.* **116**, 143602 (2016).

12. Lee, K. W., Lee, D., Ovarthaiyapong, P., Minguzzi, J., Maze, J. R. & Bleszynski Jayich, A. C. Strain Coupling of a Mechanical Resonator to a Single Quantum Emitter in Diamond. *Phys. Rev. Appl.* **6**, 034005 (2016).
13. Castellanos-Gomez, A., Singh, V., Van Der Zant, H. S. J. & Steele, G. A. Mechanics of freely-suspended ultrathin layered materials. *Ann. Phys.* **527**, 27–44 (2015).
14. Tran, T. T., Bray, K., Ford, M. J., Toth, M. & Aharonovich, I. Quantum emission from hexagonal boron nitride monolayers. *Nat. Nanotechnol.* **11**, 37–41 (2015).
15. Tran, T. T., Elbadawi, C., Totonjian, D., Lobo, C. J., Grosso, G., Moon, H., Englund, D. R., Ford, M. J., Aharonovich, I. & Toth, M. Robust Multicolor Single Photon Emission from Point Defects in Hexagonal Boron Nitride. *ACS Nano* **10**, 7331–7338 (2016).
16. Kianinia, M., Regan, B., Tawfik, S. A., Tran, T. T., Ford, M. J., Aharonovich, I. & Toth, M. Robust Solid-State Quantum System Operating at 800 K. *ACS Photonics* **4**, 768–773 (2017).
17. Proscia, N. V., Hotan, Z. A. V. S., Ayakumar, H. A. J., Eddy, P. R. R., Ohen, C. H. C., Ollar, M. I. D., Lkauskas, A. U. A., Oherthy, M. A. D., Eriles, C. A. A. M. & Enon, V. I. M. M. Near-deterministic activation of room-temperature quantum emitters in hexagonal boron nitride. *Optica* **5**, 1128–1134 (2018).
18. Mendelson, N., Xu, Z. Q., Tran, T. T., Kianinia, M., Scott, J., Bradac, C., Aharonovich, I. & Toth, M. Engineering and Tuning of Quantum Emitters in Few-Layer Hexagonal Boron Nitride. *ACS Nano* **13**, 3132–3140 (2019).
19. Tawfik, S. A., Ali, S., Fronzi, M., Kianinia, M., Tran, T. T., Stampfl, C., Aharonovich, I., Toth, M. & Ford, M. J. First-principles investigation of quantum emission from hBN defects. *Nanoscale* **9**, 13575–13582 (2017).
20. Kozawa, D., Li, S. X., Ichihara, T., Rajan, A. G., Gong, X., He, G., Koman, V. B., Zeng, Y., Kuehne, M., Silmore, K. S., Parviz, D., Liu, P., Liu, A. T., Faucher, S., Yuan, Z., Warner, J., Blankschtein, D. & Strano, M. S. Discretized hexagonal boron nitride quantum emitters and their chemical interconversion. *Nanotechnology* **34**, 115702 (2023).
21. Narayanan, S. K. & Dev, P. Substrate-Induced Modulation of Quantum Emitter Properties in 2D Hexagonal Boron Nitride: Implications for Defect-Based Single Photon Sources in 2D Layers. *ACS Appl. Nano Mater.* **6**, 3446–3452 (2023).
22. Pelini, T., Waselowski, V., Maze, J. R., Gil, B., Cassabois, G. & Jacques, V. Efficient single photon emission from a high-purity hexagonal boron nitride crystal. **121405**, 1–5 (2016).
23. Ziegler, J., Klaiss, R., Blaikie, A., Miller, D., Horowitz, V. R. & Alemán, B. J. Deterministic Quantum Emitter Formation in Hexagonal Boron Nitride via Controlled Edge Creation. *Nano Lett.* **19**, 2121–2127 (2019).

24. Stern, H. L., Wang, R., Fan, Y., Mizuta, R., Stewart, J. C., Needham, L., Roberts, T. D., Wai, R., Ginsberg, N. S., Klenerman, D., Hofmann, S. & Lee, S. F. Spectrally Resolved Photodynamics of Individual Emitters in Large-Area Monolayers of Hexagonal Boron Nitride. *ACS Nano* **13**, 4538–4547 (2019).
25. Duong, N. M. H., Nguyen, M. A. P., Kianinia, M., Ohshima, T., Abe, H., Watanabe, K., Taniguchi, T., Edgar, J. H., Aharonovich, I. & Toth, M. Effects of High-Energy Electron Irradiation on Quantum Emitters in Hexagonal Boron Nitride. *ACS Appl. Mater. Interfaces* **10**, 24886–24891 (2018).
26. Frantsuzov, P., Kuno, M., Jankó, B. & Marcus, R. A. Universal emission intermittency in quantum dots, nanorods and nanowires. *Nat. Phys.* **4**, 519–522 (2008).
27. Kuno, M., Fromm, D. P., Hamann, H. F., Gallagher, A. & Nesbitt, D. J. Nonexponential “blinking” kinetics of single CdSe quantum dots: A universal power law behavior. *J. Chem. Phys.* **112**, 3117–3120 (2000).
28. Shotan, Z., Jayakumar, H., Considine, C. R., Mackoite, M., Fedder, H., Wrachtrup, J., Alkauskas, A., Doherty, M. W., Menon, V. M. & Meriles, C. A. Photoinduced Modification of Single-Photon Emitters in Hexagonal Boron Nitride. *ACS Photonics* **3**, 2490–2496 (2016).
29. Gottscholl, A., Kianinia, M., Soltamov, V., Orlinskii, S., Mamin, G., Bradac, C., Kasper, C., Krambrock, K., Sperlich, A., Toth, M., Aharonovich, I. & Dyakonov, V. Initialization and read-out of intrinsic spin defects in a van der Waals crystal at room temperature. *Nat. Mater.* **19**, 540–545 (2020).
30. Healey, A. J., Scholten, S. C., Yang, T., Scott, J. A., Abrahams, G. J., Robertson, I. O., Hou, X. F., Guo, Y. F., Rahman, S., Lu, Y., Kianinia, M., Aharonovich, I. & Tetienne, J. P. Quantum microscopy with van der Waals heterostructures. *Nat. Phys.* **19**, 87–91 (2023).
31. Mendelson, N., Doherty, M., Toth, M., Aharonovich, I. & Tran, T. T. Strain-Induced Modification of the Optical Characteristics of Quantum Emitters in Hexagonal Boron Nitride. *Adv. Mater.* **32**, 1908316 (2020).
32. Nikolay, N., Mendelson, N., Sadzak, N., Böhm, F., Tran, T. T., Sontheimer, B., Aharonovich, I. & Benson, O. Very Large and Reversible Stark-Shift Tuning of Single Emitters in Layered Hexagonal Boron Nitride. *Phys. Rev. Appl.* **10**, 041001 (2019).
33. Auburger, P. & Gali, A. Towards ab initio identification of paramagnetic substitutional carbon defects in hexagonal boron nitride acting as quantum bits. *Phys. Rev. B* **104**, 075410 (2021).
34. Chejanovsky, N., Mukherjee, A., Geng, J., Chen, Y. C., Kim, Y., Denisenko, A., Finkler, A., Taniguchi, T., Watanabe, K., Dasari, D. B. R., Auburger, P., Gali, A., Smet, J. H. & Wrachtrup, J. Single-spin resonance in a van der Waals embedded paramagnetic defect. *Nat. Mater.* **20**, 1079–1084 (2021).

35. Lee, H. Y., Al Ezzi, M. M., Raghuvanshi, N., Chung, J. Y., Watanabe, K., Taniguchi, T., Garaj, S., Adam, S. & Gradečak, S. Tunable Optical Properties of Thin Films Controlled by the Interface Twist Angle. *Nano Lett.* **21**, 2832–2839 (2021).
36. Su, C., Zhang, F., Kahn, S., Shevitski, B., Jiang, J., Dai, C., Ungar, A., Park, J. H., Watanabe, K., Taniguchi, T., Kong, J., Tang, Z., Zhang, W., Wang, F., Crommie, M., Louie, S. G., Aloni, S. & Zettl, A. Tuning colour centres at a twisted hexagonal boron nitride interface. *Nat. Mater.* **21**, 896–902 (2022).
37. Fischer, M., Caridad, J. M., Sajid, A., Ghaderzadeh, S., Ghorbani-Asl, M., Gammelgaard, L., Bøggild, P., Thygesen, K. S., Krasheninnikov, A. V., Xiao, S., Wubs, M. & Stenger, N. Controlled generation of luminescent centers in hexagonal boron nitride by irradiation engineering. *Sci. Adv.* **7**, 7138 (2021).
38. Kianinia, M., White, S., Fröch, J. E., Bradac, C. & Aharonovich, I. Generation of Spin Defects in Hexagonal Boron Nitride. *ACS Photonics* **7**, 2147–2152 (2020).
39. Xu, Z. Q., Elbadawi, C., Tran, T. T., Kianinia, M., Li, X., Liu, D., Hoffman, T. B., Nguyen, M., Kim, S., Edgar, J. H., Wu, X., Song, L., Ali, S., Ford, M., Toth, M. & Aharonovich, I. Single photon emission from plasma treated 2D hexagonal boron nitride. *Nanoscale* **10**, 7957–7965 (2018).
40. Mendelson, N., Chugh, D., Reimers, J. R., Cheng, T. S., Gottscholl, A., Long, H., Mellor, C. J., Zettl, A., Dyakonov, V., Beton, P. H., Novikov, S. V., Jagadish, C., Tan, H. H., Ford, M. J., Toth, M., Bradac, C. & Aharonovich, I. Identifying carbon as the source of visible single-photon emission from hexagonal boron nitride. *Nat. Mater.* **20**, 321–328 (2021).
41. Lyu, C., Zhu, Y., Gu, P., Qiao, J., Watanabe, K., Taniguchi, T. & Ye, Y. Single-photon emission from two-dimensional hexagonal boron nitride annealed in a carbon-rich environment. *Appl. Phys. Lett.* **117**, 244002 (2020).
42. Horder, J., White, S., Gale, A., Li, C., Watanabe, K., Taniguchi, T., Kianinia, M., Aharonovich, I. & Toth, M. Coherence properties of electron beam activated emitters in hexagonal boron nitride under resonant excitation. *Phys. Rev. Appl.* **18**, 064021 (2022).
43. Xu, X., Martin, Z. O., Sychev, D., Lagutchev, A. S., Chen, Y. P., Taniguchi, T., Watanabe, K., Shalaev, V. M. & Boltasseva, A. Creating Quantum Emitters in Hexagonal Boron Nitride Deterministically on Chip-Compatible Substrates. *Nano Lett.* **21**, 8182–8189 (2021).
44. Zhang, G., Cheng, Y., Chou, J. P. & Gali, A. Material platforms for defect qubits and single-photon emitters. *Appl. Phys. Rev.* **7**, 031308 (2020).
45. Aharonovich, I., Englund, D. & Toth, M. Solid-state single-photon emitters. *Nat. Photonics* **10**, 631–641 (2016).

46. Kianinia, M., Xu, Z. Q., Toth, M. & Aharonovich, I. Quantum emitters in 2D materials: Emitter engineering, photophysics, and integration in photonic nanostructures. *Appl. Phys. Rev.* **9**, 011306 (2022).
47. Tran, T. T., Zachreson, C., Berhane, A. M., Bray, K., Sandstrom, R. G., Li, L. H., Taniguchi, T., Watanabe, K., Aharonovich, I. & Toth, M. Quantum Emission from Defects in Single-Crystalline Hexagonal Boron Nitride. *Phys. Rev. Appl.* **5**, 034005 (2016).
48. Aharonovich, I., Tétienne, J. P. & Toth, M. Quantum Emitters in Hexagonal Boron Nitride. *Nano Lett.* **22**, 9227–9235 (2022).
49. Yang, T., Mendelson, N., Li, C., Gottscholl, A., Scott, J., Kianinia, M., Dyakonov, V., Toth, M. & Aharonovich, I. Spin defects in hexagonal boron nitride for strain sensing on nanopillar arrays. *Nanoscale* **14**, 5239–5244 (2022).
50. Gu, R., Wang, L., Zhu, H., Han, S., Bai, Y., Zhang, X., Li, B., Qin, C., Liu, J., Guo, G., Shan, X., Xiong, G., Gao, J., He, C., Han, Z., Liu, X. & Zhao, F. Engineering and Microscopic Mechanism of Quantum Emitters Induced by Heavy Ions in hBN. *ACS Photonics* **8**, 2912–2922 (2021).
51. Klaiss, R., Ziegler, J., Miller, D., Zappitelli, K., Watanabe, K., Taniguchi, T. & Alemán, B. Uncovering the morphological effects of high-energy Ga⁺focused ion beam milling on hBN single-photon emitter fabrication. *J. Chem. Phys.* **157**, 074703 (2022).
52. Weston, L., Wickramaratne, D., Mackoitt, M., Alkauskas, A. & Van De Walle, C. G. Native point defects and impurities in hexagonal boron nitride. *Phys. Rev. B* **97**, 214104 (2018).
53. Chu, P. K. & Li, L. Characterization of amorphous and nanocrystalline carbon films. *Mater. Chem. Phys.* **96**, 253–277 (2006).
54. Blundo, E., Surrente, A., Spirito, D., Pettinari, G., Yildirim, T., Chavarin, C. A., Baldassarre, L., Felici, M. & Polimeni, A. Vibrational Properties in Highly Strained Hexagonal Boron Nitride Bubbles. *Nano Lett.* **22**, 1525–1533 (2022).
55. Chen, L., Elibol, K., Cai, H., Jiang, C., Shi, W., Chen, C., Wang, H. S., Wang, X., Mu, X., Li, C., Watanabe, K., Taniguchi, T., Guo, Y., Meyer, J. C. & Wang, H. Direct observation of layer-stacking and oriented wrinkles in multilayer hexagonal boron nitride. *2D Mater.* **8**, 024001 (2021).
56. Ghaderzadeh, S., Kretschmer, S., Ghorbani-Asl, M., Hlawacek, G. & Krasheninnikov, A. V. Atomistic simulations of defect production in monolayer and bulk hexagonal boron nitride under low-and high-fluence ion irradiation. *Nanomaterials* **11**, 1214 (2021).

57. Zeng, W., Nie, W., Li, L. & Chen, A. Ground-state cooling of a mechanical oscillator in a hybrid optomechanical system including an atomic ensemble. *Sci. Rep.* **7**, 17258 (2017).
58. Midolo, L., Schliesser, A. & Fiore, A. Nano-opto-electro-mechanical systems. *Nat. Nanotechnol.* **13**, 11–18 (2018).
59. Noh, G., Choi, D., Kim, J. H., Im, D. G., Kim, Y. H., Seo, H. & Lee, J. Stark Tuning of Single-Photon Emitters in Hexagonal Boron Nitride. *Nano Lett.* **18**, 4710–4715 (2018).
60. Chakraborty, C., Goodfellow, K. M., Dhara, S., Yoshimura, A., Meunier, V. & Vamivakas, A. N. Quantum-Confined Stark Effect of Individual Defects in a van der Waals Heterostructure. *Nano Lett.* **17**, 2253–2258 (2017).
61. Teissier, J., Barfuss, A., Appel, P., Neu, E. & Maletinsky, P. Strain Coupling of a Nitrogen-Vacancy Center Spin to a Diamond Mechanical Oscillator. *Phys. Rev. Lett.* **113**, 020503 (2014).
62. Wang, L., Zihlmann, S., Baumgartner, A., Overbeck, J., Watanabe, K., Taniguchi, T., Makk, P. & Schönenberger, C. In Situ Strain Tuning in hBN-Encapsulated Graphene Electronic Devices. *Nano Lett.* **19**, 4097–4102 (2019).
63. Dev, P. Fingerprinting quantum emitters in hexagonal boron nitride using strain. *Phys. Rev. Res.* **2**, 22050 (2020).
64. Gao, X., Jiang, B., Llacsahuanga Allecca, A. E., Shen, K., Sadi, M. A., Solanki, A. B., Ju, P., Xu, Z., Upadhyaya, P., Chen, Y. P., Bhave, S. A. & Li, T. High-Contrast Plasmonic-Enhanced Shallow Spin Defects in Hexagonal Boron Nitride for Quantum Sensing. *Nano Lett.* **21**, 7708–7714 (2021).
65. Stern, H. L., Gu, Q., Jarman, J., Eizagirre Barker, S., Mendelson, N., Chugh, D., Schott, S., Tan, H. H., Siringhaus, H., Aharonovich, I. & Atatüre, M. Room-temperature optically detected magnetic resonance of single defects in hexagonal boron nitride. *Nat. Commun.* **13**, 618 (2022).
66. Caldwell, J. D., Aharonovich, I., Cassabois, G., Edgar, J. H., Gil, B. & Basov, D. N. Photonics with hexagonal boron nitride. *Nat. Rev. Mater.* **4**, 552–567 (2019).
67. Alaloul, M. & Khurgin, J. B. High-Performance All-Optical Modulator Based on Graphene-hBN Heterostructures. *IEEE J. Sel. Top. Quantum Electron.* **28**, 3500108 (2022).
68. Lien, D. H., Uddin, S. Z., Yeh, M., Amani, M., Kim, H., Ager, J. W., Yablonovitch, E. & Javey, A. Electrical suppression of all nonradiative recombination pathways in monolayer semiconductors. *Science* **364**, 468–471 (2019).

69. Klein, J., Lorke, M., Florian, M., Sigger, F., Sigl, L., Rey, S., Wierzbowski, J., Cerne, J., Müller, K., Mitterreiter, E., Zimmermann, P., Taniguchi, T., Watanabe, K., Wurstbauer, U., Kaniber, M., Knap, M., Schmidt, R., Finley, J. J. & Holleitner, A. W. Site-selectively generated photon emitters in monolayer MoS₂ via local helium ion irradiation. *Nat. Commun.* **10**, 2755 (2019).
70. Kim, S., Fröch, J. E., Christian, J., Straw, M., Bishop, J., Totonjian, D., Watanabe, K., Taniguchi, T., Toth, M. & Aharonovich, I. Photonic Crystal Cavities from Hexagonal Boron Nitride. *Nat. Commun.* **9**, 2623 (2018).
71. Li, C., Fröch, J. E., Nonahal, M., Tran, T. N., Toth, M., Kim, S. & Aharonovich, I. Integration of hBN Quantum Emitters in Monolithically Fabricated Waveguides. *ACS Photonics* **8**, 2966–2972 (2021).
72. Fröch, J. E., Spencer, L. P., Kianinia, M., Totonjian, D. D., Nguyen, M., Gottscholl, A., Dyakonov, V., Toth, M., Kim, S. & Aharonovich, I. Coupling Spin Defects in Hexagonal Boron Nitride to Monolithic Bullseye Cavities. *Nano Lett.* **21**, 6549–6555 (2021).
73. Glushkov, E., Macha, M., R ath, E., Navikas, V., Ronceray, N., Cheon, C. Y., Ahmed, A., Avsar, A., Watanabe, K., Taniguchi, T., Shorubalko, I., Kis, A., Fantner, G. & Radenovic, A. Engineering Optically Active Defects in Hexagonal Boron Nitride Using Focused Ion Beam and Water. *ACS Nano* **16**, 3695–3703 (2022).
74. Choi, S., Tran, T. T., Elbadawi, C., Lobo, C., Wang, X., Juodkazis, S., Seniutinas, G., Toth, M. & Aharonovich, I. Engineering and Localization of Quantum Emitters in Large Hexagonal Boron Nitride Layers. *ACS Appl. Mater. Interfaces* **8**, 29642–29648 (2016).
75. Gale, A., Li, C., Chen, Y., Watanabe, K., Taniguchi, T., Aharonovich, I. & Toth, M. Site-Specific Fabrication of Blue Quantum Emitters in Hexagonal Boron Nitride. *ACS Photonics* **9**, 2170–2177 (2022).
76. Li, C., Mendelson, N., Ritika, R., Chen, Y., Xu, Z. Q., Toth, M. & Aharonovich, I. Scalable and Deterministic Fabrication of Quantum Emitter Arrays from Hexagonal Boron Nitride. *Nano Lett.* **21**, 3626–3632 (2021).
77. Fournier, C., Plaud, A., Roux, S., Pierret, A., Rosticher, M., Watanabe, K., Taniguchi, T., Buil, S., Qu elin, X., Barjon, J., Hermier, J. P. & Delteil, A. Position-controlled quantum emitters with reproducible emission wavelength in hexagonal boron nitride. *Nat. Commun.* **12**, 3779 (2021).
78. Gilbert, S. M., Liu, S., Schumm, G. & Zettl, A. Nanopatterning Hexagonal Boron Nitride with Helium Ion Milling: Towards Atomically-thin, Nanostructured Insulators. *MRS Adv.* **3**, 327–331 (2018).
79. Proscia, N. Control of Light-Matter Interactions via Nanostructured Photonic Materials. *CUNY Acad. Work.* (2019).

80. Lassaline, N., Thureja, D., Chervy, T., Petter, D., Murthy, P. A., Knoll, A. W. & Norris, D. J. Freeform Electronic and Photonic Landscapes in Hexagonal Boron Nitride. *Nano Lett.* **21**, 8175–8181 (2021).
81. Ziegler, J. F., Ziegler, M. D. & Biersack, J. P. SRIM - The stopping and range of ions in matter. *Nucl. Instruments Methods Phys. Res. Sect. B Beam Interact. with Mater. Atoms* **268**, 1818–1823 (2010).
82. Vladov, N., Segal, J. & Ratchev, S. Apparent beam size definition of focused ion beams based on scanning electron microscopy images of nanodots. *J. Vac. Sci. Technol. B, Nanotechnol. Microelectron. Mater. Process. Meas. Phenom.* **33**, 041803 (2015).
83. Gupta, S., Periasamy, P. & Narayanan, B. Defect dynamics in two-dimensional black phosphorus under argon ion irradiation. *Nanoscale* **13**, 8575–8590 (2021).
84. Gao, Y., Zhang, Y., Schwen, D., Jiang, C., Sun, C. & Gan, J. Formation and self-organization of void superlattices under irradiation: A phase field study. *Materialia* **1**, 78–88 (2018).
85. Gilbert, S. M., Dunn, G., Azizi, A., Pham, T., Shevitski, B., Dimitrov, E., Liu, S., Aloni, S. & Zettl, A. Fabrication of Subnanometer-Precision Nanopores in Hexagonal Boron Nitride. *Sci. Rep.* **7**, 15096 (2017).
86. Mouhoub, O., Martinez-Gordillo, R., Nelayah, J., Wang, G., Park, J. H., Kim, K. K., Lee, Y. H., Bichara, C., Loiseau, A., Ricolleau, C., Amara, H. & Alloyeau, D. Quantitative insights into the growth mechanisms of nanopores in hexagonal boron nitride. *Phys. Rev. Mater.* **4**, 014005 (2020).
87. Pham, T., Gibb, A. L., Li, Z., Gilbert, S. M., Song, C., Louie, S. G. & Zettl, A. Formation and Dynamics of Electron-Irradiation-Induced Defects in Hexagonal Boron Nitride at Elevated Temperatures. *Nano Lett.* **16**, 7142–7147 (2016).
88. Paszkowicz, W., Pelka, J. B., Knapp, M., Szyszko, T. & Podsiadlo, S. Lattice parameters and anisotropic thermal expansion of hexagonal boron nitride in the 10-297.5 K temperature range. *Appl. Phys. A Mater. Sci. Process.* **75**, 431–435 (2002).
89. Millett, P. C., Rokkam, S., El-Azab, A., Tonks, M. & Wolf, D. Void nucleation and growth in irradiated polycrystalline metals: A phase-field model. *Model. Simul. Mater. Sci. Eng.* **17**, 064003 (2009).
90. Weston, L., Wickramaratne, D., Mackoite, M., Alkauskas, A. & Van De Walle, C. G. Native point defects and impurities in hexagonal boron nitride. *Phys. Rev. B* **97**, 214104 (2018).
91. Abdi, M., Hwang, M., Aghtar, M. & Plenio, M. B. Spin-Mechanical Scheme with Color Centers in Hexagonal Boron Nitride Membranes. *Phys. Rev. Lett.* **119**, 233602 (2017).

92. Abdi, M. & Plenio, M. B. Quantum Effects in a Mechanically Modulated Single-Photon Emitter. *Phys. Rev. Lett.* **122**, 23602 (2019).
93. Aradi, E., Naidoo, S. R., Cummings, F., Motochi, I. & Derry, T. E. Cross-sectional transmission electron microscopy studies of boron ion implantation in hexagonal boron nitride. *Diam. Relat. Mater.* **92**, 168–173 (2019).
94. Tawfik, S. A., Ali, S., Fronzi, M., Kianinia, M., Tran, T. T., Stampfl, C., Aharonovich, I., Toth, M. & Ford, M. J. First-principles investigation of quantum emission from hBN defects. *Nanoscale* **9**, 13575–13582 (2017).
95. Abdi, M., Chou, J. P., Gali, A. & Plenio, M. B. Color Centers in Hexagonal Boron Nitride Monolayers: A Group Theory and Ab Initio Analysis. *ACS Photonics* **5**, 1967–1976 (2018).
96. Li, S., Pershin, A., Thiering, G., Udvarhelyi, P. & Gali, A. Ultraviolet quantum emitters in hexagonal boron nitride from carbon clusters. *J. Phys. Chem. Lett.* **13**, 3150–3157 (2022).
97. Li, K., Smart, T. J. & Ping, Y. Carbon trimer as a 2 eV single-photon emitter candidate in hexagonal boron nitride: A first-principles study. *Phys. Rev. Mater.* **6**, L042201 (2022).
98. Carr, E. J. & Turner, I. W. A semi-analytical solution for multilayer diffusion in a composite medium consisting of a large number of layers. *Appl. Math. Model.* **40**, 7034–7050 (2016).
99. Perdew, J. P. & Yue, W. Accurate and simple density functional for the electronic exchange energy: Generalized gradient approximation. *Phys. Rev. B* **33**, 8800–8802 (1986).
100. Perdew, J. P., Burke, K. & Ernzerhof, M. Generalized Gradient Approximation Made Simple. *Phys. Rev. Lett.* **77**, 3865–3868 (1996).
101. Giannozzi, P., Baroni, S., Bonini, N., Calandra, M., Car, R., Cavazzoni, C., Ceresoli, D., Chiarotti, G. L., Cococcioni, M., Dabo, I., Corso, A. D., Gironcoli, S. De, Fabris, S., Fratesi, G., Gebauer, R., Gerstmann, U., Gougoussis, C., Kokalj, A., Lazzeri, M., Martin-Samos, L., Marzari, N., Mauri, F., Mazzarello, R., Paolini, S., Pasquarello, A., Paulatto, L., Sbraccia, C., Scandolo, S., Sclauzero, G., Seitsonen, A. P., Smogunov, A., Umari, P. & Wentzcovitch, R. M. QUANTUM ESPRESSO: a modular and open-source software project for quantum simulations of materials. *J. Phys. Condens. Matter* **21**, 395502 (2009).
102. Monkhorst, H. J. & Pack, J. D. Special points for Brillouin-zone integrations. *Phys. Rev. B* **13**, 5188–5192 (1976).
103. Tanaka, T., Matsunaga, K., Ikuhara, Y. & Yamamoto, T. First-principles study on structures and energetics of intrinsic vacancies in SrTiO₃. *Phys. Rev. B* **68**, 205213 (2003).

104. Li, Q., Wang, J.-F., Yan, F.-F., Zhou, J.-Y., Wang, H.-F., Liu, H., Guo, L.-P., Zhou, X., Gali, A., Liu, Z.-H., Wang, Z.-Q., Sun, K., Guo, G.-P., Tang, J.-S., Li, H., You, L.-X., Xu, J.-S., Li, C.-F. & Guo, G.-C. Room-temperature coherent manipulation of single-spin qubits in silicon carbide with a high readout contrast. *Natl. Sci. Rev.* **9**, (2022).
105. Schuler, B., Lee, J. H., Kastl, C., Cochrane, K. A., Chen, C. T., Refaely-Abramson, S., Yuan, S., Van Veen, E., Roldán, R., Borys, N. J., Koch, R. J., Aloni, S., Schwartzberg, A. M., Ogletree, D. F., Neaton, J. B. & Weber-Bargioni, A. How Substitutional Point Defects in Two-Dimensional WS₂ Induce Charge Localization, Spin-Orbit Splitting, and Strain. *ACS Nano* **13**, 10520–10534 (2019).
106. Grosso, G., Moon, H., Lienhard, B., Ali, S., Efetov, D. K., Furchi, M. M., Jarillo-Herrero, P., Ford, M. J., Aharonovich, I. & Englund, D. Tunable and high-purity room temperature single-photon emission from atomic defects in hexagonal boron nitride. *Nat. Commun.* **8**, 705 (2017).